Hazy 2

a brief introduction to Cloudy 95

computational methods

G.J. Ferland
Department of Physics and Astronomy
University of Kentucky, Lexington
http://www.pa.uky.edu/~gary/cloudy

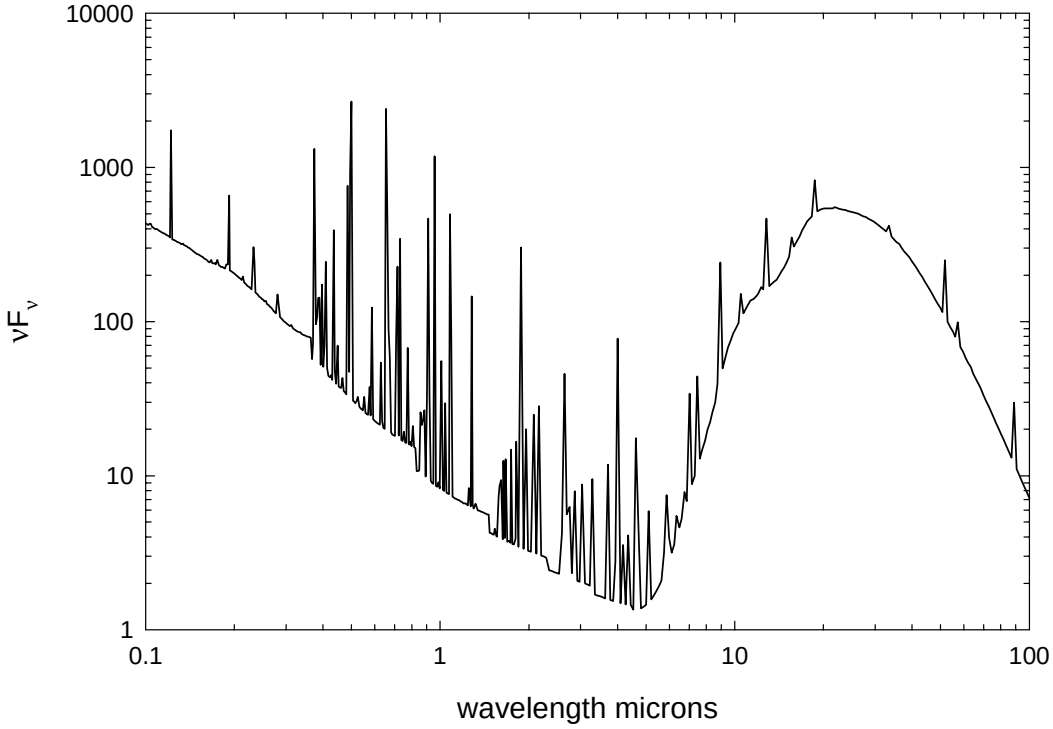

Use of this program is not restricted provided each use is acknowledged upon publication. The bibliographic reference to this version of Cloudy is Ferland, G.J., 2001, *Hazy, a Brief Introduction to Cloudy*, University of Kentucky Department of Physics and Astronomy Internal Report.

Cloudy is an evolving code. Updates are made on a roughly quarterly basis, while major revisions occur roughly every three years. You should confirm that you have the most recent version of the code by checking the web site http://www.pa.uky.edu/~gary/cloudy or asking to be placed on the Cloudy mailing list.

April 14, 2001.

CLOUDY 95

G. J. Ferland
Department of Physics and Astronomy
University of Kentucky
Lexington

Table of Contents

List of Figures

List of Tables

1 INTRODUCTION

This section outlines the computational methods used in version 95 of Cloudy. Parts are modified from Ferland and Mushotzky (1984), Ferland and Rees (1988), Ferland and Persson (1989), Rees, Netzer, and Ferland (1989), Baldwin et al. (1991), Ferland, Fabian, and Johnstone (1994), Ferland et al. (1992), Ferland (1992) and Ferland et al. (1998). The code has been designed to be as general as possible (but limited to non-relativistic regimes which are not Compton-thick) while remaining computationally expedient. Similar discussions of hydrogen line formation, focusing on the density range $n \leq 10^{11}$ cm^{-3} appropriate to quasar emission-line clouds, can be found, for instance, in Mathews, Blumenthal, and Grandi (1980) and Drake and Ulrich (1980). Discussions of line formation and ionization and thermal equilibria are presented by Osterbrock (1988), Davidson and Netzer (1979), Kwan and Krolik (1981), Halpern and Grindlay (1980), Weisheit, Shields, and Tarter (1981), Kallman and McCray (1982), Hubbard and Puetter (1985), Vernazza, Avrett, and Loeser (1981), Avrett and Loeser (1988), and Netzer (1990).

2 THE CONTINUUM MESH

2.1 Overview

Under most circumstances the continuum produced by the central object is the only source of heat and ionization for the emission-line clouds. This section describes how this continuum is treated.

Variable dealing with the continuum mesh are contained within the structure rfield, defined in the header file *rfield.h*. The following sections refer to parts of that structure.

2.2 Continuum Range

The energy interval 1.001×10^{-8} Ryd — 7.354×10^{6} Ryd is divided into ~2200 energy bins with nearly logarithmically increasing widths.

emm This is the low-energy limit to the continuum array. It can only be changed by modifying the statement where its value is set. Its current value is 1.001×10^{-8} Ryd.

egamry This is the high energy limit to the continuum array. The current value is 7.354×10^{6} Ryd.

nupper This is the number of cells needed to define the continuum from the low energy limit, up to its high energy limit of 7.354×10^{6} Ryd. It does not depend on the continuum shape but does depend on how fine the frequency mesh is. Array indices within the continuum arrays can be defined up through an energy of ***egamry***, and they will have the value ***nupper***. A particular continuum source may not extend this high, as discussed next.

nflux Each of the continuum intensity vectors is defined up to the high-energy limit for the particular continuum generated. The array index to this higher energy limit is the variable ***nflux***. ***nflux*** is chosen so that, for the highest energy considered, ν_{high} = ***anu(nflux)***, $\nu f_\nu(\nu_{high}) / \nu f_\nu(\nu_{peak}) <$ ***FluxFaint***, where ν_{peak} is the frequency where the continuum reaches its maximum νf_ν. ***FluxFaint*** is normally 10^{-10} and is reset with the **`set flxfnt`** command.

2.3 The Continuum Mesh

2.3.1 Defining the continuum energy mesh

The array ***anu*** specifies the energy of the center of each continuum cell, in Rydbergs. This energy scale is defined in routine ***ContCreatePointers*** . The continuum energy mesh is established by successive calls to routine ***fill***. Each call defines the continuum mesh over a specific energy range, at a specific resolution. This provides the option to have different energy resolutions over different energy ranges. This is important become some spectral regions are rich with features and require relatively high resolution (the optical and UV are examples) while others have few features and only modest is required (hard X-Rays are an example). The full continuum is set by a series of calls to ***fill***, each with its own energy range and energy resolution.

fill has five arguments. The first two are the lower and upper bounds to the energy range defined by that call to ***fill***. The third argument is the energy resolution desired over that energy range, expressed as a relative resolution, $\delta\nu/\nu$. The 4th argument is the starting index within the frequency grid, and can extend up to ***ncell***. The fifth argument is a pointer indicating which energy band this is — it is incremented for each call to ***fill***.

The code will stop if it is not possible to define the entire energy range 1.001×10^{-8} Ryd — 7.354×10^{6} Ryd with ***ncell*** cells. ***nupper*** is set to the pointer to the highest energy cell, at 7.354×10^{6} Ryd, after these calls to ***fill***.

2.3.2 Changing the energy resolution of the mesh

Altering the value of the third argument to ***fill*** will change the resolution of a particular range of the continuum mesh. This number is the fractional resolution $\delta\nu/\nu$, where ν is the energy.

If the energy resolution is increased then the code will require more mesh points to cover the full continuum, and will run more slowly. It may necessary to increase the size of continuum vectors.

2.3.3 Array indices within the continuum mesh

After the continuum energy scale is defined, one of the following routines should be used to find the array index corresponding to a given energy.

ipoint This function converts energies (Rydberg) into array indices for the cell in ***anu*** containing the specified energy. It has a single argument, the energy in Rydberg, and returns the index for the appropriate cell. ***ipoint*** will stop if the energy does not lie within the continuum bounds of the code.

In most cases the previous routine is not used, but rather one of the following routines used instead (they call ***ipoint***). The difference is that the following routines take two arguments, the energy in Rydbergs and a four-character null terminated string that identifies the line or continuum. An index for an emission line should be generated with a call to ***ipLineEnergy*** and a continuum edge to ***ipContEnergy***.

ipLineEnergy This routine calls ***ipoint*** and generates an index for the energy of an emission line. Line labels are stored in the four-character array ***chLineLabel***. In some cases it is important that a line index not exceed a certain value. For instance, energy would not be conserved if a Lyman line overlapped with the Lyman continuum. This routine has a third argument, an array index. If this is greater than zero then this routine will guarantee that the returning index does not equal or exceed this value.

ipContEnergy This routine calls ***ipoint*** and generates a index to the energy of a continuum edge. Continuum labels are stored in the four-character array ***chContLabel***.

2.4 Continuum Arrays

Several vectors deal with aspects of the attenuated incident and diffuse continua. All fluxes are stored in units photons cm^{-2} s^{-1} $cell^{-1}$ and they all map one-to-one with one another.

2.4.1 Continuum definition

anu The energy (in Rydbergs) of the center of each cell is stored in the vector ***anu***. There are ***nupper*** cells with defined energies. This energy grid *does* have a weak dependence on continuum shape since the center of the cell is defined by a weighted average over the incident continuum.

AnuOrg This array saves the initial frequency array, so that it may be reset when the code is initialized during compuations of many grid models. The opacity array is defined using this energy array.

ContBoltz Continuum Boltzmann factors, the ratio exp($-h\nu/kT$), are stored in the vector ***ContBoltz***, which is evaluated in routine ***boltgn***.

widflx The width of each cell (Rydbergs) is stored in the vector ***widflx***. There are ***nupper*** cells with defined widths. This energy grid does not depend on the continuum shape.

2.4.2 Continuum vectors

These store information relevant to the local radiaion field. All are members of the structure rfield.

Outward continua:

ConOutNoInter This is a continuum that is carried outward, but does not interact with the gas. It contains mainly continua whose gas interactions are included by other methods, such as OTS. This does not affect the ionization of the gas directly, but is included in the punched continuum.

ConOutRecInter This contains ground state recombination continua that are carried outward.

ConOutInter stores the continua that are carried outward and treated as sources of ionizing radiation. This continuum is the local outward continuum at the current position within the nebula, with correction for the r^{-2} dilution of radiation.

outlin stores the many lines that are carried outward and treated as sources of ionizing radiation.

Reflected continua:

ConRefIncid The reflected incident continuum.

ConRefDiff The diffuse continuum emitted in the inward direction.

reflin The “reflected” lines (that emergent from the illuminated face of the cloud) is stored in the vector ***reflin***. Throughout the calculation the reflected continuum and lines are stored relative to the inner radius of the cloud. This is only computed for an open geometry.

Local diffsure continua

Continuous diffuse emission is evaluated in routine ***RTDiffuse***.

ConLocInter This stores the local diffuse continuum (total local emission due to all processes, *per unit volume* with no filling factor).

ConLocNoInter Non-interacting local continua.

flux The attenuated incident continuum is stored in the vector ***flux***. The actual contents of ***flux*** are given by

$$flux(\nu) = 4\pi J_{inc} \frac{\Delta\nu}{h\nu} \text{ photons cm}^{-2}\text{ s}^{-1} \quad (100)$$

where the cell width is $\Delta\nu$.

Continuum occupation numbers

OccNumbDiffCont and *OccNumbIncidCont* The photon occupation number associated with the attenuated incident continuum is stored in the vector ***OccNumbIncidCont***. The occupation number associated with the diffuse continuum is given by *OccNumbDiffCont*.

The occupation number at a frequency ν is given by

$$\eta_\nu \equiv J_\nu / \left(2h\nu^3 / c^2\right) = \left(\exp(h\nu / kT_{ex}\right) - 1)^{-1} \quad . \quad (100)$$

Here J_ν is the mean intensity of the continuum at the frequency, and T_{ex} is the excitation temperature of the continuum at the frequency.

On the Spot arrays

otscon* and *otslin Two vectors, ***otscon*** and ***otslin***, store the local on-the-spot (OTS) photon fluxes for continua and lines. Both are totally local rates.

Summed continua:

Several continua are summed together to speed up the evaluation of the local interaction rates. This is done in routine ***SumContinuum***.

SummedDif This is summed diffuse continua.

SummedCon This is the sum of ***SummedDif*** and ***flux***, the attenuated incident continuum.

SummedOcc This is the continuum occupation number corresponding to ***SummedCon***.

2.4.3 Continuum optical depth arrays

These arrays define the gas opacity and are members of the *opac* structure, which is defined in the file *opacity.h*.

TauAbsFace, TauScatFaceThese are the arrays containing the absorption and scattering optical depths from the current position to the illuminated face of the cloud.

TauAbsFace, TauScatFace, TauTotalGeo Total absorption, scattering, and total (absorption plus scattering) optical depths are stored in three arrays, ***TauAbsFace[2][ncell]***, and ***TauScatFace[2][ncell]***, TauTotalGeo***[2][ncell]***, respectively. These map one-to-one with the ***anu*** that gives the photon energy.

The first element of the first dimension of the array gives the optical depth from the illuminated face to the current position. The second element gives the total optical depth determined in the previous iteration. For an open geometry this optical depth is only the optical depth of the computed structure. For a closed geometry the optical depth at the illuminated face is set equal to the computed optical depth.

ExpmTau The vector ***ExpmTau*** contains the attenuation term $\exp(-\tau_\nu)$ for each frequency in ***anu***. This is the attenuation from the current position to the illuminated face of the cloud.

e2TauAbs The vector ***e2TauAbs*** contains the term $E_2(\tau)$ where τ is the absorption optical depth from the current position to the illuminated face of the cloud.

ExpZone This is the term $\exp(-d\tau)$ for the current zone.

opac This is the array of continuous absorption opacities (units cm^{-1}). It is evaluated in ***addopc***.

scatop This is the array of continuous scattering opacities (units cm^{-1}). It is evaluated in ***addopc***.

2.5 Continuum Generation

The continuum is generated by the function ***ffun***. ***ffun*** has a single argument, the energy in Rydbergs, and it returns the number of photons per unit area, time, and Rydberg, at that energy. ***ffun*** sums over all the specified continua and applies the appropriate normalization factors. Another function, ***ffun1***, evaluates each individual continuum, and is normally called only by ***ffun***.

The units, and their conversion to other measures of the continuum, are given below. The photon flux density is:

$$\varphi_\nu(\nu) = \mathrm{FFUN}(\nu) \quad \text{photons} \quad \mathrm{cm}^{-2}\ \mathrm{s}^{-1}\ \mathrm{Ryd}^{-1} \quad . \tag{101}$$

This is stored in the photon array:

$$\mathrm{FLUX}(\nu_i) = \varphi_\nu(\nu)\,\delta\nu_i = \mathrm{FFUN}(\nu_i) \times \mathrm{WIDFLX}(\nu) \quad \text{photons} \quad \mathrm{cm}^{-2}\ \mathrm{s}^{-1} \quad . \tag{102}$$

Finally, the energy flux density is given by

$$f_\nu(\nu) = \mathrm{FFUN}(\nu)\, h\left(\frac{\nu}{\nu_{912}}\right) \quad \text{erg} \quad \mathrm{cm}^{-2} \quad \mathrm{s}^{-1} \quad \mathrm{Hz}^{-1} \tag{103}$$

and

$$\nu f_\nu(\nu) = \mathrm{FFUN}(\nu)\, h\left(\frac{\nu}{\nu_{912}}\right) \nu_{912}\, h\nu_{Ryd} \quad \text{erg} \quad \mathrm{cm}^{-2} \quad \mathrm{s}^{-1} \quad . \tag{104}$$

2.5.1 Blackbody emission

For reference, the Planck function is given by

$$B_\nu = \frac{F_\nu}{\pi} = \frac{2h\nu^3}{c^2} \frac{1}{\exp(h\nu / kT) - 1} \quad \text{erg cm}^{-2}\ \text{s}^{-1}\ \text{sr}^{-1}\ \text{Hz}^{-1}. \tag{105}$$

Function ***plankf*** evaluates the Planck function for the current electron temperature. It has a single argument, a pointer to the desired continuum energy. It returns the photon flux for that cell.

2.5.2 Continuum Normalization

The continuum normalization is performed in routine ***conorm***.

2.6 Energy Units; The Rydberg

Continuum energies are usually given in Rydbergs. One Rydberg is approximately equal to the ionization potential of hydrogen, which is

$$R_H \equiv 2.178728 \times 10^{-11}\ \text{erg} = 13.59842\ \text{eV} = 91.176340\ \text{nm} = 109677.576\ \text{cm}^{-1} \tag{106}$$

This was the Rydberg unit used by Cloudy before 1988, and *is not* the more commonly used R_∞, for infinite mass nuclei.

The energy scale is now in terms of R_∞, using the 1986 CODATA revision of the fundamental constants (Cohen and Taylor 1987). In these units, the wavenumber corresponding to R_∞ is

$$R_\infty \equiv \frac{2\pi^2 m_e q_e^4}{ch^3} = 109737.315 \quad \mathrm{cm}^{-1} \quad , \tag{107}$$

the wavelength in vacuum is

$$1 / R_\infty = 91.126732 \quad \mathrm{nm}, \tag{108}$$

the frequency is

$$c\,R_\infty = 3.289842 \times 10^{15} \ \mathrm{s}^{-1} \ , \tag{109}$$

and this corresponds to an energy

$$1 \ \ \mathrm{Ryd} = chR_\infty = 2.179874 \times 10^{-11} \ \mathrm{erg} = 13.605698 \quad \mathrm{eV}{=}1.5788866 \times 10^5 \mathrm{K} \quad . \tag{110}$$

Thus the ionization potential of hydrogen is actually 0.99946 Ryd. Thes difference between the H and infinite mass constants is significant since it enters as the third power in the photon phase-space conversion factor $2h\nu^3/c^2$.

Another commonly used unit is the “atomic unit”, also called the Hartree, which is equal to *two* Rydbergs (i.e., $2R_\infty$).

2.7 Conversion Factors

Table 16 gives conversion factors between various common units. The last column of the table gives the variable names for constants that occur in parameter statements within the code. These should be used instead of entering the constant directly. In the following all Rydbergs are for infinite mass nuclei.

The fundamental constants now used by the code are from a variety of revisions of the basic data, some dating back to the 1970’s. An effort is now underway to convert the constants to the 1986 CODATA recommended values (see http://physics.nist.gov/PhysRefData/codata86/codata86.html).

Table 16 Conversion Factors

To convert from	Variable	to	multiply by	Parameter
phot/s/cm^2	flux	f_ν	ν_{Ryd} $h\nu_1$ (erg)	
phot/Ryd/s/cm^2	flux/widflx	νf_ν	ν_{Ryd}^2 $h\nu_1$ (erg)	
phot/Ryd/s/cm^2	flux/widflx	J_ν	ν_{Ryd} h	
optical depth	tautot	A_V(mag)	1.08574	
energy (eV)		ergs	1.602192(-12)	
energy (eV)		K	1.1604448(4)	***eVdegK***
energy (Ryd)	anu	Kelvin	1.5788866(5)	***te1ryd***
energy (Ryd)	anu	ergs	2.179874(-11)	***en1ryd***
energy (Ryd)	anu	cm^{-1}	109737.315	***1/WavNRyd***
energy (Ryd)	anu	eV	13.6056981	***evRyd***
energy (Ryd)	anu	Å	911.6	***rydlam***
energy (Ryd), T	anu, Te	$h\nu$ /kT	1.5788866(5)*anu/Te	***te1ryd***
temperature (K)	Te	eV	8.617385(-5)	
temperature (K)	Te	ergs	1.38063(-16)	***boltzmann***
temperature (K)	Te	Rydbergs	1/1.5788866(5)	1/***te1ryd***
wavelength (cm)		microns	1(+4)	
wavelength (cm)		Å	1(+8)	
wavelength (Å)		Ergs	1.9864(-8)/λ(Å)	
wavelength (Å)		degree K	1.43877(+8)/λ(Å)	
wavelength (cm)		degree K	1.43877/λ(cm)	
wavelength (micron)		degree K	1.43877(+4)/λ(μ)	
wavelength (micron)		ergs	1.9864(-12)/λ(μ)	
wavenumbers (cm^{-1})		ergs	1.98648(-16)	
wavenumbers (cm^{-1})		degree K	1.43877	***WavNKelv***
wavenumbers (cm^{-1})		Rydbergs	9.1126732(-6)	***WavNRyd***

3 CONTINUUM INTERACTIONS

3.1 Attenuation of the Incident Continuum

In an open geometry scattering is assumed to attenuate the incident continuum as

$$I = I_o \left(1 + 0.5\, d\tau_{scat}\right)^{-1} \quad . \tag{111}$$

Scattering does not affect the continuum in a closed geometry. Absorption is assumed to attenuate the incident continuum as

$$I = I_o \exp(-d\tau_{abs}) \quad . \tag{112}$$

for both geometries.

3.2 Recombination Equilibrium

3.2.1 On-the-spot approximation

A modified version of the "on-the-spot" (OTS) approximation is used in the treatment of sources of diffuse ionizing radiation when the **`diffuse ots`** command is used. Were no other opacity sources present, then, for a closed geometry that is optically thick in the Lyman continuum, all recombinations of hydrogen or helium to the ground state would produce ionizing photons. Other atoms of the recombined species would quickly absorb these. In this case OTS is an excellent approximation (Van Blerkom and Hummer 1967; Bässgen, Bässgen, and Grewing 1988). However, other opacity sources are present, and these compete in absorbing protons produced by recombinations, making the recombination process more efficient than the OTS approximation would suggest.

The recombination coefficients for all states of hydrogen and helium are modified by the presence of all other opacity sources, such as grains, free-free or H^- absorption, and the heavy element opacities, in the following manner. The net effective recombination rate coefficient ($cm^3\ s^{-1}$) to level *n*, $\hat{\alpha}(T_e, n)$, is written in terms of the spontaneous radiative recombination rate coefficient $\alpha(T_e, n)$, and the opacities (cm^{-1}) κ_n and κ_0 for the level *n* and other opacity sources respectively, as

$$\hat{\alpha}\left(T_e, n\right) = \alpha(T_e, n)\left\{P_c(n) + \left[1 - P_c(n)\right]\left(\frac{\kappa_o}{\kappa_o + \kappa_n}\right)\right\} \quad , \tag{113}$$

where $P_c(n)$ is the continuum escape probability. In general, $P_c(n)$ varies between 0 and 0.5 for an optically thick open geometry (see, for example Davidson 1977), $P_c \sim 1$ if the gas is optically thin, and $P_c \sim 0$ for ground states if the gas is optically thick and the geometry is closed. All computed opacity sources are included in κ_0.

These recombination continua produce a flux of local on-the-spot photons, φ_{OTS} ($cm^{-2}\ s^{-1}$). The OTS photoabsorption rate Γ_{OTS} (s^{-1}), used to determine the ionization or heating rate for the gas or grain constituents, is then $\Gamma_{OTS} = \alpha_\nu \varphi_{OTS}$ where α_ν is the absorption cross section at frequency ν. The OTS flux is related to the spontaneous recombination rate coefficient by

$$\varphi_{OTS} = \alpha\left(T_e, n\right) n_e \, n_{ion} \left[\frac{1-P_c(\tau)}{\kappa_o + \kappa_n}\right] \text{ cm}^{-2} \text{ s}^{-1} \qquad (114)$$

where n_{ion} is the density of the ion in question. These are stored in the vectors ***otscon*** and ***otslin***, which map one-to-one onto the vectors ***flux*** and ***anu***.

3.2.2 Outward only approximation

A composite "outward-only"-"on-the-spot" approximation is used in the treatment of sources of diffuse ionizing radiation when the **`diffuse outward`** command is used. This is the default assumption. The escaping radiation is then propagated in the outward direction (all for the spherical case, and half for an open geometry).

3.3 Continuous Opacities

The cloud is divided into a large number of concentric shells (zones) and the attenuated and diffuse continua and physical conditions are then determined within each.

The main opacity sources in the ultraviolet continuum are generally photoelectric and free-free (inverse brems) absorption, grain opacity, electron scattering (of both bound and free electrons), and the damping wings of Lyman lines (Rayleigh scattering). The main reemission mechanisms are generally free-free (bremstrahlung), grain emission, free-bound, and two-photon emission. Grains are not present by default but can be added as an option. Continuous absorption and reemission by all ground states, and many excited states, of all ionization stages of the 30 elements in the calculation are explicitly included. Great care is taken to ensure that each absorption mechanism is balanced by a reemission process, and vice versa, so that energy balance in the strict thermodynamic equilibrium limit can be achieved.

3.3.1 Opacity arrays

Total absorption opacities (cm^{-1}) are storied in the vector ***opac***. Total scattering opacities (cm^{-1}) are stored in ***scatop***. The opacities are evaluated in routine ***AddOpac***.

3.3.2 Cross-section array

Storage. The cross sections per particle (cm^2) for individual species (atoms, ions, molecules, etc) are stored within the array *OpacStack*, a stack array with a single dimension. These cross sections are evaluated when the code is initialized in routine *OpacityCreateAll*.

Array indices. Each species has an associated array index that defines the offset between the origin of *OpacStack*, the frequency array *anu*, and the opacity at the threshold. If this offset has the name ***ioff***, for instance, then the cross section at threshold will be given by array element *OpacStack[ioff]*. If *ip* is the index to the threshold energy within *anu*, then the array index to the cross section at an energy *i* will be *i-ip+ioff*.

Individual cross-sections. The function *csphot* returns the cross section at a specific frequency for any species. It has three arguments, 1) the pointer to the frequency in *anu* where the cross section is to be evaluated, 2) the pointer to the

threshold for the species, and 3) the *ioff* offset described above. All are integer variables.

3.3.3 Photoionization rates

Photoionization rates (units s^{-1}) can be computed by several functions. Which is used at a particular time is determined by circumstances.

GammaK This computes the photoionization rate with allowance for an arbitrary fluorescence yield. This routine is a major pacesetter for the code since it is used to evaluate the continuum rates in the majority of the cases. The photoionization rate is given by

$$\Gamma_n = 4\pi \int_{\nu_o}^{\infty} \frac{J_\nu}{h\nu} \alpha_\nu \, d\nu \quad . \tag{115}$$

The routine has three integer arguments, the *anu* pointers to the lower and upper energies, and the offset to the opacity array ***ioff*** (described above).

GammaPrt This is a special version of ***GammaK*** that writes (on any open file) the step by step results of the integration. The output lists the product of the photon flux and the cross section, the photon flux, and the opacity.

GammaBn This is a special version of ***GammaK*** that is used when the correction for stimulated emission or induced recombination is important. The photoionization rate is given by

$$\Gamma_n = 4\pi \int_{\nu_o}^{\infty} \frac{J_\nu}{h\nu} \alpha_\nu \, d\nu \tag{116}$$

and the rate for induced recombination and its associated cooling is computed as

$$\alpha(ind) = P_n^* 4\pi \int_{\nu_o}^{\infty} \frac{J_\nu}{h\nu} \alpha_\nu \exp(-h\nu / kT) \, d\nu \quad . \tag{117}$$

where P^* is the LTE population.

GammaPrtRate will print photo rates for all shells of an ion and element. It is called with three arguments, a file handle, followed by the ionization stage and element number on the C scale (0 for H or atoms, etc).

3.3.4 Attenuation within the zone

A correction must be made to account for the attenuation of the continuum across the zone (Netzer and Ferland 1983). Assuming that the continuum varies across the zone as

$$\frac{I(\nu, \delta r)}{I_o(\nu)} = \exp\left(-\kappa(\nu) f(r) \delta r\right) \tag{118}$$

then the intensity averaged over a zone with thickness δr is

$$\left\langle \frac{I(\nu, \delta r)}{I_o(\nu)} \right\rangle = \frac{1 - \exp\left(-\kappa(\nu) f(r) \delta r\right)}{\kappa(\nu) f(r) \delta r} \tag{119}$$

where $\kappa(\nu)$ is the absorption opacity and $f(r)$ is the filling factor. The coefficients giving this ratio as a function of energy are stored in the vector *tmn*, and are evaluated in subroutine ***radinc***. The continuum stored in ***flux*** is multiplied by these factors in the same subroutine.

3.3.5 Rayleigh scattering

Clouds with neutral hydrogen column densities greater than ~ 10^{23} cm^{-2} are optically thick to Rayleigh scattering at wavelengths near Lα, and this process is a major scattering opacity source at short wavelengths for grain-free environments.

Rayleigh scattering cross sections given by Gavrila (1967) are used, joined with expressions for the radiative damping wings of Lyman lines (Mihalas 1978). For wavelengths longward of 1410 Å a power-law fit to Gavrila's quantal calculations is used;

$$\sigma_{Ray} = 8.41\times10^{-25}\varepsilon^4 + 3.37\times10^{-24}\varepsilon^6 + 4.71\times10^{-22}\varepsilon^{14} \quad \text{cm}^2 \tag{120}$$

where $\varepsilon \equiv \nu / cR_\infty$ is the photon energy in Rydbergs. This fit is accurate to typically a percent, with occasional errors as large as 4 percent.

For wavelengths between 1410 Å and the Lyman limit, radiative broadening of the Lyman lines is assumed (Mihalas 1978);

$$\sigma_{Ray} = \sum_{i=2}^{4}\left(\frac{q_e^2\, f_{1,i}}{m_e c}\right)\frac{\Gamma / 4\pi}{\left(\nu - \nu_{1,i}\right)^2} \quad \text{cm}^2 \tag{121}$$

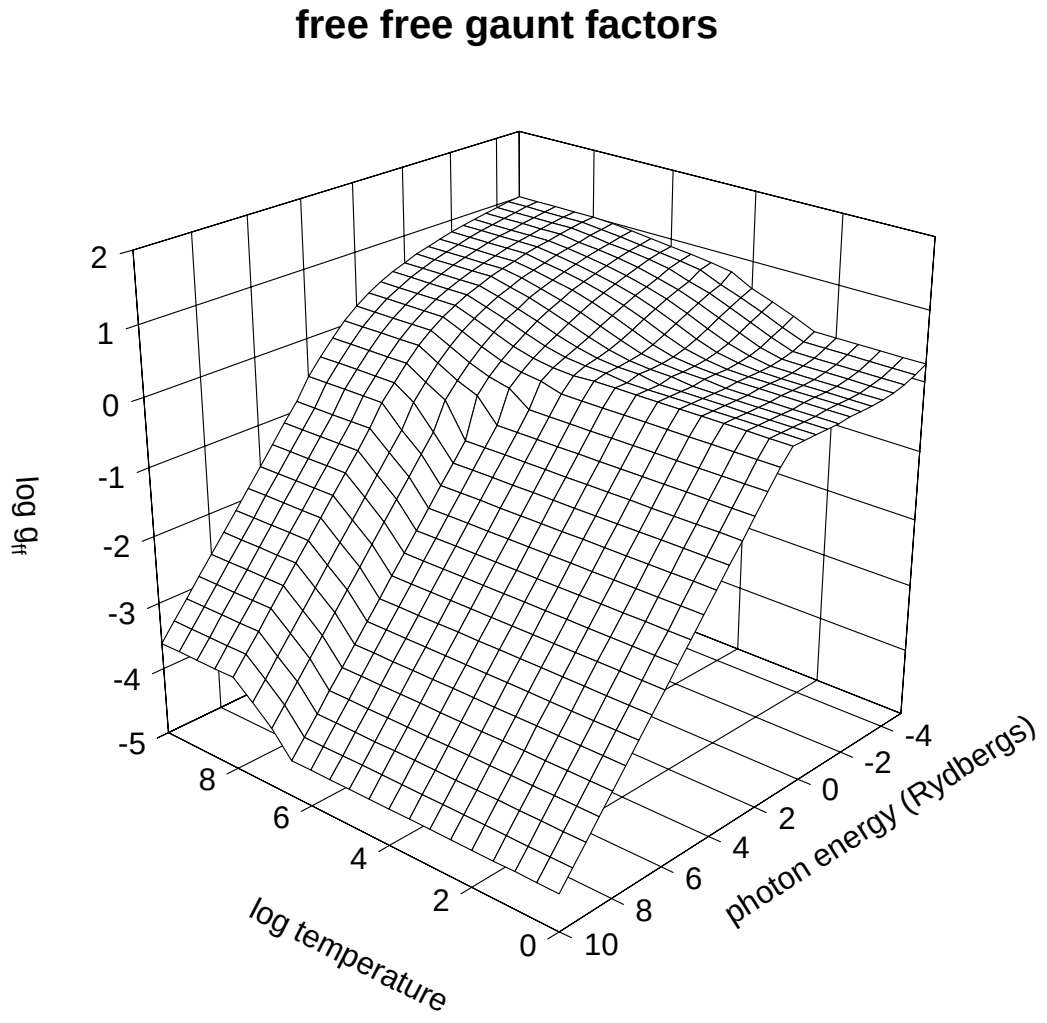

Figure 1 Thermally averaged free-free gaunt factor. The gaunt factor is shown as a function of photon energy and temperature. gaunt recool

where Γ is the reciprocal lifetime of the upper level *i* and the sum is over the first four Lyman lines. This expression gives cross sections in excellent agreement with Gavrila (1967) for these wavelengths.

3.3.6 Free-free opacity

The main opacity source in the infrared-radio spectral region for many conditions is free-free opacity with a cross section given by

$$\alpha_\nu(ff) = 3.69\times10^{8}\ \bar{g}_{III}(\nu,T)\ f(r)\,\nu^{-3}\ T^{-1/2}\left\{1-\exp\left(-h\nu\,/\,kT\right)\right\}\sum_{A}\ \sum_{z} z^{2}\ n_{A}^{+z}\quad \text{cm}^{2} \tag{122}$$

(see, for example, Mihalas 1978). The sum is over all ions n^{+z} of element *A* and over all elements. The temperature averaged gaunt factor $\bar{g}_{III}(\nu,T)$ is taken from Hummer (1988; see also Karzas and Latter 1961) and are evaluated in routine ***gffsub*** that was written by D. Hummer.

This routine did not extend to energies that could be treated by asymptotic expansions of the gaunt factor. ***gffsub*** was modified by J. Ferguson to extend over the full temperature and energy range considered by Cloudy. Figure 1 shows the gaunt factors as functions of photon energy and temperature.

3.3.7 Bound-free opacity

Continuum optical depths for photoabsorption from level *n* are given by

$$d\tau_n(\nu) = \alpha_\nu(n)\,n_n\left[1-\exp\left(-h\nu\,/\,kT\right)/\,b_n\right]\,f(r)\,\delta r \tag{123}$$

where b_n is the departure coefficient for level *n* and α_ν is the absorption cross section.

3.3.8 Plasma frequency

The plasma frequency, the energy where the index of refraction of an ionized medium goes to zero, is given by

$$\nu_{pl} = \left(\frac{n_e q_e^2}{\pi\, m_e}\right)^{1/2} = 8.978\times10^{3}\ n_e^{1/2}\ s^{-1} = 2.729\times10^{-12}\ n_e^{1/2}\ \text{Ryd}\,. \tag{124}$$

An ionized gas will reflect the incident continuum for energies smaller than this. This shielding becomes important for the energy range considered by Cloudy for electron densities greater than ~10^{12} cm^{-3}. For higher densities this process is treated by setting the intensity of the incident continuum to zero for energies below the plasma frequency, and adding this portion of the incident continuum to the reflected continuum.

4 LINE DETAILS

4.1 Overview

The effects of optical depths, continuum pumping, collisions, and destruction by background opacity, are computed for *all* permitted and intercombination lines. The cooling is usually distributed among many lines in high-density models, and these lines are usually optically thick.

4.2 Line Boltzmann Factors

The Boltzmann factor $h\nu/kT$ for a line with a known wavelength or energy is given by Table 17. The table lists the ratio $h\nu/k$ for various units of the line energy. Vacuum, not air, wavelengths, must be used for all quantities involving wavelengths.

Table 17 Line Boltzmann Factors

Line Energy Units	hν / k (K)
Angstroms	1.43877(+8) / λ(Å)
microns	1.43877(+4) / λ(μ)
wavenumbers	1.43877×σ
Rydbergs	1.5788866(+5) ×E

4.3 Optical Depths, Opacities, and Transition Probabilities

4.3.1 Optical depths

The line center optical depth for a transition *u-l*, where *u* and *l* are the upper and lower levels, is given by

$$d\tau_{l,u} = \alpha_\nu \left(n_l - n_u g_l / g_u \right) f(r)\, dr \ . \qquad (125)$$

Here $f(r)$ is the filling factor and α_ν the absorption cross section (cm^2).

The term in parenthesis is the population of the lower level, with correction for stimulated emission. This term is the only place where stimulated emission enters in the radiative balance equations (Elitzur et al. 1983) .

4.3.2 Absorption cross section

The line-center absorption cross section α_ν (cm^2) is related to the dimensionless absorption oscillator strength f_{lu} or f_{abs} by

$$\alpha_\nu = \frac{\pi^{1/2} q_e^2 \lambda\, f_{abs}}{m_e c v_{Dop}} \varphi_\nu(x) = 0.014974\, f_{abs} \frac{\lambda_{cm}}{v_{Dop}} \varphi_\nu(x) = 1.4974 \times 10^{-6}\, f_{abs} \frac{\lambda_{\mu m}}{v_{Dop}} \varphi_\nu(x) \quad \mathrm{cm}^2 \qquad (126)$$

with the relative line displacement given by

$$x \equiv \frac{\nu - \nu_o}{\Delta\nu_{Dop}} \qquad (127)$$

and $\varphi_\nu(x)$ is the Voigt function. With this definition of the relative line displacement, the line profile due to thermal motions along is exp ($-x^2$). Equation 126 is evaluated in routine ***abscf***.

4.3.3 Velocities in a thermal distribution

There are three mean speeds in a thermal velocity distribution. The ***most probable speed*** is the peak of the velocity distribution, with a value

$$v^2_{mean} = 2kT / m_A \text{ [cm s}^{-1}\text{]} . \quad (128)$$

This is found by setting the derivative of the Maxell-Boltzmann function to zero (Novotny 1973, p 122). The ***average speed*** is obtained by averaging over this function and is given by

$$v^2_{average} = 8kT / \pi \ \ m_A \text{ [cm s}^{-1}\text{]} . \quad (129)$$

The ***Doppler velocity width*** is the velocity averaged over the projected line of sight, given by

$$v^2_{Doppler} = 2kT / m_A \text{ [cm s}^{-1}\text{]} . \quad (130)$$

So it turns out that the most probable speed is equal to the Doppler width.

4.3.4 Line Widths

In equation 126 the velocity Doppler width (cm s^{-1}), the observed half-width of the line, including turbulence, is given by

$$v^2_{Dop} = 2kT / m_A + v^2_{turb} \text{ [cm s}^{-1}\text{]} \quad (131)$$

as determined by the local electron temperature. The micro-turbulent velocity v_{turb} is assumed to be zero unless it is reset with the **`turbulence`** command[1]. The Doppler width (cm s^{-1}) for each element and molecule is computed in routine ***velset***, and values are stored in the array *doppler*. The array ***doppler*** , part of the structure *DoppVel*, gives the velocity width of each element extending from hydrogen through the value of *limelm*, currently 30.

In ***velset*** the Doppler width is evaluated as

$$v_{Dop} = \sqrt{2kT / m_A + v^2_{turb}} = \sqrt{1.651\times10^8\, T / m_{AMU} + v^2_{turb}} \ . \quad (132)$$

The atomic weight in atomic mass units, m_{AMU}, is stored in the vector ***AtomicWeight***, which contains m_{AMU} for the first 30 elements.

4.3.5 Oscillator strengths

The absorption (f_{abs}, $f_{l,u}$) and emission (f_{em}, $f_{u,l}$) oscillator strengths are related by

$$g_l f_{l,u} = -g_u f_{u,l} \quad (133)$$

where the *g*'s are the statistical weights. This product is symmetric, neglecting sign, and the code tries to use *gf*'s throughout.

4.3.6 Voigt function

Optical depths a relative displacement *x* away from line center are related to the line center optical depth by

$$\tau(x) = \tau_o \ \ \varphi_\nu(x) \ . \quad (134)$$

The relative displacement is given by

$$x \equiv \frac{\nu}{\nu_{Dop}} \quad (135)$$

[1] Note that the turbulence command enters v_{turb} in km / s, but converts it into cm / s, the units used throughout the code.

where ν_{Dop} is given by equation 132. The Voigt function is normalized to unity at line center and is approximately given by

$$\varphi_\nu(x) \approx \exp(-x^2) + a/(\pi^{1/2}x^2) \quad . \tag{136}$$

4.3.7 Mean vs. line center optical depths

Cloudy tries to work with line center optical depths throughout (see, for example, Mihalas 1978). In many places routines or approximations using *mean* optical depths are encountered (e.g., Hummer and Kunasz 1980). For comparison, the line center optical depth is $\pi^{1/2}$ times *smaller* than the mean optical depth.

4.4 Optical depths and iterations

4.4.1 RTOptDepthInit

Routine ***RTOptDepthInit*** is called soon after the initial boundary conditions are established, to estimate the total line and continuum optical depths for hydrogen and helium. It uses various methods to estimate these.

4.4.2 RTOptDepthIncre

Routine ***RTOptDepthIncre*** is called once during each zone to increment the optical depth scale.

4.4.3 RTOptDepthReset

Routine ***RTOptDepthReset*** is after the iteration is complete to reset the optical depth scale.

4.4.4 lgTauOutOn

This logical variable indicates whether or not the outward optical depths have been estimated. It is false on the first iteration and true thereafter. It is part of the *opac* structure.

4.5 The Einstein Coefficients

The oscillator strength *gf* is related to the transition probability A_{ul} by

$$g_u f_{em} = \frac{mc\lambda_{cm}^2}{8\pi^2 q_e^2} g_u A_{u,l} = 1.4992 g_u A_{u,l} \lambda_{cm}^2 = 1.499\times10^{-8} g_u A_{u,l} \lambda_{\mu m}^2 \tag{137}$$

where $\lambda_{\mu m}$ is the wavelength in microns and λ_{cm} the wavelength in centimeters. Neglecting sign the absorption oscillator strength is related to the transition probability by

$$f_{abs} = \frac{mc\lambda_{cm}^2}{8\pi^2 q_e^2} \frac{g_u}{g_l} A_{u,l} = 1.4992\times10^{-8} A_{u,l} \lambda_{\mu m}^2 \frac{g_u}{g_l} \tag{138}$$

or

$$A_{u,l} = \frac{8\pi^2 q_e^2}{mc\lambda_{cm}^2} \frac{g_l}{g_u} f_{abs} = \frac{f_{abs}}{1.4992\times10^{-8}} \lambda_{\mu m}^{-2} \frac{g_l}{g_u} \quad . \tag{139}$$

Equation 139 is evaluated in routine ***eina***. Combining equations 126 and 138 we obtain an expression relating the transition probability and the absorption cross section;

$$\alpha_\nu = \frac{c^2 g_u}{8\pi\nu^2 g_l}\frac{\varphi_\nu(x)}{\pi^{1/2}\mathrm{v}_{Dop}}A_{u,l} = \frac{\lambda^2 g_u}{8\pi g_l}\frac{\varphi_\nu(x)}{\pi^{1/2}\mathrm{v}_{Dop}}A_{u,l} = 2.24484\times10^{-14}A_{u,l}\lambda_{\mu m}^3\frac{g_u}{g_l}\frac{\varphi_\nu(x)}{\mathrm{v}_{Dop}} \quad \mathrm{cm}^2 \quad . \tag{140}$$

The coefficient for induced emission, B_{ul}, is related to A_{ul} by the phase space factor $2h\nu^3/c^2$;

$$A_{u,l} = \frac{2h\nu^3}{c^2}B_{ul} \tag{141}$$

and the induced emission and absorption probabilities are related by

$$g_l B_{l,u} = g_u B_{u,l} \tag{142}$$

so that the rate of induced radiative excitation (continuum pumping) is given by

$$r_{l,u} = n_l B_{l,u} J_{l,u} = n_l A_{u,l}\frac{J}{2h\nu^3/c^2}\frac{g_u}{g_l} = n_l A_{u,l}\eta_{l,u}\frac{g_u}{g_l} \tag{143}$$

where η is the continuum occupation number at the line energy. Similarly the rate of induced radiative de-excitation is related by detailed balance,

$$r_{u,l} = r_{l,u}\frac{g_l}{g_u} \quad . \tag{144}$$

The absorption cross section α_ν is related to $B_{l,u}$ by

$$\alpha_\nu = \frac{h\nu}{4\pi}B_{l,u} \quad \mathrm{cm}^2 \, .$$

In these terms the optical depth increment (equation 125) is given by

$$d\tau_{l,u} = \alpha_\nu\left(n_l - n_u g_l/g_u\right)f(r)dr = B_{l,u}\frac{h\nu}{4\pi}\left(n_l - n_u g_l/g_u\right)f(r)dr \quad . \tag{145}$$

4.6 The Line Source Function

The source function for a line is defined as

$$S_\nu(T_{exc}) \equiv B_\nu(T_{exc}) \equiv \frac{j_\nu}{\kappa_\nu} = \frac{A_{u,l}n_u}{B_{l,u}\left(n_l - n_u g_l/g_u\right)} \quad \mathrm{erg\ Hz^{-1}\ sr^{-1}\ s^{-1}} \tag{146}$$

where T_{exc} is the line excitation temperature (see equation 188, page 228), and $B_\nu(T_{exc})$ is the Planck function at the line excitation temperature. Combining the definitions of the Einstein relations we find the relation

$$S_\nu(T_{exc}) = \frac{2h\nu^3}{c^2}\frac{n_u/g_u}{\left(n_l/g_l - n_u/g_u\right)} \quad . \tag{147}$$

4.7 The Line Escape Probability Functions

At low densities, line scattering for a two-level atom is coherent in the atom's reference frame, and the line profile function is described by the incomplete redistribution function. At high densities the Stark effect can broaden the line. When the radiation density is high, scattering within excited states can inhibit the broadening of resonance lines such as Lβ (line interlocking), destroying the coherence of the scattering process. In these cases complete redistribution in a

Doppler core more closely describes the scattering process. Cloudy uses two escape probability functions to take these processes into account. Strong resonance lines are treated with partial redistribution with a Voigt profile. Subordinate lines are treated with complete redistribution in a Doppler core.

4.7.1 Escape probability routines

Three routines compute the fundamental escape probabilities, and are all located within the file *rtescprob.c*. These are ***esccom***, ***escinc***, and ***escla***. They compute escape probabilities for complete redistribution (either with or without the damping wings), incomplete redistribution, and Lα. A separate routine, ***escmase***, is called by these to compute escape probabilities when the optical depth is negative. These routines are called by higher-level line transfer routines throughout the code.

4.7.2 Incomplete redistribution

Incomplete redistribution is assumed for resonance transitions such as C IV λ1549 and the Lα transitions of hydrogen and helium. Two studies of line formation using this approximation are those of Bonilha et al. (1979) and Hummer and Kunasz (1980). Both studies suggest escape probabilities of the form

$$P_l(\tau) = \left\{1 + b(\tau)\tau\right\}^{-1} \qquad (148)$$

but there is substantial disagreement in the form and value of the factor $b(\tau)$, sometimes by more than a factor of 2. (This is after due allowance for the different definitions of line opacities in the two papers.) Cloudy uses the Hummer and Kunasz (1980) results for H I, He I, and He II Lα and strong resonance lines such as C IV λ 1549. Their tabulated values were fitted by interpolation.

4.7.3 damping constant

The damping constant a is given by

$$a = \frac{\Gamma}{4\pi\,\Delta\nu_D} = \frac{\lambda_{cm}\sum A}{4\pi\,v_{Dop}} = \frac{\lambda_{cm}\sum A\,7.958\times10^{-2}}{v_{Dop}} = \frac{\lambda_{\mu m}\sum A\,7.958\times10^{-6}}{v_{Dop}} \qquad (149)$$

where Γ is the sum of the A's from the upper level, and $\Delta\nu_D$ is the Doppler width in frequency units (Mihalas 1978), λ_{cm} and $\lambda_{\mu m}$ are the wavelengths in cm and microns respectively, and v_{Dop} is the Doppler width in cm s^{-1}. The ratio $\Gamma\lambda/4\pi$ is stored in the line vectors. The a's are then evaluated in the routines deriving the escape probabilities.

4.7.4 Background opacity and Destruction probability

The ratio of continuous to total opacity is X_c parameterized as

$$X_c = \frac{\sum \kappa_c\, n_c}{\kappa_l n_l + \sum \kappa_c\, n_c} \qquad (150)$$

where the κ_l's are the line center absorption opacities and the n's the number of absorbers.

Destruction probabilities are computed in routine ***eovrlp***.

4.7.5 Complete redistribution

Lines arising from excited states (hydrogen Balmer, Paschen, etc.) and Lyman lines with $n_u > 2$ are treated assuming complete redistribution in a Doppler core (i.e., the damping constant *a* is assumed to be zero). In this case, if the total optical depth of the slab is *T*, then the escape probability at a depth τ from the illuminated face is given by;

$$P_{u,l}(\tau,T,X_c)=\left[1-X_cF(X_c)\right]\frac{1}{2}\left[K_2(\tau,X_c)+K_2(T-\tau,X_c)\right] \quad , \tag{151}$$

and the destruction probability is

$$D_{u,l}(X_c)=X_cF(X_c)\,. \tag{152}$$

The function is

$$F(X_c)=\int_{-\infty}^{\infty}\frac{\varphi(x)}{X_c+\varphi(x)}\,dx \quad , \tag{153}$$

where in these expressions (and in this part of the code) the *mean opacity is used*, and $\varphi(x) \approx \pi^{1/2} \exp(-x^2)$ is the Voigt function. $F(X_c)$ is interpolated from the tables presented by Hummer (1968). The function

$$K_2(\tau,X_c)\equiv\frac{1}{1-X_cF(X_c)}\int_{-\infty}^{\infty}\frac{\varphi^2(x)}{X_c+\varphi(x)}E_2\left[\left(X_c+\varphi(x)\right)\tau\right]d\tau \tag{154}$$

is evaluated numerically.

4.7.6 Masing lines

A line mases when its optical depth is negative. Routine ***escmase*** evaluates this escape probability as (Elitzur 1992; p 32)

$$\beta(\tau)=\frac{1-\exp(-\tau)}{\tau} \quad . \tag{155}$$

The code will generate a comment if strong maser action occurs for any transition.

4.7.7 Continuum fluorescence

Continuum fluorescence is treated as in Ferland and Rees (1988) and Ferland (1992).

Consider the case of a continuum that has been attenuated by photoelectric (and all other) opacity sources. The transmitted continuum has a flux of photons φ_ν (photons cm^{-2} s^{-1} Ryd^{-1}). Continuum pumping is included among the general line excitation processes for all lines considered by the code.

The photon occupation number of the attenuated continuum is given by

$$\eta_\nu=\varphi_\nu\,\frac{c^2}{8\pi\,\nu_1^3\,\nu_{Ryd}^2} \tag{156}$$

where ν_{Ryd} is the frequency in Rydbergs, ν_1 is the frequency of 1 Rydberg, and the other symbols have their usual meaning. The rate ions are excited from a lower level with population n_l (cm^{-3}) is then given by

$$r_{l,u} = A_{u,l} \frac{g_u}{g_l} \eta_\nu \gamma_{l,u} n_l \qquad (157)$$

where $A_{u,l}$ is the transition rate and the g's are the statistical weights. In this expression $\gamma_{l,u}$ is the probability that continuum photons penetrate a line-center distance τ_o and are then absorbed by an atom:

$$\gamma_{l,u} = \int_0^\infty \varphi_\nu \exp\left(-\tau_o \varphi_\nu\right) d\nu \; / \int_0^\infty \varphi_\nu \, d\nu \; . \qquad (158)$$

where, in this expression only, φ_ν is the Voigt function. Figure 2 shows $\gamma_{l,u}$ for a wide variety of values of the damping constant *a*.

4.7.8 Stark broadening

Distant collisions with charged particles broaden the upper levels of lines, and in the limit of very high densities this will make the scattering process completely non-coherent even for Lα (i.e., complete redistribution obtains). Cloudy closely follows the treatment of Puetter (1981) in treating Stark broadening. For transitions described by incomplete redistribution a total escape probability $P_{l,\,tot}$ given by

$$P_{u,l} = \min\left(P_{inc} + P_{Stark} \; , P_{com}\right) \qquad (159)$$

is defined, where the escape probabilities are those for incomplete, Stark, and complete redistribution respectively. The total effective escape probability is not allowed to exceed the complete redistribution value for $\tau > a^{-1}$.

4.7.9 Net escape probability

If τ is the optical depth in the direction towards the source of ionizing radiation and T is the total optical depth computed in a previous iteration, then the escape probability entering the balance equations is

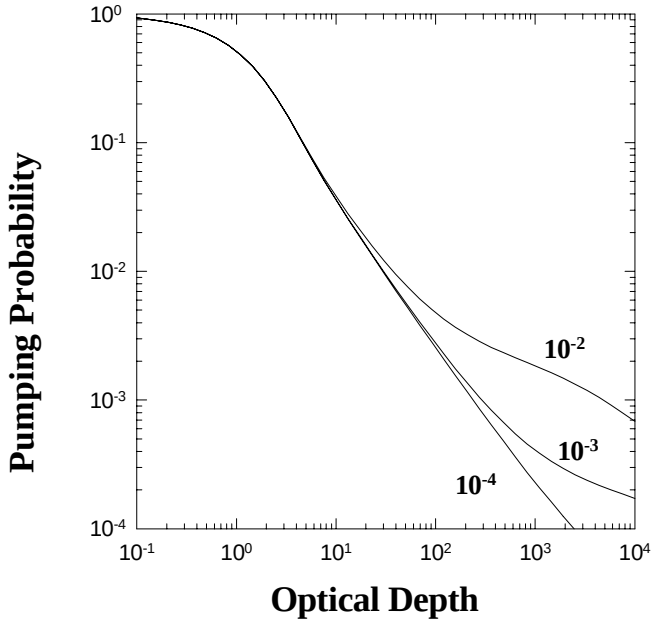

Figure 2 This figure shows the probability that a photon will penetrate to the line center optical depth shown on the x-axis, and then be absorbed by the line. The curves are for various values of the damping constant *a* (the ratio of damping width to Doppler width), as indicated on the figure. ppump

$$P_{u,l}(\tau,T)=\left\{P_{u,l}(\tau)+P_{u,l}(T-\tau)\right\}/2 \quad . \tag{160}$$

In general the total optical depth T is only known after the first iteration, so more than one iteration must be performed when radiative transfer is important.

4.8 Level populations

Both escape and destruction probabilities enter in the calculation of a level population and line emissivity. The escape probability $P_{u,l}$ is the probability that a line photon will escape in a single scattering (Elitzur et al. 1983; Elitzur 1984). The destruction probability $D_{u,l}$ is the probability that a line photon will be destroyed in a single scattering.

The radiative line de-excitation rate is given by

$$\left(\frac{dn_u}{dt}\right)_{rad}=n_u A_{u,l}\left(P_{u,l}+D_{u,l}\right)-n_l A_{u,l}\eta\gamma_{u,l} \tag{161}$$

where η is the photon occupation number of the attenuated external radiation field and $\gamma_{u,l}$ is the fluorescence probability.

The net emission from a transition between the level n to a lower level l is then simply

$$4\pi\, j(n,l)=n_n A_{n,l}\, h\nu_{n,l}\, P_{u,l}(\tau_{n,l})\, f(r) \tag{162}$$

where $f(r)$ is the filling factor. The local cooling rate (erg cm^{-3} s^{-1}) due to the line is related to the level populations by

$$\Lambda_{u,l}=\left(n_l C_{l,u}-n_u C_{u,l}\right) f(r)\, h\nu \tag{163}$$

and the local flux (cm^{-2} s^{-1}) of "on-the-spot" (OTS) photons caused by line loss (used to compute heating or photoionization rates for the sources of the background opacity) is

$$\varphi_{OTS}=\frac{n_u A_{u,l} D_{u,l}(X_c)}{\sum \kappa_c\, n(c)} \quad . \tag{164}$$

The ratio of inward to total line intensity is then given by

$$\frac{4\pi\, j(in)}{4\pi\, j(total)}=\frac{P_{u,l}(\tau)}{\left[P_{u,l}(\tau)+P_{u,l}(T-\tau)\right]} \quad . \tag{165}$$

4.9 Optical Depths and the Geometry

The terms open and closed geometry are defined in a section in Part I. The treatment of transfer in these two limits is described here.

4.9.1 Open geometry

This is the default. During the first iteration the line escape probability is defined using only optical depths accumulated in the inward direction. This optical depth is initialized to a very small number, at the start of the calculation. At the end of the first iteration the total optical depth is set to the optical depth accumulated in the inward direction in routine ***RTOptDepthReset***. At the end of subsequent iterations the total optical depth is defined as a mean of the new and old inward optical depths.

4.9.2 Closed geometry overview

Continuum photons are assumed to interact with gas fully covering the continuum source. At the end of the first iteration the total continuum optical depths are set equal to twice the computed optical depths, and the inner optical depths reset to the computed optical depths. The same recipe is followed on subsequent iterations, except that means of old and computed optical depths are used.

Closed expanding geometry This is the default if the **`sphere`** command is entered. In this case it is assumed that line photons do not interact with lines on the "other" side of the expanding spherical nebula. The treatment of the optical depths is entirely analogous to that described for an open geometry, since the presence of the distant material has no effect on line transfer.

Closed static geometry This is assumed if the **`sphere static`** command is entered. In this case line photons from all parts of the spherical shell do interact. As a result, the optical depth scale is poorly defined on the first iteration, and more than one iteration is required. On second and later iterations the total line optical depth is set to twice the optical depth of the computed structure, and the optical depth at the illuminated face of the shell is set to half of this. The optical depth scale is only reliably defined after at least a second iteration.

4.9.3 Wind

The model is a large velocity gradient ($v \propto R$ Sobolev approximation) wind. This is described further on page 302.

4.10 Collision Strengths

I have tried to follow the Opacity Project notation throughout this document (Lanzafame et al. 1993). The energy specific collision strength Ω_{lu} for a transition between upper and lower levels u and l is related to the excitation cross section Q_{lu} (cm^2) by

$$Q_{lu} = \frac{\pi \Omega_{lu}}{g l k_{lu}^2} \tag{166}$$

where k_{lu}^2 is the wavenumber of the collision energy. If the collisions are with thermal electrons having a Maxwellian velocity distribution *f(v)* and velocity *v* then the rate coefficient q_{lu} is given by

$$q_{lu} = \int_0^\infty f(v) v Q_{lu}\, dv = \frac{2\pi^{1/2}\hbar^2}{g_l m_e} a_o \left(\frac{R_\infty}{kT}\right) \Upsilon_{lu} \exp\left(-\frac{E_{lu}}{kT}\right) \sqrt{\frac{2kT}{m_e}} \quad . \tag{167}$$

E_{ul} is the transition energy in Rydbergs, a_o is the Bohr radius,

$$a_o = \frac{\hbar^2}{m_e q_e^2} = 0.529177249 \times 10^{-8} \text{ cm} \tag{168}$$

and R_∞ is the Rydberg energy. Then the thermally averaged collision strength is given by

$$\Upsilon_{lu} = \int_0^\infty \Omega_{lu} \exp\left(-\frac{\varepsilon}{kT}\right) d\left(\frac{\varepsilon}{kT}\right) \quad . \tag{169}$$

The rate coefficient for collisional de-excitation is then given by

$$q_{ul} = \frac{Y}{g_u\sqrt{T_e}}\left(\frac{2\pi}{k}\right)^{1/2}\frac{\hbar^2}{m_e^{3/2}} = \frac{Y 8.6291\times10^{-6}}{g_u\sqrt{T_e}} \ \ \mathrm{cm^3\ s^{-1}}. \tag{170}$$

The rate coefficient for excitation follows from detailed balance:

$$q_{lu} = q_{ul}\frac{g_u}{g_l}\exp(-\chi) = \frac{Y 8.6291\times10^{-6}}{g_l\sqrt{T_e}}\exp(-\chi) \ \ \mathrm{cm^3\ s^{-1}}. \tag{171}$$

4.11 Born Approximation

For energies much larger than the excitation energy of the transition, the Born approximation is valid and the energy specific collision strength is given by Bethe (1930)

$$\Omega_{lu} \approx \frac{4 g_l f_{lu}}{E_{lu}}\ln\left(\frac{4\varepsilon}{E_{lu}}\right) \tag{172}$$

where f_{lu} is the absorption oscillator strength of the permitted transition.

4.12 The g-bar Approximation

4.12.1 The van Regemorter approach

The g-bar or van Regemorter (1962) approximation relates the collision strength to the transition probability A_{ul} and wavelength λ (in microns). Here, the collision strength for the downward transition Y_{ul} is approximately given by

$$\begin{aligned} \Upsilon_{u,l} &= \frac{2\pi}{\sqrt{3}}\frac{m^2e^2}{h^3}\lambda_{\mu m}^3 10^{-12} g_u A_{u,l}\bar{g} \\ &\approx 2.388\times10^{-6}\lambda_{\mu m}^3 g_u A_{u,l}\bar{g} \\ &\approx 159\lambda_{\mu m} g_l f_{abs}\bar{g} \end{aligned} \tag{173}$$

where g_u and g_l are the statistical weights of the upper and lower levels and f_{abs} is the absorption oscillator strength. For energies of interest in astrophysical plasmas, where $kT<h\nu$, $\bar{g}$ is approximately given by

$$\bar{g} \approx \begin{cases} 0.2; & \text{positive ions} \\ (\mathrm{kT}/\mathrm{h}\nu)/10; & \text{neutrals} \end{cases} \tag{174}$$

(van Regemorter 1962). These approximations are generally accurate to better than 1 dex.

4.12.2 The g-bar implementation

Far better collision data are available today. Dima Verner's routine, ***ColStrGBar***, uses the best available data to generate collision strengths for the transferred emission lines, using data stored in the line array. The array element ***ipLnCS1*** points to stored information identifying the type of transition.

4.13 The Critical Density

The critical density is defined as the density at which the radiative de-excitation rate $A_{ul}\,P_{ul}$ (A is the transition probability and P is the escape probability) equals the collisional de-excitation rate $q_{ul}n_e$. Setting

$$A_{ul}\;\;P_{ul} = C_{ul} = q_{ul}n_e = Y\,\frac{8.629\times10^{-6}}{g_u\sqrt{T_e}}\,n_e \qquad (175)$$

where Y is the thermally averaged collision strength, the critical density is given by

$$n_{crit} = \frac{A_{ul}P_{ul}g_u\sqrt{T_e}}{Y\,8.629\times10^{-6}}\;\;\text{cm}^{-3}. \qquad (176)$$

For an optically allowed transition, in which the g-bar approximation may apply, this density is approximately given by

$$n_{crit} = \frac{4.8\times10^{10}\sqrt{T_e}}{\lambda_{\mu m}^3\,\overline{g}}\;\;\text{cm}^{-3}. \qquad (177)$$

4.14 Thermalization Length

Radiative transfer will affect the thermal equilibrium of the gas when the collision time scale approaches an effective lifetime $\tau \sim (A_{ul} / N_{scat})^{-1}$, where A_{ul} is the transition probability and N_{scat} is the number of scatterings a line photon undergoes before escape. For permitted metal lines (which often have optical depths ~ 10^4 – 10^6) line thermalization becomes important at densities $n_e > 10^{15} / \tau \sim 10^{10}$ cm^{-3}. These effects are important for hydrogen at considerably lower densities. Additionally, continuum transfer affects the ionization and thermal equilibrium of the gas at all densities.

4.15 Averaging Levels into Terms

4.15.1 Collision strengths

Often cases are encountered in which a multiplet consisting of many lines can be treated as the equivalent two-level atom with a single transition. In these cases it is necessary to define effective collision strengths and transition probabilities. If the collision strength from an individual level i is Υ_i, and the statistical weights of the level and term are g_i and g_{tot} respectively, then the effective collision strength Υ_{eff} is related to Υ_i by a simple argument. The collision rate q_i is proportional to the ratio

$$n_i\,q_i \propto n_i\,\frac{\Upsilon_i}{g_i} \qquad (178)$$

so that

$$n_{tot}\,q_{tot} = \sum_i n_i\,q_i \propto \sum_i n_i\,\frac{\Upsilon_i}{g_i}\;\;. \qquad (179)$$

In many cases it is valid to assume that the levels within the term are populated according to their statistical weight, viz.,

$$n_i = n_{tot} \frac{g_i}{g_{tot}} \quad . \tag{180}$$

Then, the effective collision strength Υ_{tot} is operationally defined by the relations

$$n_{tot} \frac{\Upsilon_{tot}}{g_{tot}} = \sum_i n_i \frac{\Upsilon_i}{g_i} = n_{tot} \sum_i \frac{g_i}{g_{tot}} \frac{\Upsilon_i}{g_i} = n_{tot} \frac{\sum_i \Upsilon_i}{g_{tot}} \quad . \tag{181}$$

So, the effective collision strength of the entire multiplet is

$$\Upsilon_{tot} = \sum_i \Upsilon_i \quad . \tag{182}$$

4.15.2 Transition probabilities

Under similar circumstances an effective transition probability A_{eff} may be defined as

$$n_{tot} A_{tot} = \sum_i n_i A_i = n_{tot} \sum_i \frac{g_i}{g_{tot}} A_i \tag{183}$$

so that the effective transition probability is

$$A_{tot} = \sum_i \frac{g_i}{g_{tot}} A_i \quad . \tag{184}$$

So collision strengths are added, and transition probabilities averaged.

4.16 The Line Structures

4.16.1 Overview

Each emission line is represented as an ***EmLine*** structure containing all the details needed to transfer a line and predict its intensity. This structure will evolve into an object in C++. The goal is for there to be only one emission line in Cloudy, but millions of instances of it. This ***EmLine*** structure is defined in *cddefines.h*. There are two 1-D arrays of ***EmLine*** structures to contain the level 1 and level 2 lines (defined below) and multidimensional arrays of ***EmLine*** structures describe the hydrogenic, He-like, and FeII atoms.

4.16.2 The main line structures

Level 1 Lines: *TauLines* This array contains the lines with high-quality atomic data.

Level 2 Lines: *TauLine2* This is the large group of lines brought in by Dima Verner. These lines have Opacity Project wavelengths, generally accurate to about 10%. All have g-bar collision strengths (Gaetz & Salpeter 1983; Mewe 1972; van Regemorter 1962), generally thought to be accurate to about 0.5 dex.

Hydrogenic ions: *HydroLines* These contain the lines of the hydrogen-like isoelectronic sequence. The array indices give the atomic number, and upper and lower level.

Helium-like ions: *HeLike* These contain the lines of the helium-like isoelectronic sequence. The array indices give the atomic number, and upper and lower level.

4.16.3 Evaluation of stored quantities

The line structures store information dealing with the solution of the equations of statistical equilibrium, and rates related to the line transfer. Quantities dealing with the populations are evaluated in the routine that computes the level populations, and this depends on the individual lines. Quantities dealing with the line transfer are evaluated in routine ***RTMake***, which calls either ***RTMakeStat*** (for static solutions) or ***RTMakeWind*** (for a large velocity gradient model).

4.16.4 Contents of the EmLine structure

int iRedisFun ; This indicates the type of line redistribution function to be used, for level 1 lines only. Valid values are -1 and +1. If the value is positive then incomplete redistribution is used. If it is negative then complete redistribution in a Doppler core (Hummer's 'K2' function) is used.

int ipCont ; This is the pointer to line within continuum array

int IonStg; ion stage of element, 1 for atom, 2 ion, etc

int nelem; atomic number of element, 1 for H, 2 for He, etc

float TauCon ; The line optical depth to the continuum source.

float ColUL; Collision rate from upper to lower level.

float TauIn , TauTot ; The inward and total line optical depth through the cloud. TauTot was computed in the previous iteration and is not defined on the first iteration.

float FracInwd; The *fraction* of the line escaping in the inward direction. This is between 0 and 1.

float pump ; This is the local rate of lower to upper continuum pumping for the transition. It is the product of the local continuum and the pumping probability, given by

$$TauArray.ipLnPump = A_{u,l}\left(\frac{g_u}{g_l}\right)P\eta \qquad (185)$$

where η is the occupation number of the attenuated continuum, and P the line pumping probability.

double xIntensity ; line intensity

float phots; number of photons emitted per sec in the line

float gf ; gf value

float Pesc , Pdest; The escape and destruction probabilities for the line.

float damp, damprel ; The damping constant, and a number related to it. The ratio $\Gamma\lambda/4\pi$, used to derive the damping constant. For a two level system this is just $A_{ul}\lambda/4\pi$. This is given by

$$TauArray.ipLnDamp\,\mathrm{Re}\,l = 531 f_{abs}\lambda_{\mu m}\frac{g_l}{g_u} \quad . \qquad (186)$$

float dTau; total opacity (cm^{-1}) in transition

double cool , heat; cooling and heating due to collisional excitation

float ColOvTot; ratio of collisional to radiative excitation

float cs; collision strength for transition

float WLAng; The wavelength (Å) of the line as used in the print out of the line optical. This number is only a label and can be an air wavelength.

float EnergyK; transition energy in degrees kelvin

float EnergyRyd; transition energy in Rydberg

float EnergyErg; ergs

float EnergyWN; transition energy in wavenumbers

float opacity; line opacity

float gLo , gHi ; These are the statistical weights of the lower and upper levels.

float PopLo , PopHi; These are the lower and upper level populations (cm^{-3}) for the transition.

float PopOpc The correction for stimulated emission is included in the optical depth scale for all lines of the heavy elements. The effective population determining the optical depth scale is given by the population stored here, computed as

$$n_l^{eff} = n_l - n_u \frac{g_l}{g_u} \quad . \tag{187}$$

float Aul ; transition probability, Einstein A upper to lower

float AovTot ; ratio *A21/(A21+C21)*

float CS1, CS2 These indicates the type of transition, and is used when the Mewe or Verner g-bar routines are used as the source of the collision strengths. If ***CS1*** is zero then the line is a "high quality" or "level 1" transition, and has its own pointer to the OTS line array. If ***CS1*** is not zero, (a "level 2" transition) then the collision strength is generated from the contents of ***CS1*** and ***CS2***.

float ots; ots rate

4.16.5 Dumping the line array.

The contents of the line array can be printed by calling routine ***DumpLine***, with the single argument being a pointer to the line optical depth array.

4.16.6 Generating a line label

Two functions can be used to generate a designation for an emission line using the information stored in the line arrays. A 10-character function, ***chLineLbl***, will generate a label for an emission line. This label is the spectroscopic designation for a line, such as C 4 1549Å. It is called with a single argument, the line array.

The spectroscopic designation of the ion by itself ("C 4", "O 6", etc) can be obtained from the 4 character function ***chIonLbl***. It is called with a single argument, the line array.

chLineLbl is surprisingly slow and should be used as sparingly as possible.

4.16.7 Line excitation temperature

Routine ***TexcLine*** will use the contents of the line array to generate the line excitation temperature. The line excitation temperature T_{exc} is operationally defined from the relative level populations n_u and n_l and the line energy $h\nu$ as

$$\frac{n_u / g_u}{n_l / g_l} = \exp\left(-h\nu / kT_{exc}\right) \quad . \tag{188}$$

Routine ***TexcLine*** uses the contents of the line arrays to evaluate T_{exc} as

$$T_{exc} = -t(ipLnBolt) / \log\left(\frac{t(ipLnPopu) / t(ipLnGu)}{t(ipLnPopl) / t(ipLnGl)}\right) \tag{189}$$

if both populations are positive. The routine returns an excitation temperature of zero if either population is non-positive.

4.16.8 A Simple Two Level Atom

The following code fragment uses the information in the line optical depth arrays to compute the population of a two level atom. The treatment includes pumping by the attenuated external radiation field, collisional excitation and deexcitation, and photon escape and destruction by background opacity. To see more examine routine *level2* within the code.

```
#include "cddefines.h"
#include "taulines.h"
/* following includes variables te and eden, the electron
 * temperature and electron density*/
#include "phycon.h"
/* following contains abundances of all ions
 * following includes sqrte, the square root of te*/
#include "tepowers.h"
void ComputeIt( EmLine *t )
{
        /* net rate down A21*(escape + destruction) */
        Aul = t->Aul*(t->Pesc + t->Pdest);

        /* statistical weights of upper and lower levels */
        gl = t->gLo;
        gu = t->gHi;

        /* get Boltzmann factor */
        boltz = sexp(t->EnergyK/phycon.te);

        /* upward pumping by external continuum */
        PumpLU = t->pump;
        /* downward pumping by external continuum */
        PumpUL = PumpLU * gl / gu;

        /* collisions from lower to upper, and upper to lower */

        /* collisions from upper to lower */
        Cul =  8.629E-6 / tepowers.sqrte * t->cs * phycon.eden / gu;

        /* collisional excitation
         * sexp is special form of exp that sets zero if very small */
        Clu = Cul *  gu/gl * sexp(-boltz);

        /* xIonFracs(nelem,i) is density of ith ionization stage (cm^-3) */
        Abun = xIonFracs[t->IonStg][ t->nelem -1];

        /* this is ratio of upper to lower level population
        ratio = (Clu+PumpLU) / ( Cul+PumpUL+Aul )
        /* uppper level population */
        upper = Abun / (1. + 1./ratio);
}
```

4.16.9 Adding lines to the level 1 line arrays

The file *level1.dat***.** The list of level 1 lines is contained in the file *level1.dat*, which lives in the main data directory. This file contains the information needed to set up all the level 1 lines, and is edited to add more files. Comments may be entered

anywhere within the file, and are indicated by a sharp symbol ("#") in the first column. The order of the parameters for each line is described in the file.

The file begins with a magic number that must be changed when the file is changed. If the contents of the data file are changed then both this magic number and the parallel code in ***CreateData*** must be changed.

Routine ***CreateData*** reads the file *level1.dat*. This routine first counts how many level 1 lines are contained in the file and then allocates space for the emission line structure.

Array elements for the TauLines array. The level 1 lines are contained in *TauLines*, an array of structures of type *EmLine*. The header file *cddefines.h* contains the declaration for a long list of integer indices that are used to address elements of the *TauLines* array. The definition of this set of integers is in routine ***CreateData.***

MakeLevLines After ***CreateData*** reads in the contents of the *level1.dat* data file, it calls ***MakeLevLines*** to establish the array indices. This routine uses the line wavelength, chemical element, and ionization stage to associate an array index with each line.

Follow these steps:

- **Add the line to the file level1.dat that lives in the data directory.** All level 1 lines are contained in the file *level1.dat*. The file describes the format of the data. Each emission line is contained on a single line, which has a line label, wavelength, excitation energy, statistical weights of the upper and lower levels, either the *gf* or *A* for the transition, and the type of redistribution function. The code will count how many emission lines are present in level1.dat and allocate the appropriate space.
- **Enter the line in routine CreateData.** The level 1 lines are an array of structures that are defined in *createdata.c* and declared in *cddefines.h*. A series of integer variables give the array index for each line. Initially these indices are set to very large negative values.
- **Associate the line with an array index in MakeLevLines.** This routine has a series of call to ***ipFindLevLine***, which takes the line wavelength, ionization stage and element number as arguments. ***ipFindLevLine*** returns the index to the emission line with the array of level 1 lines. ***MakeLevLines*** confirms that all array indices entered in ***CreateData*** are given valid indices here.
- **Compute the line intensity and cooling.** This is done by calling one of the line cooling routines, ***level2***, ***level3***, etc. It will be necessary to assign a collision strength to the transition. This can be done by calling ***PutCS***, a routine with two arguments, the collision strength and the line vector.
- **Add the line to the line output routine.** This is done in one of the members of the ***lines*** Family of routines. A call to routine ***PutLine***, which has as a single argument the line structure, will enter all of the needed information about the line production in the current zone.
- **Recompile** Cloudy

Table 18 Needed Line Parameters

Label	λ	g_l	g_u	gf	E(σ)	Ion	Nelem	Redis	A_{ul}
	ipLnWlAng	ipLnGl	ipLnGu	ipLnGF	ipLnEnrWN	ipLnIonStg	ipLnNelem	ipLnRedis	ipLnAul

label a four character string that will identify the line in the printout.

λ This is the line wavelength in Ångstroms or microns, and is only used as a line label. It can be an air wavelength.

g_l, g_u Lower and upper statistical weights.

gf, A It is only necessary to specify either the *gf* or *A*. If the transition probability is to be entered instead of the *gf*, the *gf* must be assigned a value of zero. If *gf* is specified then *A* does not need to be set.

E(σ) This is the line energy in wavenumbers, and is used to generate Boltzmann factors.

Redis This must be non-zero. Negative values indicate complete redistribution with a Doppler core, and positive values incomplete redistribution.

5 THE MODEL ATOM FOR HYDROGEN-LIKE SPECIES

5.1 Overview

Cloudy is designed to model environments that range from the low-density limit to LTE. The hydrogenic isoelectronic series is treated as a multi-level atom plus continuum. Tests in the low-density, or nebular, limit show that the model atom predicts level populations and emissivities that are in much better than 1% agreement with Seaton (1959), and with the Storey and Hummer (1995) results. The atom goes to LTE in the high radiation or matter density limits.

All emission lines of the hydrogen-like sequence are three-dimensional structures of type *EmLine*. The array indices, from left to right indicate the atomic number and the upper and lower level. In all these the array starts from 0, so the hydrogen Lα transition would be *EmLine[0][2][0]*.

5.2 Hydrogen Departure Coefficients

Departure coefficients, rather than actual level populations, are used in the solution of the hydrogen level populations. The LTE relative population density for level *n* is given by

$$\begin{aligned} P_n^* &= \frac{n_n^*}{n_e n_p} = \frac{g_n}{g_e g_p}\left(\frac{h^2}{2\pi\ m_e kT}\right)^{3/2} \exp\left(+\chi_n\right) \\ &= \frac{g_n}{g_e g_p} 4.1412957\times10^{-16} T^{-3/2} \exp\left(+\chi_n\right) \quad \mathrm{cm}^3 \end{aligned} \tag{190}$$

where the electron statistical weight is $g_e = 2$, all nuclear statistical weights are ignored, and $g_n = 2n^2$ is the statistical weight of hydrogen level *n*. n_n^* is the LTE population of level *n* (cm^{-3}), and the other symbols have their usual meaning. Here

$$\chi_n = \frac{I_n}{kT} = \frac{15.7807\times10^4 Z^2}{n^2 T} \tag{191}$$

where I_n is the ionization threshold for level *n* and Z is the nuclear charge, and the exponent in equation 190 is greater than one. The departure coefficients are related to the LTE relative population density by

$$b_n = \frac{n_n}{P_n^* n_e n_p} \tag{192}$$

where n_n is the actual population of the level.

5.3 Hydrogen Level Energies

Boltzmann factors for transitions between levels are defined as

$$\mathrm{HLBOLT}(l,u) \equiv \exp\left(\chi_u - \chi_l\right). \tag{193}$$

The energy sign convention is such that the Boltzmann factor is less than unity, decreasing with increasing temperature. Boltzmann factors for levels relative to the continuum are stored in the vector

$$\mathrm{HCBOLT}(n) \equiv \exp(-\chi_n) \ . \qquad (194)$$

5.4 Effective Hydrogenic Transition Probabilities

5.4.1 Einstein As

Two routines are used to compute hydrogenic transition probabilities, in the limit of a completely *l*-mixed atom. The routine ***fosc***(u, l) returns the absorption oscillator strength of the transition. Routine ***EinstA*** (u, l) drives ***fosc*** to actually obtain the transition probability. There routines were coded by Jason Ferguson, using algorithms given by Johnson (1972).

Note that the code considers the 2s and 2p as two separate levels. These routines return transition probabilities for a well l-mixed atom, and cannot be applied directly to the separate 2s and 2p levels.

5.5 Recombination Rates and Cooling

State-specific rates for radiative recombination and radiative recombination cooling are needed for the temperature range 2.8 K ≤ $T \leq 10^{10}$ K. The methods and assumptions used to derive these for hydrogenic ions are described here.

5.5.1 Formalism

The Milne relation for the state-specific radiative recombination rate coefficient ($cm^3\ s^{-1}$) to a level *n* can be expressed as (Brown and Mathews 1974; Gould 1978; Mihalas 1978);

$$\begin{aligned}\alpha_n(T) &= \left(\frac{2\pi m_e k}{h^2}\right)^{-3/2} \frac{8\pi}{c^2} \frac{g_n}{g_e g_{ion}} T^{-3/2} \int_{h\nu_o}^{\infty} \nu^2 \alpha_\nu(n) \exp\left(-h(\nu-\nu_o)/kT\right) d\nu \\ &= 4.12373\times10^{11} \frac{g_n}{g_e g_{ion}} T^{-3/2} \int_{h\nu_o}^{\infty} \nu_{Ryd}{}^2 \alpha_\nu(n) \exp\left(-h(\nu-\nu_o)/kT\right) d\nu_{Ryd}\end{aligned} \qquad (195)$$

where the *g*'s are the statistical weights of the constituents, $h\nu_{Ryd}$ is the photon energy in Rydbergs, $h\nu_o \sim z^2/n^2$ is the ionization potential in Rydbergs, $\alpha_\nu(n)$ is the photoionization cross section, and the other symbols have their usual meanings.

In implementing this formalism the fact that, for hydrogen itself, the energy scale is shifted by the ratio of the reduced mass of the nucleus to an infinite mass was explicitly taken into account. If the energy of level *n* of hydrogen is $n^{-2}\ R_H$, then the temperature corresponding to 1 Rydberg, appearing in the exponential, is 157807 K, not the commonly quoted 157890 K. This does affect the results slightly since the energy scale enters as an exponential in equation 195.

Hydrogenic photoionization cross sections are required over a very wide range of energy since recombination coefficients over a wide range of temperature are needed. Cross sections $\alpha_\nu(n)$ were calculated using a program based on routines developed by Hummer (1988) and Storey and Hummer (1991, and private communication). The program generates the cross section values at arbitrary photon energies for all hydrogenic (*n*,l) states, as well as for the total *n*, employing analytic expressions and some very accurate expansions and numerical procedures. The

Table 19 State Specific and Case B Recombination Coefficients

$\log(T_e)$	1	2	3	4	5	6	case B
0.5	9.258-12	5.087-12	3.512-12	2.684-12	2.172-12	1.825-12	5.758-11
1.0	5.206-12	2.860-12	1.974-12	1.508-12	1.220-12	1.025-12	2.909-11
1.5	2.927-12	1.608-12	1.109-12	8.465-13	6.842-13	5.737-13	1.440-11
2.0	1.646-12	9.028-13	6.216-13	4.732-13	3.811-13	3.183-13	6.971-12
2.5	9.246-13	5.055-13	3.460-13	2.613-13	2.084-13	1.720-13	3.282-12
3.0	5.184-13	2.805-13	1.888-13	1.395-13	1.085-13	8.717-14	1.489-12
3.5	2.890-13	1.517-13	9.779-14	6.884-14	5.099-14	3.912-14	6.430-13
4.0	1.582-13	7.699-14	4.555-14	2.965-14	2.053-14	1.487-14	2.588-13
4.5	8.255-14	3.461-14	1.812-14	1.076-14	6.953-15	4.775-15	9.456-14
5.0	3.882-14	1.316-14	6.059-15	3.314-15	2.022-15	1.331-15	3.069-14
5.5	1.545-14	4.196-15	1.736-15	8.918-16	5.219-16	3.335-16	8.793-15
6.0	5.058-15	1.146-15	4.392-16	2.160-16	1.229-16	7.694-17	2.245-15
6.5	1.383-15	2.760-16	1.005-16	4.807-17	2.685-17	1.660-17	5.190-16
7.0	3.276-16	6.031-17	2.129-17	1.000-17	5.523-18	3.385-18	1.107-16
7.5	7.006-17	1.227-17	4.251-18	1.976-18	1.083-18	6.606-19	2.221-17
8.0	1.398-17	2.377-18	8.139-19	3.759-19	2.052-19	1.248-19	4.267-18
8.5	2.665-18	4.455-19	1.515-19	6.970-20	3.796-20	2.303-20	7.960-19
9.0	4.940-19	8.175-20	2.769-20	1.271-20	6.913-21	4.190-21	1.457-19
9.5	9.001-20	1.481-20	5.005-21	2.294-21	1.247-21	7.552-22	2.636-20
10.0	1.623-20	2.662-21	8.985-22	4.116-22	2.235-22	1.354-22	4.737-21

calculations were carried out at a number of different mesh sizes to check for convergence. The results are typically accurate to better than 0.1 percent.

The recombination cooling rate coefficient (erg cm^3 s^{-3}) is given by

$$kT\beta(t,n) = \left(\frac{2\pi m_e k}{h^2}\right)^{-3/2} \frac{8\pi}{c^2} \frac{g_n}{g_e g_{ion}} T^{-3/2} \int_{h\nu_o}^{\infty} \nu^2 \, \alpha_\nu(n) \, h(\nu - \nu_o) \exp\left(-h(\nu - \nu_o)/kT\right) d\nu \tag{196}$$

5.5.2 Results

The numerical results are presented in Tables 19 and 20. The first column of the table gives the log of the temperature. Columns 2 through 7 give the total recombination coefficient for $1 \le n \le 6$ summed over *l* states. The last column gives the case B sum, $2 \le n \le 1000$. A very large temperature range is considered for completeness; actually, at very low temperatures three-body recombination predominates for most densities (Bates et al. 1963), while at very high temperatures other processes (i.e., Compton scattering, collisions) dominate the balance and the neutral fraction is vanishingly small.

As tests, these predictions of the recombination rate coefficients are compared with those of Seaton (1959), Ferland (1980), Hummer and Storey (1987), and Martin (1988). (Note that the total recombination rate given by Hummer and Storey is the sum of radiative and net three-body recombination. For this comparison their results for a density of 10^2 cm^{-3} were used to minimize the contribution of the second process.) The agreement with all of these results is good, usually much better than 1 percent. Seaton (1959) calculates the recombination cooling coefficients. The present results agree with his to better than 5 percent. Figure 3 shows the recombination-cooling coefficient for several states.

5.5.3 Rational approximations

It is not numerically expedient to compute these rate coefficients on-the-fly in large scale ionization / thermal structure calculations. The rate coefficients were fitted

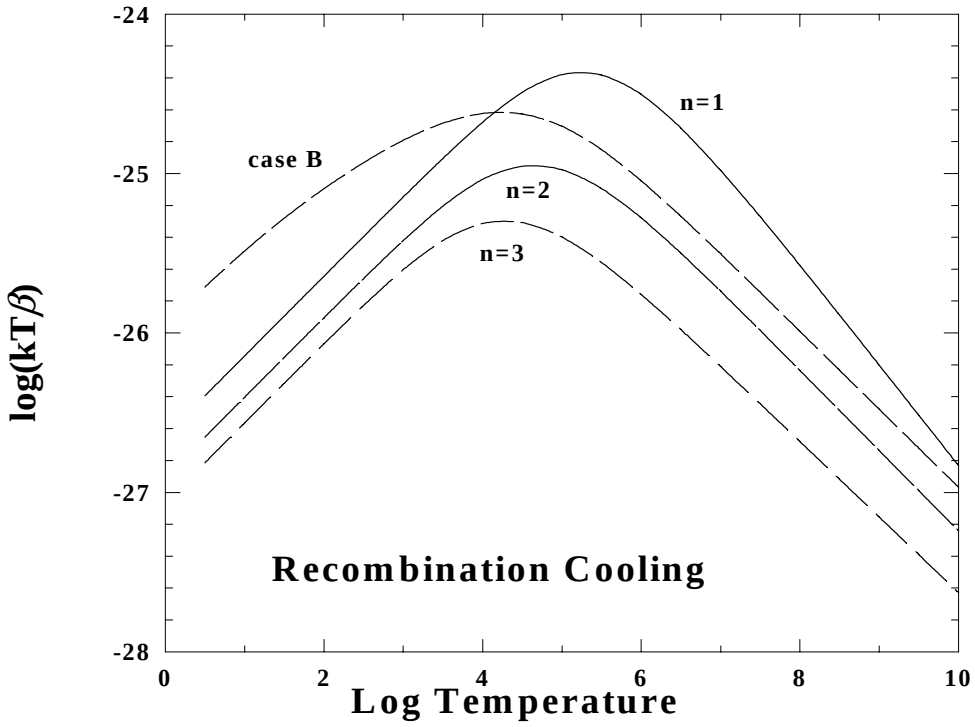

Figure 3 The recombination cooling for several states is shown as a function of temperature.

recool

with a high-order rational approximation. The recombination rate coefficient is expressed as

$$\alpha(n,T) = 10^{F(n,T)}\, T^{-1} \tag{197}$$

with

$$F(n,T) = \frac{a_n + c_n x + e_n x^2 + g_n x^3 + i_n x^4}{1 + b_n x + d_n x^2 + f_n x^3 + h_n x^4} \tag{198}$$

and $x \equiv \log(T)$. The coefficients for the expansion are given in routine ***hrcf***, which evaluates the rate. These approximations reproduce the numerical results with a

Table 20 State Specific and Case B Recombination Cooling Coefficients

$\log(T_e)$	1	2	3	4	5	6	case B
0.5	4.025-27	2.211-27	1.527-27	1.167-27	9.441-28	7.929-28	2.295-26
1.0	7.158-27	3.932-27	2.713-27	2.072-27	1.676-27	1.406-27	3.595-26
1.5	1.273-26	6.985-27	4.815-27	3.671-27	2.962-27	2.479-27	5.514-26
2.0	2.262-26	1.239-26	8.507-27	6.451-27	5.171-27	4.293-27	8.236-26
2.5	4.015-26	2.184-26	1.483-26	1.107-26	8.708-27	7.074-27	1.187-25
3.0	7.099-26	3.785-26	2.488-26	1.784-26	1.341-26	1.039-26	1.629-25
3.5	1.241-25	6.245-26	3.796-26	2.505-26	1.740-26	1.255-26	2.082-25
4.0	2.094-25	9.195-26	4.856-26	2.845-26	1.795-26	1.198-26	2.395-25
4.5	3.234-25	1.112-25	4.923-26	2.557-26	1.483-26	9.305-27	2.376-25
5.0	4.173-25	1.056-25	3.990-26	1.891-26	1.034-26	6.240-27	1.981-25
5.5	4.149-25	7.981-26	2.698-26	1.208-26	6.389-27	3.771-27	1.390-25
6.0	3.121-25	4.961-26	1.572-26	6.827-27	3.549-27	2.073-27	8.316-26
6.5	1.843-25	2.616-26	8.015-27	3.429-27	1.768-27	1.028-27	4.307-26
7.0	9.016-26	1.204-26	3.628-27	1.541-27	7.917-28	4.591-28	1.967-26
7.5	3.847-26	4.978-27	1.487-27	6.296-28	3.229-28	1.870-28	8.109-27
8.0	1.490-26	1.897-27	5.644-28	2.385-28	1.222-28	7.077-29	3.092-27
8.5	5.397-27	6.811-28	2.023-28	8.541-29	4.375-29	2.533-29	1.115-27
9.0	1.867-27	2.346-28	6.959-29	2.937-29	1.504-29	8.706-30	3.872-28
9.5	6.261-28	7.849-29	2.327-29	9.820-30	5.028-30	2.910-30	1.316-28
10.0	2.057-28	2.575-29	7.633-30	3.220-30	1.649-30	9.543-31	4.436-29

sub

mean error well below 0.1 percent. For levels below n=20 the largest error is also under 0.1 percent, although errors as large as 1.4 percent occur for the highest sum at temperatures below 100 K.

Recombination cooling coefficients were fitted to equations of the form

$$kT\beta(n,T) = 10^{F(n,T)} \tag{199}$$

where *F(T,n)* is given above, and the fitting coefficients are given in the code. The errors in fitting these coefficients are larger, typically 0.5 percent, but sometimes as large as several percent.

5.5.4 Recombination coefficients

Hydrogen recombination coefficients are stored in the three-dimensional vectors ***hrec***. The first dimension gives the charge, the next indicates the level of the model atom – ***hrec***[0][0][xx] would refer to the ground level of hydrogen. The last dimension points to several quantities related to computation of the effective recombination coefficient.

hrec[ipZ][n][0] This is the radiative recombination rate coefficient to level *n* (units $cm^3\ s^{-1}$), the term α(T,n) in equation **113**.

hrec[ipZ][n][1] This is the dimensionless OTS effective recombination efficiency, given by the term

$$\left\{P_c(n) + \left[1 - P_c(n)\right]\left(\frac{\kappa_o}{\kappa_o + \kappa_n}\right)\right\} \tag{200}$$

This term is zero deep in the cloud, and unity for an optically thin region.

hrec[ipZ][n][2] This is the continuum escape probability $P_c(n)$.

ophf These are the vectors containing the ratio of "other" to "total" opacities, which appears as the term $\kappa_o/(\kappa_o + \kappa_n)$ in equation 200.

5.6 The Collisional Rate Equations

The collision rates between two terms in strict TE are related by detailed balance[2]. Then

$$n_l^* C_{l,u} = n_u^* C_{u,l} \tag{201}$$

and we get the usual relation between collisional excitation and de-excitation rates,

$$C_{l,u} = \left(n_u^* / n_l^*\right) C_{u,l} = \left(g_u / g_l\right) \exp\left(-\chi / kT\right) C_{u,l} \quad . \tag{202}$$

Considering only collisional terms, the departure coefficient for level *n* is given by

$$\frac{db_n}{dt} = \sum_l b_l C_{n,l} + \sum_u \frac{P_u^*}{P_n^*} b_u C_{u,n} - b_n \left\{\sum_l C_{n,l} + \sum_u \frac{P_u^*}{P_n^*} C_{u,n} + C_{n,k}\left(1 - b_n^{-1}\right)\right\} \tag{203}$$

where the sums are over upper and lower levels. The collision rates (s^{-1}) from level *i* to level *j* are denoted by C_{ij}. The first term on the RHS represents collisional excitation to *n* from lower levels, the second is collisional deexcitation to *n* from

[2] The bound-bound collision rate coefficients were updated to Anderson et al. (2000) in version 95.

higher levels, and the last term accounts for destruction processes. These include collisions to lower levels, upper levels, and the continuum. The factor multiplying the collisional ionization rate $C_{n\kappa}$ accounts for collisional ionization less three-body recombination. Note that this is often a net recombination process for the atom since, under many circumstances, $b_n < 1$.

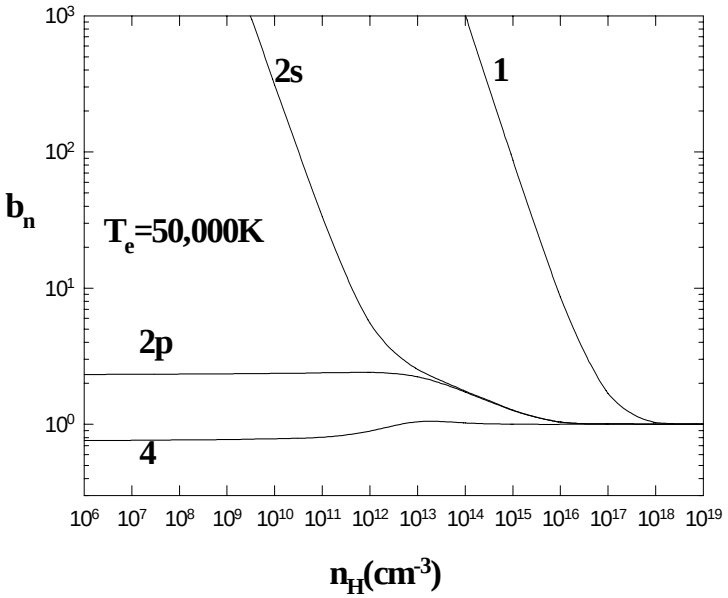

Figure 4 The equilibrium populations of the ground state and levels 2s, 2p, and 4 of the model hydrogen atom are shown as a function of the total hydrogen density n_H.. hbnvsn

Figure 4 shows a test case where collisional processes are dominant. All of the radiative processes discussed below are actually included, but the intensity of the external continuum is set to a very low (and hence negligible) value. As a result collisional and spontaneous radiative processes are dominant. The electrons are given a temperature of 50,000 K, and the level populations and ionization of the gas are determined by solving the full set of equations of statistical equilibrium. The model is of a very thin cell of gas that is optically thin in the lines and continuum. Departure coefficients for the ground state, 2s, 2p, and 4 are shown.

The radiation field is set to a very low intensity, and the column density is kept small enough for optical depth effects to be negligible. A constant electron temperature of 5×10^4 K is assumed, so the gas is primarily collisionally ionized and excited. Levels 2s and 2p do not mix until a density of nearly 10^{14} cm^{-3} is reached, and do not come into LTE until the density is nearly 100 times higher. The entire atom is nearly in LTE at densities greater than 10^{18} cm^{-3}

The ground state is overpopulated relative to its LTE value when upward collisional processes are much slower than downward radiative processes. It is only when the collisional rates approach the radiative rates that b_1 approaches unity. The 2s level also has a large overpopulation for much the same reason. It is highly metastable and accumulates a large overpopulation until 2s - 2p collisions become fast enough to mix the two l levels. The more highly excited levels ($n \geq 3$) have a behavior very similar to that of n=4, which is shown in the figure. They are under populated relative to their LTE value when radiative decays to lower levels are competitive with collisional processes. It is only at a density of $n_H > 10^{18}$ cm^{-3} that collisional processes completely dominate the rate equations and the atom reaches LTE. The mean departure coefficient at a density of 10^{19} cm^{-3} is $\overline{b_i} = 1.0007 \pm 0.0022$ for the entire atom, and the largest single deviation from unity is 0.7% (for the ground term).

5.7 The Radiative Rate Equations

5.7.1 Photoionization - recombination

The photoionization rate (s^{-1}) from level *n*, stored in the vector ***hgamnc[ipZ][n]***, is given by

$$\Gamma_n = 4\pi \int_{\nu_o}^{\infty} \frac{J_\nu}{h\nu} \alpha_\nu \, d\nu \tag{204}$$

and the induced recombination rate coefficient ($cm^3\ s^{-1}$) by

$$\alpha(ind) = P_n^* 4\pi \int_{\nu_o}^{\infty} \frac{J_\nu}{h\nu} \alpha_\nu \exp(-h\nu / kT)\, d\nu \quad . \tag{205}$$

This is evaluated at each zone by direct integration.

The ground level of the model hydrogen atom also includes destruction due to bound Compton scattering.

5.7.2 Derivation of radiative balance equations

Consider the balance for a level *n* of a three level system, with upper and lower levels *u* and *l*.

$$n_n \left(B_{n,u} + B_{n,l} + A_{n,l}\right) = n_u \left(B_{u,n} + A_{u,n}\right) + n_l B_{l,n}. \tag{206}$$

Converting densities n_i into departure coefficients, $n_i = b_i P_i^*$, we obtain

$$P_n^* b_n \left(B_{n,u} + B_{n,l} + A_{n,l}\right) = P_u^* b_u \left(B_{u,n} + A_{u,n}\right) + P_l^* b_l B_{l,n} \quad . \tag{207}$$

Gathering LTE densities we find

$$b_n \left(B_{n,u} + B_{n,l} + A_{n,l}\right) = \frac{P_u^*}{P_n^*} b_u \left(B_{u,n} + A_{u,n}\right) + \frac{P_l^*}{P_n^*} b_l B_{l,n} \quad . \tag{208}$$

Writing $B_{ln} = B_{nl}\, g_n / g_l$, we obtain the final form

$$b_n \left(\frac{g_u}{g_n} B_{u,n} + B_{n,l} + A_{n,l}\right) = \frac{P_u^*}{P_n^*} b_u \left(B_{u,n} + A_{u,n}\right) + \frac{P_l^*}{P_n^*} b_l \frac{g_n}{g_l} B_{n,l}. \tag{209}$$

5.7.3 Final radiative equations

The full set of radiative balance equations can be written as

$$\begin{aligned} \frac{db_n}{dt} = & \sum_l \frac{P_l^*}{P_n^*} b_l A_{n,l} \frac{g_n}{g_l} \eta_{n,l} \gamma_{n,l} + \sum_u \frac{P_u^*}{P_n^*} b_u \left(A_{u,n} P_{u,n} + A_{u,n} \eta_{u,n} \gamma_{u,n}\right) + \\ & \left[\alpha(rad) + \alpha(ind)\right] / P_n^* - \\ & b_n \left(\sum_l \left(A_{n,l} P_{n,l} + A_{n,l} \eta_{n,l} \gamma_{n,l}\right) + \sum_u A_{u,n} \frac{g_u}{g_n} \eta_{u,n} \gamma_{u,n} + \Gamma_n \right) \end{aligned} \tag{210}$$

where the continuum occupation number in the transition *ij* is given by

$$\eta_{i,j} \equiv J_\nu(i,j) / \left(2h\nu_{ij}^3 / c^2\right) = \left(\exp(h\nu / kT_{ex}) - 1\right)^{-1} \quad . \tag{211}$$

Here $J_\nu(ij)$ is the mean intensity of the net continuum at the line frequency, and T_{ex} is the excitation temperature of the continuum at the level frequency.

Figure 5 shows a test case that, in contrast to that shown in Figure 4, is dominated by radiative transitions.

Again, the full set of equations coupling the levels are solved, but spontaneous and induced processes are more important than collisions for many values of the radiation density. The model is of a very thin cell of gas, so that all lines and continua are optically thin, has a density of $n(H) = 10^{10}$ cm^{-3}, and an electron temperature of 5×10^4 K. The gas is exposed to a black body continuum with a color temperature of $T_{color} = 5 \times 10^4$ K, but the intensity of this continuum is varied. This intensity is parameterized by an energy density temperature defined by $T_u \equiv (u/a)^{1/4}$ where u and a are, respectively, the actual radiation energy density and Stefan's radiation density constant.

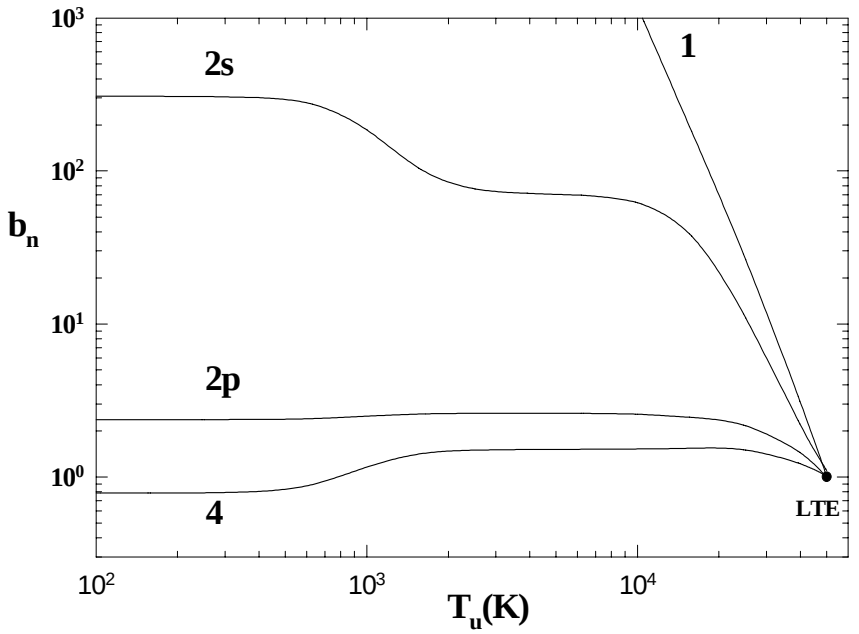

Figure 5 The calculations are for a constant temperature ($T = 5 \times 10^4$ K) optically thin gas exposed to black body radiation with a color temperature of $T_{color} = 5 \times 10^4$ K, but with various values of the energy density, parameterized as $T_u = (u/a)^{1/4}$, where u is the actual radiation density. hbnvsu

A radiation field given by Planck's law (i.e., $T_u \equiv T_{color}$) forces the ionization and level population of an atom or ion to LTE in much the same way that high electron densities do. As Figure 5 shows, at very low values of T_u (low photon densities) the ground and $n = 2$ states are overpopulated for much the same reason that this occurs at low electron densities; the downward spontaneous radiative rates are fast relative to the induced (upward and downward) rates. At very low T_u (< 500 K), $n \geq 3$ levels are under populated since they decay at a rate much faster than the induced rates (for $T = 5 \times 10^4$ K these levels have $h\nu \ll kT$, so induced processes will be fast relative to spontaneous rates when $T_u = T_{color}$ and the atom is in LTE). As T_u increases, fluorescence from the ground state over-populates excited states (because the ground state is itself overpopulated) and b_4 exceeds unity. Finally, in the limit where $T_u = T_{color}$, the departure coefficients reach unity and the atom goes to LTE. (The actual mean departure coefficient for the entire atom is $\overline{b_i} = 1.013 \pm 0.029$). Note that the vast majority of the neutral hydrogen population is in excited states when the atom approaches LTE at these temperatures.

The hydrogen density ($n(H) = 10^{10}$ cm^{-3}) is low enough for radiation to be the main agent affecting level populations for most values of T_u. Fluorescence from the

ground state drives the population of n=4 above its LTE value for many radiation densities. Induced processes, mainly transitions between adjacent levels, drive the atom to LTE when T_u reaches 5×10^4 K.

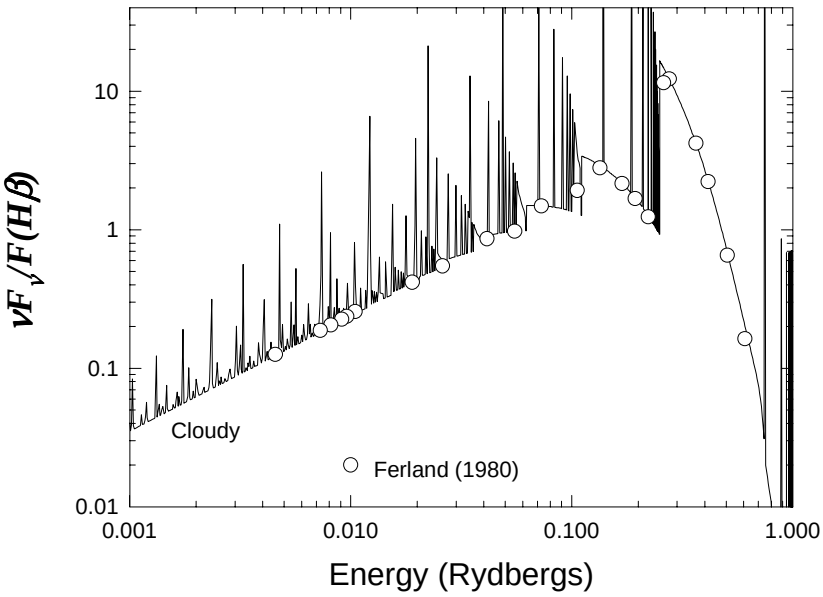

Figure 6 The emission from a slab of gas is compared with the predictions of Ferland (1980). hemis

5.8 Continuous Thermal Emission

Diffuse emission (free-free and free-bound) by the model hydrogen atom is computed using the stored photoabsorption cross sections and detailed balance (i.e., the Milne relation; see Mihalas 1978).

Free-bound continua of all levels of hydrogen and helium are treated as follows. The Milne relation for the emissivity $4\pi j$ (erg cm^3 Hz^{-1} s^{-1}) can be expressed as (Brown and Mathews 1970)

$$4\pi j_\nu = h\nu \left(\frac{2\pi m_e k}{h^2} \right)^{-3/2} \frac{8\pi}{c^2} \frac{g_n}{g_e g_{ion}} T^{-3/2} \nu^2 \alpha_\nu(n) \exp\left(-h(\nu - \nu_o)/kT\right) \qquad (212)$$

where the statistical weight of level n is $g_n = 2n^2$ for H^0 and He^+, and $g_n = n^2$ for helium singlets.

The code actually works with units similar to photons Ryd^{-1} s^{-1} cm^{-2}. The photon emissivity (photons cm^3 s^{-1} Ryd^{-1}) is then

$$\begin{aligned} \varphi_\nu(T,n) &= \left(\frac{2\pi m_e k}{h^2} \right)^{-3/2} \frac{8\pi}{c^2} \frac{g_n}{g_e g_{ion}} T^{-3/2} \nu^2 \alpha_\nu(n) \exp\left(-h(\nu - \nu_o)/kT\right) \\ &= 4.12373 \times 10^{11} \frac{g_n}{g_e g_{ion}} T^{-3/2} \nu_{Ryd}^{\ 2} \alpha_\nu(n) \exp\left(-h(\nu - \nu_o)/kT\right) \end{aligned} \qquad (213)$$

where the g's are the statistical weights of the constituents, ν_{Ryd} is the photon energy in Rydbergs, $h\nu_o \sim z^2/n^2$ is the ionization potential in Rydbergs, $\alpha_\nu(n)$ is the photoionization cross section, and the other symbols have their usual meanings. Equation 213 is evaluated directly using the stored photoionization cross sections. A similar approach is used for other absorption opacities, such as brems and H^-. Detailed balancing between absorption and emission mechanisms is necessary if LTE is to be achieved.

A test case with an ionized hydrogen plasma at a temperature of 10^4 K and a density of 10^7 cm^{-3} (to suppress two photon emission) was computed, and is shown in Figure 6.

The input stream used to derive the figure is given as **hemis.in** in the test suite. As can be seen from the figure, the predicted diffuse continuum is generally within 10 percent of the exact value (Ferland 1980).

Figure 7 shows another series of test cases in which a very high density gas with cosmic abundances is irradiated with a 50,000 K blackbody radiation field in strict thermodynamic equilibrium. As can be seen from the figure, the predicted continuum goes to the blackbody limit.

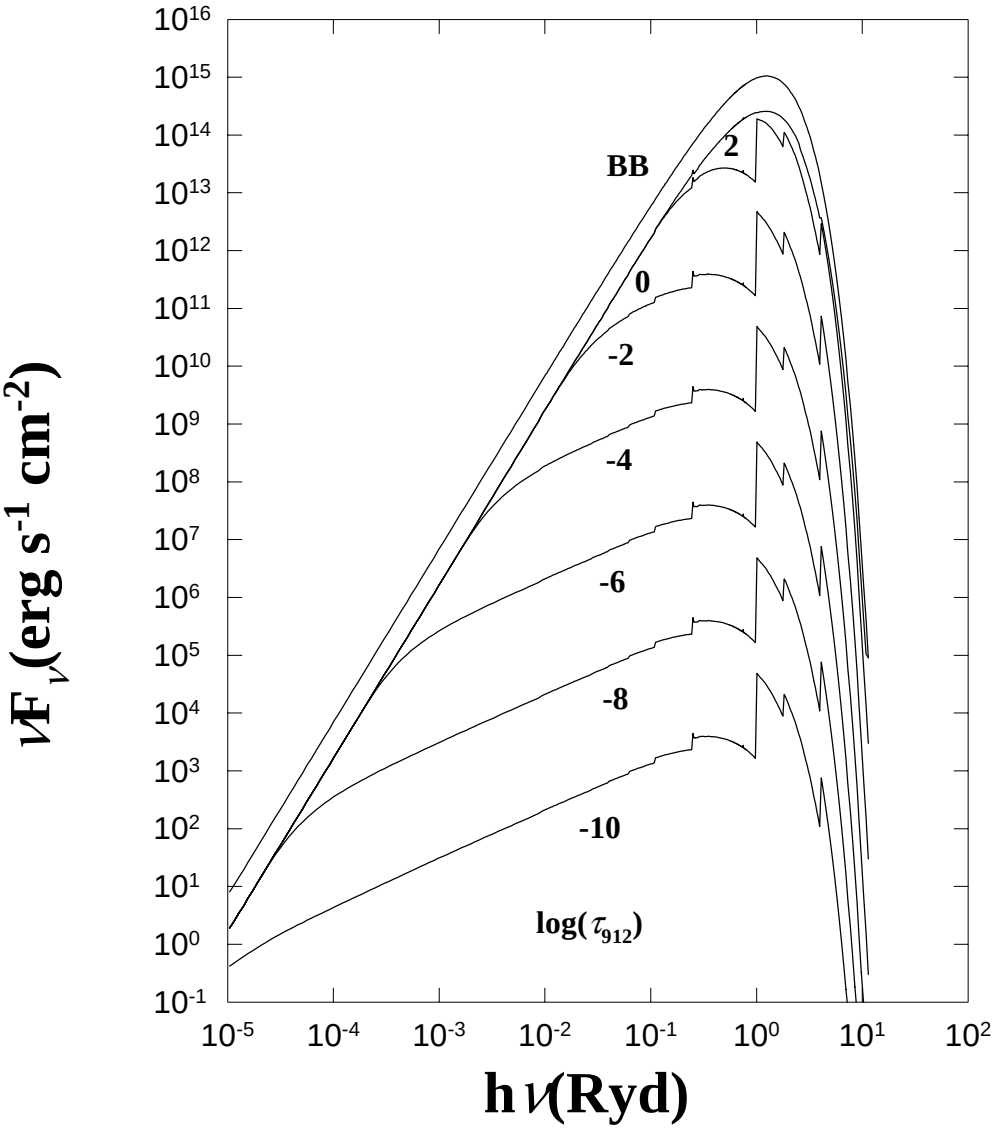

Figure 7 The emission from a dense slab of gas with cosmic abundances is shown as a function of the optical depth at the Lyman limit. The log of this optical depth is indicated on the figure. The top curve is for emission given by Planck's law. The continuous emission goes to the blackbody limit in the case of large continuum optical depths. conlte

6 H^- AND MOLECULES

6.1 Overview

An ion-molecule network, initially based on Black (1978) but heavily revised to include the network described by Hollenbach and McKee (1979; 1989), is included in Cloudy. The network presently includes H^-, H_2, H_2^+, H_3^+, HeH^+, OH, OH^+, CH, CH^+, O_2, O_2^+, CO, CO^+, H_2O, H_2O^+, H_3O^+, and CH_2^+.

The treatment of the major hydrogen molecules (i.e., H_2, H_2^+, H_3^+ and H^-) is discussed in the first subsection, and is based on Lambert and Pagel (1968); Black (1978); Lites and Mihalas (1984); Hollenbach and McKee (1979; 1989; hereafter HM79 and HM89); Tielens and Hollenbach (1985a, b; hereafter TH85), Lenzuni, Chernoff, and Salpeter (1991; hereafter LCS91), and Wolfire, Tielens, and Hollenbach (1990); Crosas and Weisheit (1993); and Puy et al (1993). This section is adapted from Ferland and Persson (1989) and Ferland, Fabian, and Johnstone (1994).

6.2 The Saha Equation for Arbitrary Systems

The Boltzmann equation relates the densities of related species by the expression

$$\frac{n_{final}}{n_{initial}} = \frac{\rho_{final}}{\rho_{initial}} \exp\left(-\Delta E / kT\right) \qquad (214)$$

where $n_{initial}$ and n_{final} indicate the densities of the initial and final states, and the ρ's are the densities of available states at a given energy. Consider the process $i \Rightarrow j+k$. The energy change during this process is

$$\Delta E = \chi_I + \frac{1}{2} m v^2 \qquad (215)$$

where the first term is the ionization or dissociation potential of the initial system, and the second term represents the kinetic energy of the system in the final state. The sign of ΔE is related to the energies of the initial and final systems by

$$E_{final} = E_{initial} + \Delta E \quad . \qquad (216)$$

The ρ's entering equation 214 are the total densities of states accessible at an energy E. Since the initial state is a bound particle we can take it as at rest in the lab frame, and consider the final state consisting of two constituent particles moving with kinetic energy ΔE. The density of states of the final particles can be written as the product of densities of states due to electron spin and to motion of the particle. Nuclear spins are assumed to be uncorrelated, so nuclear statistical weights cancel out and are not carried through.

Considering only spin and motion (momentum) the total density of states is the spin statistical weight of the particle g_{spin} multiplied by the density of states due to momentum g_p (Mihalas 1978, p 112; Elitzur 1992, p 14):

$$\rho_{total} = g_{spin} g_p \qquad (217)$$

where g_p is

$$g_p = \frac{dx\,dy\,dz\,dp_x\,dp_y\,dp_z}{h^3} \quad . \tag{218}$$

The volume element can be removed from the problem by defining it as the volume containing one particle,

$$dx\,dy\,dz = \left(n_k \,/\, g_k\right)^{-1} \tag{219}$$

while the momentum volume element is given in terms of the particle's speed v by

$$dp_x\,dp_y\,dp_z = 4\pi p^2\,dp = 4\pi\, m^3 v^2\,dv \quad . \tag{220}$$

Combining these with equation 214 we find

$$\frac{n_{final} n_k}{n_{initial}} = \frac{n_j n_k}{n_i} = \left(\frac{g_{spin,j} g_{spin,k}}{g_{spin,i}}\right)\left(\frac{g_{p,j} g_{p,k}}{g_{p,i}}\right)\exp\left(-\Delta E / kT\right). \tag{221}$$

Shortening $g_{spin,x}$ to simply g_x, and using equation 220, we find

$$\frac{n_j n_k}{n_i} = \left(\frac{g_j g_k}{g_i}\right)\left(\frac{4\pi}{h^3}\frac{m_j^3 v_j^2 \exp\left(-\frac{1}{2} m_j v_j^2 \,/\, kT\right)dv_j\; m_k^3 v_k^2 \exp\left(-\frac{1}{2} m_k v_k^2 \,/\, kT\right)dv_k}{m_i^3 v_i^2 \exp\left(-\frac{1}{2} m_i v_i^2 \,/\, kT\right)dv_i}\right)\exp\left(-\chi / kT\right) \tag{222}$$

Integrating each energy term over velocity, making the substitution

$$x \equiv \left(\frac{m}{2kT}\right)^{1/2} v \quad , \tag{223}$$

we find

$$\int_0^\infty v_j^2 \exp\left(-\tfrac{1}{2} m_j v_j^2 \,/\, kT\right)dv_j = \left(\frac{2kT}{m_j}\right)^{3/2}\int_0^\infty \exp\left(-x^2\right)x^2\,dx = \left(\frac{2kT}{m_j}\right)^{3/2}\frac{\pi^{1/2}}{4} \tag{224}$$

where the root π over 4 is the value of the integral. The final form of the Saha equation, for an arbitrary system, is:

$$\begin{aligned}\frac{n_j n_k}{n_i} &= \left(\frac{g_j g_k}{g_i}\right)\left(\frac{2\pi\, kT}{h^2}\frac{m_j m_k}{m_i}\right)^{3/2}\exp\left(-\chi / kT\right) \\ &= 8.7819\times 10^{55}\left(\frac{g_j g_k}{g_i}\right)\left(\frac{T m_j m_k}{m_i}\right)^{3/2}\exp\left(-\chi / kT\right)\end{aligned} \quad . \tag{225}$$

For the case of ionization producing an electron, the mass of the electron is neglected relative to the mass of the atom. If the atom and ion are *i* and *j*, then we have a mass ratio factor that is basically

$$\frac{m_j m_k}{m_i} = \frac{m_{ion} m_e}{m_{atom}} \approx m_e . \tag{226}$$

The most common final expression includes the assumption that m_i and m_k are nearly identical, and cancel out. In this case we obtain the form of the Saha equation most often encountered for hot gas, with the 2 being the spin statistical weight of the electron:

$$\frac{n_{ion}n_e}{n_{atom}} = \left(\frac{2g_j}{g_i}\right)\left(\frac{2\pi m_e kT}{h^2}\right)^{3/2} \exp\left(-\chi / kT\right). \tag{227}$$

In the case of molecular hydrogen

$$\frac{n_H n_H}{n_{H_2}} = 4\left(\frac{\pi kTm_p}{h^2}\right)^{3/2} \exp\left(-\chi / kT\right). \tag{228}$$

6.3 The Hydrogen Network

The main hydrogen network includes H^-, H_2, H_2^*, H_2^+, H_3^+, and HeH^+, and its solution is performed in subroutine ***hmole***.

The statistical weight of H_2^+ is 4 while that of H_2 is 1 and the dissociation energies are 2.647 eV and 4.477 eV respectively.

The set of balance equations for the first three species is solved simultaneously, using the matrix:

$$\begin{pmatrix} H \text{ conservation} \\ H^- \text{ balance} \\ H_2 \text{ balance} \\ H_2^+ \text{ balance} \\ H_3^+ \text{ balance} \end{pmatrix} \begin{pmatrix} n(H^o) \\ n(H^-) \\ n(H_2) \\ n(H_2^+) \\ n(H_3^+) \end{pmatrix} = \begin{pmatrix} n(H^o) \\ 0 \\ 0 \\ 0 \\ 0 \end{pmatrix} . \tag{229}$$

In the balance equations the process that destroy species x are entered as c[x][x], (these are negative), while those which create x from y are entered as c[x][y].

6.4 LTE Populations of Hydrogen Molecules

In much of the following discussion comparison and relationships will be made between the predicted hydrogen species populations and their LTE values.

The LTE relative population density of H^- is

$$P^*\left(H^-\right) = \frac{n^*\left(H^-\right)}{n_e n\left(H^o\right)} = \frac{g_{H^-}}{g_{H^o}g_e}\left(\frac{h^2}{2\pi m_e kT}\right)^{3/2} \exp\left(I(H^-)/kT\right) \quad \left(\text{cm}^3\right) \tag{230}$$

where g_i is the statistical weight of the constituents, ($g_{H^-} = 1$; $g_{H^o} = 2$; and $g_e = 2$), the binding energy of the negative hydrogen ion is *I(H-)* = 0.055502 Ryd, and other constants have their usual meaning. This population ratio is computed in routine ***hmole*** and assigned the variable name *phmlte*.

The LTE relative population density of H_2 is

$$P^*\left(H_2\right) = \frac{n^*\left(H_2\right)}{n\left(H^o\right)n\left(H^o\right)} = \frac{g_{H_2}}{g_{H^o}g_{H^o}}\left(\frac{h^2}{\pi m_p kT}\right)^{3/2} \exp\left(I(H^-)/kT\right) \quad \left(\text{cm}^3\right) \tag{231}$$

This is referred to as *ph2lte*. The LTE population of H_2^+ is computed similarly, and referred to as *phplte*.

6.5 The H$^-$ Balance; Radiative Processes

Although only a trace amount of hydrogen is in the form of H$^-$, the opacity provided by this ion is often dominant in the optical and near infrared, and helps couple energy in the near infrared continuum to moderately ionized gas. The methods and approximations employed to include heating and cooling by H$^-$ are described here. Other discussions can be found in Lambert and Pagel (1968), Vernazza, Avrett, and Loeser (1981), and Lites and Mihalas (1984). This section is based on Ferland and Persson (1989).

The equilibrium density of H$^-$ is determined by assuming statistical equilibrium, and balancing production and destruction mechanisms. Great care is taken in including both forward and back reactions, to ensure that the present treatment of H$^-$ is capable of going to LTE in the limit of high radiation or particle densities.

6.5.1 Radiative attachment

This is the most important creation mechanism for H$^-$ at low densities, when three-body processes are negligible;

$$H^o + e^- \Rightarrow H^- + \gamma \quad . \tag{232}$$

For temperatures greater than 10^4 K the rate coefficient is evaluated by numerically integrating the photodetachment cross section over frequency;

$$\alpha_{rad}(T) = P^*\left(H^-\right)\int_{\nu_o}^{\infty}\alpha_\nu \frac{8\pi\nu^2}{c^2}\exp\left(-h\nu / kT\right)d\nu \quad \left(\mathrm{cm^3\ s^{-1}}\right) \tag{233}$$

where cross sections computed by Wishart (1979) and spline interpolation are used. These cross sections are in excellent agreement with the velocity operator bound-free cross sections tabulated by Doughty et al. (1966). The energy interval between the photodetachment threshold at 0.055502 Ryd and ~1.8 Ryd is divided into roughly 100 cells with logarithmically increasing width, and the integration is carried out as a straight forward sum.

This method is not numerically expedient for very low temperatures, where the energy bandwidth of the integral is small, and a much finer frequency grid would be required. Rather, the integration was carried out using spline interpolation and 32 point gaussian quadrature, integrating over factors of two in $h\nu/kT$. The results were then fitted with a set of power-laws. The rate coefficients (cm^{-3} s^{-1}) can be approximated by:

$$\alpha(T_e) = \begin{cases} 8.934\times10^{-18}T^{0.505} & 1K \le T < 31.62 \ \ \mathrm{K} \\ 5.159\times10^{-18}T^{0.664} & 31.62K \le T < 90 \ \ \mathrm{K} \\ 2.042\times10^{-18}T^{0.870} & 90K \le T < 1200 \ \ \mathrm{K} \\ 8.861\times10^{-18}T^{0.663} & 1200K \le T < 3800 \ \ \mathrm{K} \\ 8.204\times10^{-17}T^{0.393} & 3800K \le T \le 10^4 \ \ \mathrm{K} \end{cases} \tag{234}$$

These approximations fit the exact numerical results with a mean deviation of 0.7 percent, and the largest error of 2.05 percent, over the indicated temperature range.

Tests show that the numerical radiative attachment rates computed here are in very good agreement with the approximation given by Hutchings (1976), who used

the cross sections computed by Doughty et al. (1966), for temperatures 500 K ≤ T ≤ 2500 K. (Notice that there is a typographical error in the approximation for the radiative attachment rate given by Palla, Salpeter, and Stahler 1983.) It is also within 10% of the value given by Dalgarno and Kingston (1963), which was based on earlier calculations of the photodetachment cross section.

Continuum occupation numbers can be large in the infrared. The induced radiative attachment rate coefficient is

$$\alpha_{ind}(T) = P^*(H^-) \int_{\nu_o}^{\infty} \alpha_\nu \frac{4\pi J_\nu(\tau)}{h\nu} \exp\left(-h\nu / kT\right) d\nu \quad \left(\mathrm{cm}^3\ \mathrm{s}^{-1}\right) \tag{235}$$

where the mean intensity of the depth-dependent continuum is $J_\nu(\tau)$. This expression is used for all temperatures.

6.5.2 Photodetachment

Photodetachment,

$$H^- + \gamma \Rightarrow H^o + e^- \tag{236}$$

is the dominant H- destruction mechanism for many conditions. The rate is evaluated in the standard manner;

$$\Gamma\left(H^-\right) = \int_{\nu_o}^{\infty} \alpha_\nu\left(bf\right) \frac{4\pi J_\nu(\tau)}{h\nu} d\nu \quad \left(\mathrm{s}^{-1}\right) \quad . \tag{237}$$

The integral is evaluated as a sum over the numerically binned continuum. The incident continuum is then attenuated by optical depth increments

$$d\tau(H^-) = \alpha_\nu(bf)\, n(H^-)\left\{1 - \exp\left(-h\nu / kT\right) / b_{H^-}\right\} f(r)\, dr \tag{238}$$

where b_{H^-} is the departure coefficient for H-, $b_{H^-} \equiv n(H^-)/n^*(H^-)$, $f(r)$ is the filling factor, and $n^*(H^-)$ is the LTE H- density.

6.5.3 Photodetachment by hard photons

The H- photoabsorption cross section increases above ~ 3/4 Ryd, energies where excitation of n ≥ 2 levels is possible. Cross sections that include this process are taken from Broad and Reinhardt (1976). These calculations do not extend to high energies, so I scaled high-energy hydrogen cross sections by the ratio of H- to Hº cross sections at 18Å in order to take absorption of x- and γ- rays into account.

The cross section for (γ,2e-) absorption is much smaller than (γ, e-) (Broad and Reinhardt 1976), and this latter process is neglected.

6.5.4 The approach to LTE; high radiation densities

As a test of the assumptions and methods, the approach to LTE under conditions determined by radiative attachment (spontaneous and induced) and photodetachment are first considered. Tests in which gas with temperature T is exposed to black body radiation fields with color temperature T_{color} are computed. The color and gas temperatures are set equal, $T = T_{color}$, and the intensity of the radiation field is varied up to the black body limit. The intensity of the radiation field is parameterized by the equivalent energy density temperature $T_u = (u/a)^{1/4}$, where u is the energy density (erg cm^{-3}; see above) and a is the Stefan's radiation density constant. The equilibrium population of H$^-$ was computed, including all process mentioned below, but with the hydrogen density small enough (typically ~ 10^5 cm^{-3}) for radiative processes to be most important. The H$^-$ population is expressed as a departure coefficient, and the results are shown in Figure 8, for tests in which T_{color} = 0.5, 1, and 2×10^4 K.

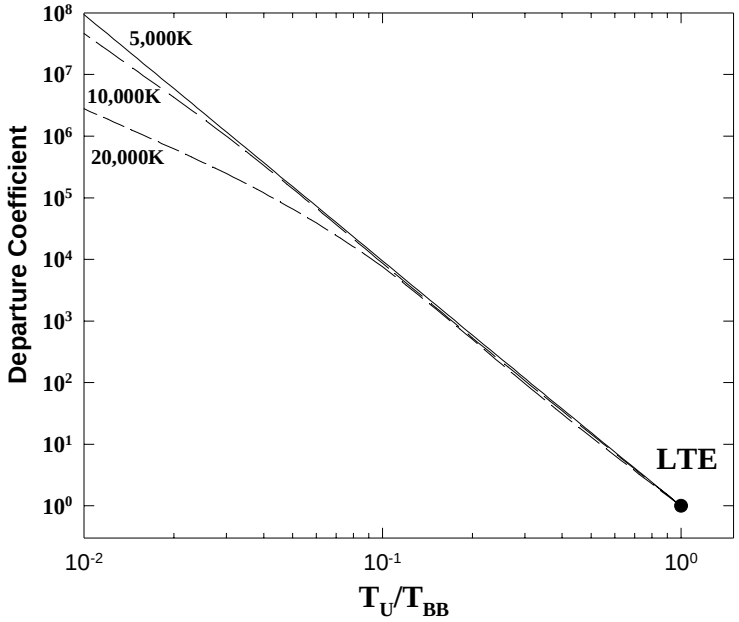

Figure 8 Departure coefficients for H$^-$. The figure shows tests in which the hydrogen density was held fixed at a low and the gas irradiated by black bodies with color temperatures of 5, 10, and 20 $\times$ 10^3K. Gas temperature and color temperatures were equal. The energy density temperature T_u. was varied up to its LTE limit. The H$^-$ departure coefficient is within 0.2% of unity when $T_u = T_{color}$. hmivsu

When $T_u = T_{color}$, and the radiation field is in strict thermodynamic equilibrium, radiative processes must hold H$^-$ in LTE and departure coefficients of unity are expected. The computed departure coefficients for the three temperatures are 0.9998, 0.9996, and 1.0030, respectively. As the Figure shows, when T_u is lowered below T_{color}, the intensity of the radiation field falls below its thermodynamic equilibrium value, and the population of H$^-$ increases. This is because the photodetachment rate (which is proportional to the intensity of the radiation field) is no longer in balance with the radiative attachment rate (which is proportional only to the electron density).

6.6 The H^- Balance; Collisional Processes

6.6.1 Associative detachment

The most important H_2 formation mechanism in grain-free environments, and a significant H^- destruction mechanism, is associative detachment,

$$H^- + H^o \Leftrightarrow H_2 + e^- \tag{239}$$

where rate coefficients from Bieniek and Dalgarno (1979) are used. The reverse reaction rate coefficient C_R, for electron collisional dissociation of H_2, is related to the forward rate coefficient C_F by detailed balance;

$$C_R = C_F \frac{P^*(H^-)}{P^*(H_2)} \quad . \tag{240}$$

6.6.2 Electron collisional detachment

For nebular temperatures (~10^4 K) and moderate levels of ionization, the process

$$H^- + e^- \Leftrightarrow H + 2e^- \tag{241}$$

is a competitive H^- destruction mechanism. Rates taken from the compendium of Janev et al. (1987) are used. The reverse process, electron three-body recombination with neutral hydrogen, is included via detailed balance;

$$C_R = C_F \, P^*(H^-) \quad . \tag{242}$$

6.6.3 Collisional ionization by suprathermal electrons

The total suprathermal collisional ionization rate is computed using approximations from Shull and Van Steenberg (1985). Ionization of H^- by suprathermal electrons is scaled from the H^o rates using cross sections at 20 eV given by Janev et al. (1987). This energy was chosen as representative of the mean energy of the secondary electron shower. The majority of these collisions are of the form $e^- + H^- \rightarrow H(1s) + 2e^-$, although $e^- + H^- \rightarrow H^+ + 3e^-$ collisions occur roughly 1% of the time.

6.6.4 Mutual neutralization

Neutral hydrogen can charge transfer with the negative ion through

$$H^- + H^+ \Leftrightarrow H + H^* \quad . \tag{243}$$

The rate coefficients given in Janev et al. (1987) are used. By far the largest rate coefficients are for collisions that populate hydrogen in the n=3 level. These rates are based on both experimental and theoretical data (see, for example, Peart et al. 1985).

The reverse reaction is included using detailed balance. If the rate coefficient for the forward reaction is C_F then the reverse reaction rate, and its rate coefficient C_R, are given by

$$H_{1s} \, n_i \, C_R = b_i \, P^*(H^-) \, n_e n_p \, C_F \tag{244}$$

where n_i and b_i are the population and departure coefficient of hydrogen in the i^{th} level.

6.6.5 Charge neutralization with heavy elements

The process

$$H^- + A^+ \Leftrightarrow H^o + A^o \qquad (245)$$

is considered by Dalgarno and McCray (1973), who give rate coefficients for very low temperatures and ionization levels. Judging from the curves given by Peterson et al. (1971), upon which the Dalgarno and McCray rates are based, the approximation they give should still be valid (although very uncertain) at temperatures of general interest ($\sim 0.5 - 1.0 \times 10^4$ K). Here A^+ is all singly ionized species, which are assumed to be neutralized at the same rate.

6.6.6 Neglected processes

Collisional detachment by protons ($p^+ + H^- \rightarrow H + p^+ + e^-$), which has a negligible rate coefficient according to Janev et al. (1987), is neglected, as is collisional detachment by atomic hydrogen ($H^- + H \rightarrow 2H + e^-$), which has no reliable rate coefficient according to Lites and Mihalas (1984).

6.6.7 The approach to LTE; high hydrogen densities

A series of models in collisional equilibrium was computed. Radiative processes were also included, but the incident radiation field, a 10^4 K blackbody, was given a negligible intensity (an ionization parameter of 10^{-12}). Three temperatures, 0.5, 1, and 2×10^4 K, were considered to span the temperature range typical of regions with significant H^- population. The hydrogen density was varied between 10^8 and 10^{18} cm^{-3} to confirm the approach to LTE at high densities. The results of these calculations are shown in Figure 9.

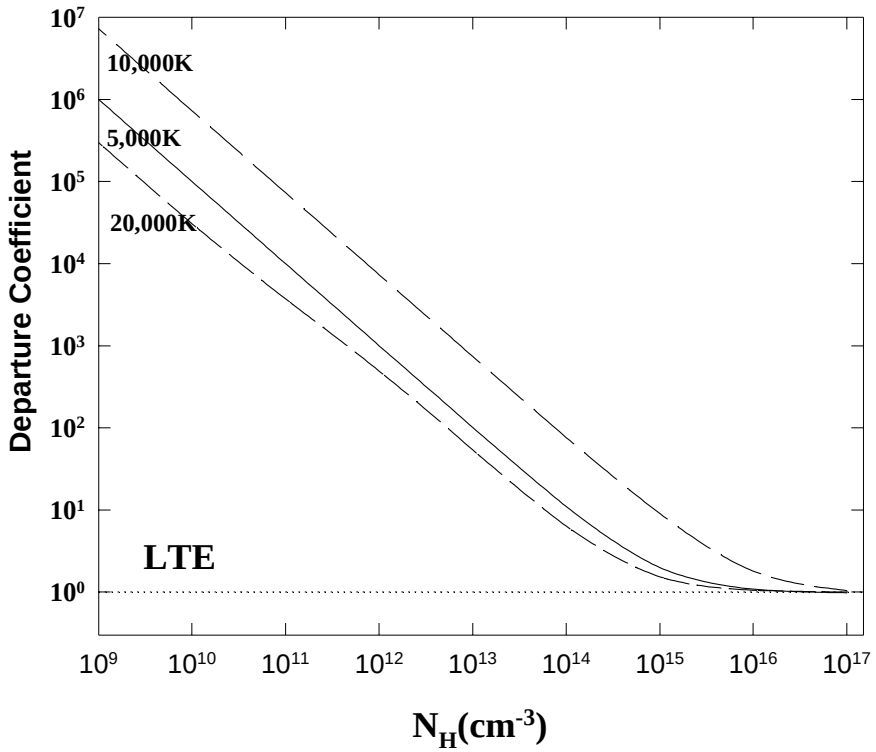

Figure 9 Departure coefficients for H^- are shown. The radiation density was low and the total hydrogen density varied. Three gas temperatures are shown. Collisions bring H^- to LTE at high densities. hmivsn

For the majority of the calculations hydrogen is largely neutral, and for the smaller temperatures a significant fraction of the hydrogen was in the molecular form (H_2 and H_2^+). The calculation confirms that the departure coefficients are within 2% of unity at the highest densities computed.

6.7 The HeH^+ Molecular Ion

Rates for radiative association of He and H^+ to form HeH+ are taken from Zygelman and Dalgarno (1990).

6.8 The H_2 Molecule

The hydrogen chemistry network includes the ion-molecules H_2, H^-, H_2^+, and H_3^+. All of the chemical reactions involving H_2 described by HM79, TH85, HM89, and LCS91 have been incorporated in the present treatment. Rather than go into these details, which are well presented in these papers, we only outline details of how some of the processes have been implemented.

6.8.1 Associative detachment of H^-

The process

$$H^- + H \Rightarrow H_2 + e \tag{246}$$

is the main H_2 formation mechanism in low-density grain-free regions, and is treated as described above. At temperatures of interest here (~10^3 K) the rate for H_2 formation by this process is set by the rate for radiative association to form H^-, and is of order 10^{-15} cm^3 s^{-1} (see above).

6.8.2 Catalysis on grain surfaces

The process

$$2H + \text{grain} \Rightarrow H_2 + \text{grain} \tag{247}$$

is a competitive H_2 formation process when grains are present. The rate coefficient is taken from Hollenbach and McKee (1979). Defining the fraction of atoms which form molecules as

$$f_a = \left(1 + 10^4 \exp\left(-600 / T_{gr}\right)\right)^{-1} \tag{248}$$

then the rate coefficient is given by

$$\alpha_{gr}\left(H_2\right) = 3\times10^{-18} \frac{\sqrt{T}\, A_{gr}\, f_a}{1 + 0.04\sqrt{T_{gr} + T} + 0.002T + 8\times10^{-6}T^2} \tag{249}$$

where A_{gr} is the grain abundance relative to the ISM value, and T and T_{gr} are the electron and grain temperatures respectively. The grain temperature is determined self-consistently, including radiative and collisional heating and cooling, as described in the section "Grain Physics" beginning on page 288 below.

At T=10^3 K and T_{gr}=100 K (representative values of the gas and grain temperature in regions near a H^o-H_2 interface) the rate coefficient for grain catalysis is ~4×10^{-18} cm^{-3} s^{-1}. For most conditions of interest here radiative association is at least a competitive H_2 formation mechanism. The ratio of the two processes (referred to as the H^- and grain H_2 formation routes) is then

$$\frac{r\left(H^-\right)}{r\left(\text{grain}\right)} = \frac{n_e \alpha\left(H^-\right)}{n_H \alpha\left(\text{grain}\right)} \approx \frac{n_e}{n_H} 250 \tag{250}$$

i.e., the H^- route is faster for conditions of moderate ionization ($n_e/n_H > 4\times10^{-3}$) even when grains are present. When grains are absent (or deficient) the H^- route dominates.

6.8.3 Excited atom radiative association

Rates for the process

$$H(n=2)+H(n=1) \Rightarrow H_2 + h\nu \tag{251}$$

are taken from Latter and Black (1991).

6.8.4 Excited molecular dissociation

Rates for the process

$$H_2(v \geq 4)+e^- \Rightarrow \left(H_2^-\right)^* \Rightarrow H + H^- \tag{252}$$

are given in Janev et al. (1987; their process 2.2.17), and these have been adopted by Lenzuni et al. (1991) and Crosas and Weisheit (1993) in their work on high density gas. Tests show that this process, if taken at face value, is by far the fastest destruction mechanism for molecular hydrogen under ISM conditions.

The process outlined by Janev et al. (1987) involves an electron capture by H_2 into vibrationally excited levels ($4 \leq v \leq 9$). The process is fast at low temperatures because the energy barrier is small, and the excited levels have large populations at laboratory densities. The process proceeds much more slowly at ISM densities, however, because excited levels have populations below their LTE value. This situation is thus similar to that described by Dalgarno and Roberge (1979). We have modified the Janev et al. (1987) rates using the physics outlined by Dalgarno and Roberge.

6.8.5 Discrete absorption into Lyman and Werner bands

Line absorption and excitation leading to dissociation through the vibrational continuum,

$$H_2 + h\nu \Rightarrow H_2^* \Rightarrow 2H + h\nu \tag{253}$$

is the dominant H_2 destruction mechanism in regions where photodissociation (by photons with hν > 14.7 eV) and photo-ionization (with hν> 15.4 eV) do not occur (Stecher and Williams 1967).

Photodissociation through the Lyman-Werner bands occurs through a large number of transitions between 1109Å and the Lyman edge for a region shielded by atomic hydrogen (i.e., no radiation shortward of 912Å). Individual H_2 electronic transitions become optically thick for sufficient column densities, and eventually the H_2 becomes self-shielding. H_2 then becomes the dominant hydrogen species.

Photodissociation through the Lyman-Werner bands is included using the approximations outlined by TH85. The incident radiation field is taken as the mean over the energy interval 1109Å–912Å , (appropriate for photo-excitation into the $B^1\Sigma_u^+$ electronic state). This quantity is then reposed in terms of the Habing (1968) radiation field, which is the quantity used by TH85. H_2 self-shielding is included using escape probabilities and the deduced optical depth, again using the approximations described by TH85.

6.8.6 Photo-ionization to H_2^+

Photons with energies greater than 15.4 eV produce H_2^+ via

$$H_2 + h\nu \Leftrightarrow H_2^+ + e^* \quad . \tag{254}$$

This process both creates H_2^+ and heats the gas. Photo-absorption cross sections are taken from the compendium of Janev et al. (1987).

6.8.7 Collisional dissociation by H^o, He^o, and e^-

The rate coefficient for the forward process, collisional dissociation by the species S (one of H^o, He^o, or e^-),

$$H_2 + S \Rightarrow 2H + S \tag{255}$$

is taken from Dove and Mandy (1986; dissociation by H^o), Dove et al. (1987; dissociation by He^o) and Janev et al. (1987; dissociation by electrons). These can be important destruction mechanisms only for warm regions of the ISM because of the large binding energy of H_2 (~50,000 K).

The reverse reactions are included via detailed balance. Three-body formation of H_2 is important only for very high densities ($n \gg 10^{10}$ cm^{-3}).

6.8.8 H_2 cooling

Cooling due to collisional excitation of vibration-rotation levels of H_2 is treated using the analytic fits given in Lepp and Shull (1983). Both H_2-H and H_2-H_2 collisions are included.

6.8.9 H_2 heating

Many electronic excitations eventually decay to excited vibration-rotation levels within the ground electronic state, and these can then heat by gas following collisionally de-excitation. The scheme outlined by TH85 is again used.

6.9 Heavy Element Molecules

The heavy element molecule network described by Hollenbach and McKee (1989) has been incorporated into Cloudy.

The system of equations which are solved are as follows:

$$\begin{pmatrix} C \text{ conservation} \\ O \text{ conservation} \\ CH \text{ balance} \\ CH^+ \text{ balance} \\ OH \text{ balance} \\ OH^+ \text{ balance} \\ CH_2^+ \text{ balance} \\ C^+ \text{ balance} \\ CO \text{ balance} \\ CO^+ \text{ balance} \\ H_2O \text{ balance} \\ H_2O^+ \text{ balance} \\ H_3O^+ \text{ balance} \\ O_2 \text{ balance} \\ O_2^+ \text{ balance} \end{pmatrix} \begin{pmatrix} C \\ O \\ CH \\ CH^+ \\ OH \\ OH^+ \\ CH_2^+ \\ C^+ \\ CO \\ CO^+ \\ H_2O \\ H_2O^+ \\ H_3O^+ \\ O_2 \\ O_2^+ \end{pmatrix} = \begin{pmatrix} C_{total} \\ O_{total} \\ 0 \\ 0 \\ 0 \\ 0 \\ 0 \\ 0 \\ 0 \\ 0 \\ 0 \\ 0 \\ 0 \\ 0 \\ 0 \end{pmatrix} . \quad (256)$$

The heavy element chemistry network includes the molecules CH, CH^+, OH, OH^+, CH_2^+, CO, CO^+, H_2O, H_2O^+, H_3O^+, O_2, and O_2^+. The heavy element network, the hydrogen network described above, and the hydrogen-helium ionization balance network, are solved self-consistently. Of the 12 molecules in the heavy element network only CO develops a significant population under most circumstances.

6.9.1 Collisional Processes

The collision network described by Hollenbach and McKee (1989) is included (the original implementation of the network was based entirely on this work). Their approximations for the temperature dependence of the rate coefficients are used.

Photodissociation by line absorption of CO was updated to the formalism given by Hollenbach, Takahashi, & Tielens, (1991; their equations 11 and 12), which was based on the work of van Dishoeck & Black (1988). Additionally the rate coefficients for the reaction network have been updated to the rates given in Hollenbach et al.

6.9.2 Photochemical processes and heating

Rates for photochemical reactions of the form hν + XY => X + Y are largely taken from the compendium of Roberge et al. (1991). These are posed in terms of the average interstellar radiation field. They have been incorporated by taking the depth-dependent continuum, renormalizing this to the average interstellar radiation field, and then using the coefficients given by Roberge et al.

An exception to this prescription is CO, which can become a major opacity source. Photodissociation is treated by numerically integrating over the continuum (with a thresh hold of 12.8 eV) using the photodissociation cross section given by HM79.

Photodissociation heats the gas if the internal energy of the daughters is small. The kinetic energy is taken to be $\langle h\nu - \mathrm{DE} \rangle$ where DE is the dissociation energy and the mean is over the portion of the Balmer continuum that is active. Again, an exception is CO (the most important since it is the only heavy molecule that becomes

optically thick), where the heating is evaluated by numerically integrating over the attenuated incident continuum.

6.9.3 Cooling

Cooling due to collisional excitation of vibration-rotation levels of CH, OH, and H_2O is treated using the scheme outlined by HM79. Of these CO is the most important. ^{12}CO and ^{13}CO are treated as multi-level rigid rotors, with the full spectrum predicted.

7 HELIUM ISO-SEQUENCE

7.1 Overview

The helium-like isoelectronic sequence is treated with a single unified approach. Figure 10 shows a partial Grotrian diagram for He-like ions.

Bound-bound collision data come from Bray et al. (2000).

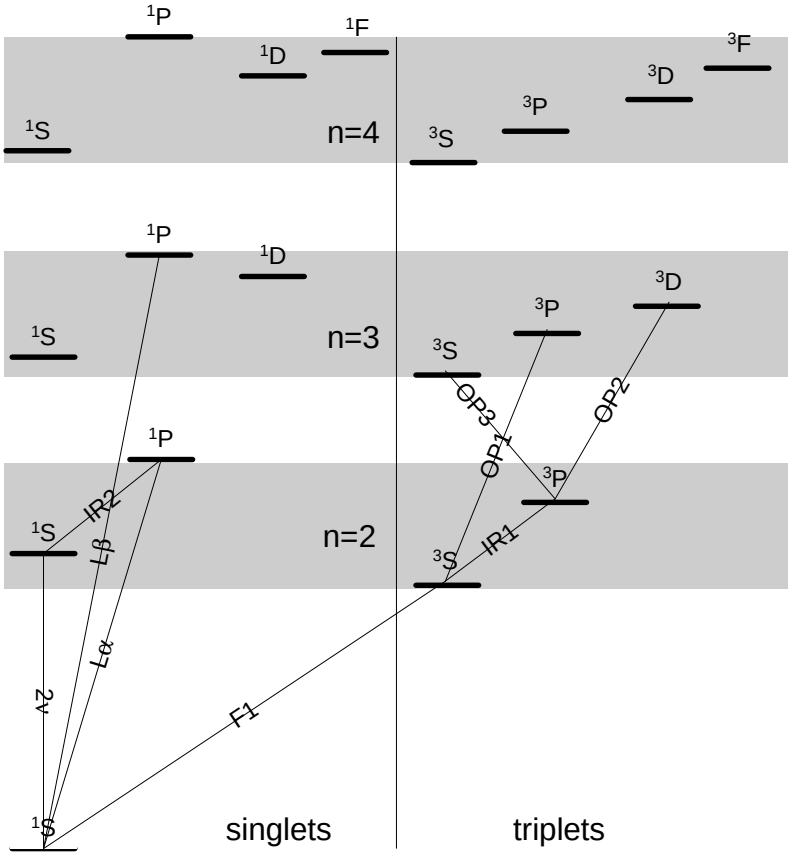

Figure 10 A partial Grotrian diagram for the helium iso-electronic sequence. helium

Table 21
Helium-like enery levels

index	desig	E(wn,He)	E(wn,O)	E(wn,Fe)
0	1 1S	0	0	0
1	2 3S	1.59867e+005	4.52637e+006	5.35554e+007
2	2 1S	1.66280e+005	4.58831e+006	5.38793e+007
3	2 3P	1.69076e+005	4.58550e+006	5.39002e+007
4	2 1P	1.71135e+005	4.62917e+006	5.40690e+007
5	3 3S	1.83243e+005	5.33976e+006	6.34332e+007
6	3 1S	1.84866e+005	5.35628e+006	6.35220e+007
7	3 3P	1.85562e+005	5.35599e+006	6.35302e+007
8	3 3D	1.86118e+005	5.36562e+006	6.35794e+007
9	3 1D	1.86118e+005	5.36562e+006	6.35794e+007
10	3 1P	1.86209e+005	5.36815e+006	6.35812e+007
11	4 3S	1.90301e+005	5.61633e+006	6.68519e+007
12	4 1S	1.90942e+005	5.62299e+006	6.68884e+007
13	4 3P	1.91216e+005	5.62297e+006	6.68922e+007
14	4 3D	1.91452e+005	5.62701e+006	6.69134e+007
15	4 1D	1.91452e+005	5.62701e+006	6.69134e+007
16	4 3F	1.91452e+005	5.62701e+006	6.69134e+007
17	4 1F	1.91452e+005	5.62701e+006	6.69134e+007
18	4 1P	1.91493e+005	5.62798e+006	6.69142e+007
19	5 3S	1.93348e+005	5.74265e+006	6.84256e+007
20	5 1S	1.93664e+005	5.74591e+006	6.84432e+007
21	5 3P	1.93800e+005	5.74592e+006	6.84452e+007
22	5 3D	1.93921e+005	5.74799e+006	6.84566e+007
23	5 1D	1.93921e+005	5.74799e+006	6.84566e+007
24	5 3F	1.93921e+005	5.74799e+006	6.84566e+007
25	5 1F	1.93921e+005	5.74799e+006	6.84566e+007
26	5 3G	1.93921e+005	5.74799e+006	6.84566e+007
27	5 1G	1.93921e+005	5.74799e+006	6.84566e+007
28	5 1P	1.93943e+005	5.74849e+006	6.84568e+007

7.2 The Helium Triplets

The population of the metastable 2^3S level is determined including all processes that create and destroy the level. Processes that destroy 2^3S include photoionization and collisional ionization, radiative decays to ground, and collisional transitions to the singlets. Processes that create populations include three-body and radiative recombination and collisions to the triplets from the singlets. Including only radiative recombination, exchange collisions to the singlets, and radiative decays to ground, the relative population of 2^3S can be written as

$$\frac{He(2^3S)}{He^+} = \frac{5.79\times10^{-6}\ t_4^{-1.18}}{1+3110\,t_4^{-0.51}n_e^{-1}} \qquad (257)$$

where t_4 is the electron temperature in units of 10^4 K.

7.3 Ionization Equilibria

The ionization equilibria of the various ions / atoms is accurate for all photon and electron densities. Tests presented in Part III of this document show that the balance goes to LTE in the high photon and electron density limits.

8 THE HEAVY ELEMENTS

8.1 Overview

The treatment of the ionization equilibrium of the elements heavier than helium is fairly conventional (see, for instance, Halpern and Grindlay 1980; Kallman and McCray 1982). This treatment is more approximate than that of the hydrogenic iso-sequence and helium at high densities (n_H » 10^{10} cm^{-3}) because the majority of ions are treated considering only the ground term and continuum for each ionization stage. In all cases, collisional ionization from ground (using data from Voronov 1997; and Xu and McCray 1991)) and a net three-body recombination coefficient (see, for example, Burgess and Summers 1976; the actual code is taken from Cota 1987) are included. Photoionization rates are modified for induced recombination as described by equation 205. All published charge transfer rate coefficients are also included (Kingdon and Ferland 1996). Inner shell photoionization is treated using Auger yields given by Kaastra and Mewe (1993). Photoionization cross sections are from Verner et al. (1996).

This treatment is approximate at high densities for two reasons. First, net radiative recombination coefficients, which have been summed over all levels (Aldrovandi and Pequignot 1972; Aldrovandi and Pequignot 1974; Gould 1978; Verner and Ferland 1996), are used. These sums are correct only in the low-density limit. At high densities levels can undergo collisional ionization before radiative decays to the ground state occur. A second problem is that substantial populations can build up in highly excited states when the density and temperature are high. When this occurs the partition function of the atom or ion is no longer equal to the statistical weight of the ground state. As a result the ionization equilibrium of the heavy elements is approximate for very high densities (n » 10^{10} cm^{-3}), with uncertainties increasing for higher densities. The statistical and thermal equilibrium of high-density gas is an area of on-going research.

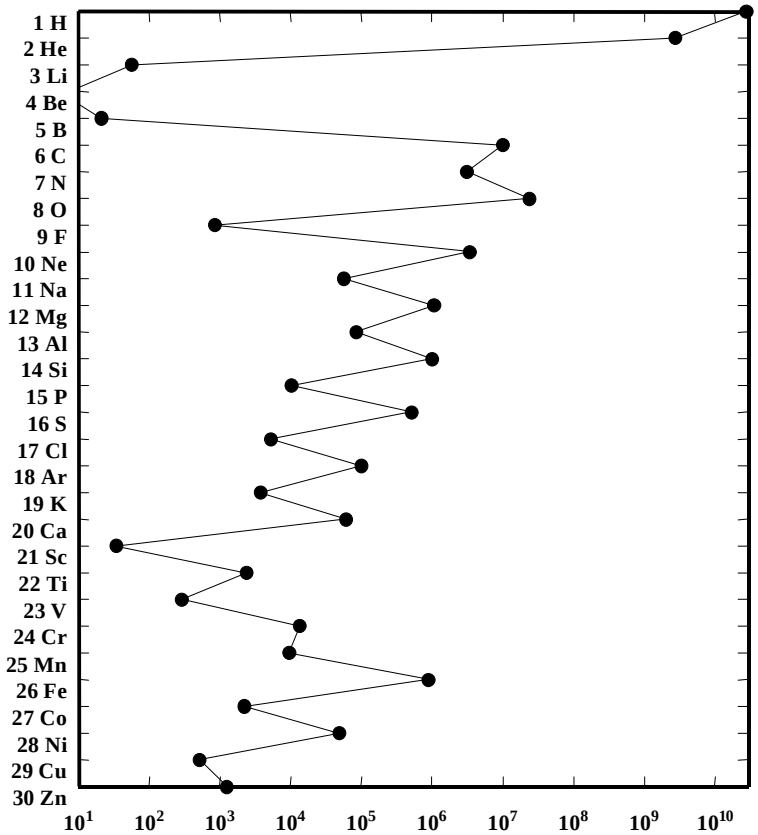

Figure 11 Solar system abundances are shown. ssystem

Many exotic line transfer effects can influence certain lines due to coincidental line overlap. A good general reference to a number of these processes

is the paper by Swings and Struve (1940). All of these processes are included in the line formation processes for those lines that are predicted by the code. Morton, York, and Jenkins (1988) and Verner, Verner, and Ferland (1996) provide a line lists for UV resonance lines, and Bowen's 1960 paper on forbidden lines remains a classic.

The effects of resonant structures often dominate collision strengths for infrared transitions. Oliva, Pasquali and Reconditi (1996) stress the uncertainties these may introduce.

8.2 Solar System Abundances

Figure 11 plots the solar system abundances of the elements, as tabulated by Anders and Grevesse (1989) and Grevesse and Noels (1993). The x-axis is the abundance by number relative to a scale where the abundance of silicon is 10^6. The y-axis lists the atomic number and the chemical symbol for the element.

8.3 Periodic Table

A periodic table of the first 36 elements follows.

1 H																	2 He
3 Li	4 Be											5 B	6 C	7 N	8 O	9 F	10 Ne
11 Na	12 Mg											13 Al	14 Si	15 P	16 S	17 Cl	18 Ar
19 K	20 Ca	21 Sc	22 Ti	23 V	24 Cr	25 Mn	26 Fe	27 Co	28 Ni	29 Cu	30 Zn	31 Ga	32 Ge	33 As	34 Se	35 Br	36 Kr

8.4 Ionization Balance

8.4.1 Photoionization cross sections

Photoionization cross sections for all elements are evaluated using Dima Verner's routine ***phfit***, which fits Opacity Project data where possible, and the best theoretical or experimental data for other cases. The fitting procedure is described in Verner Yakovlev, Band, and Trzhaskovshaya (1993), Verner and Yakovlev (1995), and Verner, Ferland, Korista, and Yakovlev (1996).

8.4.2 Auger multi-electron ejection

Many electrons may be ejected following removal of an inner electron. This is fully treated using electron yields taken from Kaastra and Mewe (1993), see page 263 for more details. This process couples non-adjacent stages of ionization. The code iterates on the ionization solution to keep the system of equations a bi-diagonal matrix (see page 272).

Figure 12 shows photoionization cross sections for each shell of atomic iron, along with plots of the electron yield, taken from Kaastra and Mewe (1993). A single photoionization of the 1s shell can remove as many as 8 electrons.

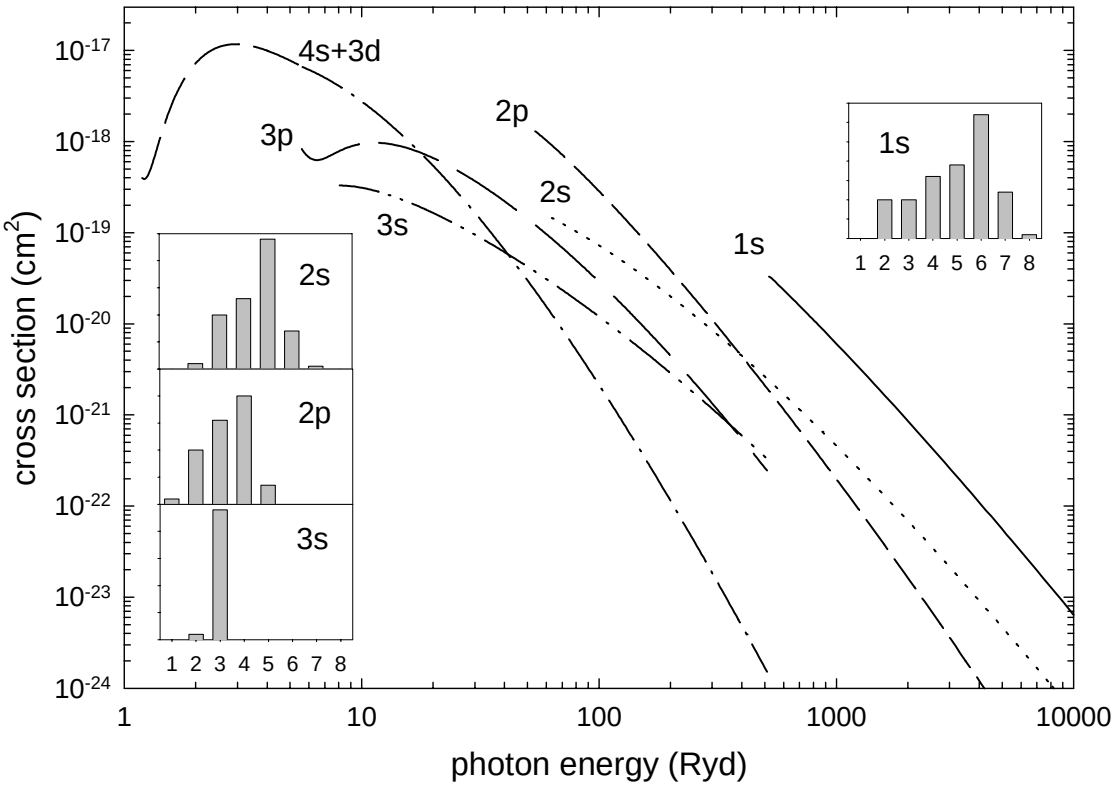

Figure 12 Photoionization cross sections and electron yields for singly ionized iron. Each subshell is shown along with the corresponding electron yield. IronPhoto

8.4.3 Collisional ionization rate coefficients

Fits to collisional ionization rate coefficients are evaluated in Dima Verner's routine ***cfit***. These rates come mainly from Arnaud and Raymond (1992) and Arnaud and Rothenflug (1985), and by interpolation where rates are not given.

8.4.4 Radiative recombination rate coefficients

Radiative recombination rate coefficients are evaluated by Dima Verner's routine ***rrfit***, which uses fits by Arnaud and Raymond (1992), Verner and Ferland (1996), Shull and van Steenberg (1982), and by Landini and Monsignori Fossi (1990, 1991).

8.4.5 Low temperature dielectronic recombination

Dielectronic recombination through low-lying autoionizing states is known to be the dominant recombination mechanism for many ions of second-row elements (i.e., Nussbaumer and Storey 1983). Unfortunately, these have not been computed for most third row or higher elements. This constitutes a major uncertainty in understanding the ionization balance of these elements, and has been described, for instance, by Ali et al. (1991). For those elements where a dielectronic recombination rate coefficient has not been computed and the parent ion is not a closed shell, the mean of the rate coefficient for C, N, O, and Ne is used instead. This assumption can be modified with the **`dielectronic recombination`** command described in part I.

8.4.6 Charge transfer

Rates for charge transfer between hydrogen and the heavy elements are evaluated using Jim Kingdon's routines ***HCTIon*** and ***HCTRecom***. These rates are evaluated in routine ***MakeCharTran***, which is called by routine ***ionize***, and stored into master arrays, ***HCharExcIon*** and ***HCharExcRec***. The rate coefficient for the process $A_{nelem}^{i+1} + H^o \Rightarrow A_{nelem}^{i} + H^+$ is stored as ***HcharExcRec[nelem][I].*** The rate coefficient for the process $A_{nelem}^{i} + H^+ \Rightarrow A_{nelem}^{i+1} + H^o$ is stored as ***HCharExcIon[nelem][I].***

For species more than 4 times ionized, a statistical estimate made by Alex Dalgarno (Ferland et al. 1997) is used. The rate coefficient for transfer between atomic hydrogen and a highly ionized species is given by $1.92\times10^{-9}\ \zeta\ cm^3\ s^{-1}$, where ζ is the charge of the ion. Other atoms are treated analogously.

All of these include the thermal effects of charge transfer, as described by Kingdon & Ferland (1998).

8.5 Ionization Potentials

Table 22 lists ionization potentials for photoionization of the outer shell of the first thirty elements. These are given in Rydbergs for infinite mass nuclei.

Figure 13 shows the number of ions with valence shell ionization potentials within logarithmically increasing energy widths, as a function of the log of the ionization potentials in Rydbergs. Two large peaks occur, one near ~25 Ryd (~350 eV) and a second near ~160 Ryd (~2 keV). The continuum binning used in the code is designed to resolve these as separate features.

8.5.1 Ionization potential pointers

The vector ***ipElement*** contains array indices to thresholds of all valence and inner shell ionization edges of the elements. It has four dimensions. The first dimension is atomic weight of the element, and the second is the ionization stage, 1 for the atom, ranging up to the atomic number of the element. The third dimension is the shell number, 1 for the K-shell, ranging up to 7. The fourth dimension is a set of pointers. One is the lower energy limit or threshold for the shell, 2 is the upper limit as set in routine ***LimitSh***, and element three is the offset pointer to the opacity array.

A parallel two dimensional array, *nsShells[ion][nelem]*, contains the number of shells for the ionization stage i of the element with a given atomic weight. With this nomenclature, the pointer to the valence shell threshold of ionization stage i of an element n would be *ipElement[n,i, nsShells[n,I]]*. These valence pointers are also stored in the array *ipHeavy[nelem][nstag]*).

Table 22 Ionization Potentials of the Elements (Rydbergs)

	1 H	*2 He*	*3 Li*	*4 Be*	*5 B*	*6 C*	*7 N*	*8 O*	*9 F*	*10 Ne*
1	9.996(-1)	1.807	3.963(-1)	6.852(-1)	6.099(-1)	8.276(-1)	1.068	1.001	1.280	1.585
2		4.000	5.559	1.338	1.849	1.792	2.176	2.581	2.570	3.010
3			9.003	1.131(+1)	2.788	3.520	3.487	4.038	4.609	4.664
4				1.600(+1)	1.907(+1)	4.740	5.694	5.689	6.405	7.138
5					2.500(+1)	2.882(+1)	7.195	8.371	8.393	9.275
6						3.601(+1)	4.058(+1)	1.015(+1)	1.155(+1)	1.161(+1)
7							4.903(+1)	5.434(+1)	1.361(+1)	1.524(+1)
8								6.405(+1)	7.011(+1)	1.757(+1)
9									8.107(+1)	8.790(+1)
10										1.001(+2)

Table 22b Ionization Potentials of the Elements (Rydbergs)

	11 Na	*12 Mg*	*13 Al*	*14 Si*	*15 P*	*16 S*	*17 Cl*	*18 Ar*	*19 K*	*20 Ca*
1	3.777(-1)	5.620(-1)	4.400(-1)	5.991(-1)	7.710(-1)	7.614(-1)	9.533(-1)	1.158	3.191(-1)	4.493(-1)
2	3.476	1.105	1.384	1.202	1.450	1.715	1.750	2.031	2.325	8.724(-1)
3	5.264	5.890	2.091	2.461	2.220	2.560	2.911	2.994	3.367	3.742
4	7.270	8.033	8.820	3.318	3.781	3.477	3.930	4.396	4.477	4.944
5	1.017(+1)	1.039(+1)	1.130(+1)	1.226(+1)	4.780	5.342	4.985	5.514	6.075	6.211
6	1.266(+1)	1.371(+1)	1.400(+1)	1.507(+1)	1.620(+1)	6.471	7.131	6.689	7.309	7.996
7	1.532(+1)	1.653(+1)	1.774(+1)	1.812(+1)	1.934(+1)	2.065(+1)	8.393	9.136	8.643	9.349
8	1.942(+1)	1.955(+1)	2.092(+1)	2.228(+1)	2.274(+1)	2.412(+1)	2.560(+1)	1.055(+1)	1.137(+1)	1.082(+1)
9	2.204(+1)	2.412(+1)	2.426(+1)	2.580(+1)	2.732(+1)	2.786(+1)	2.941(+1)	3.105(+1)	1.292(+1)	1.384(+1)
10	1.077(+2)	2.701(+1)	2.935(+1)	2.950(+1)	3.120(+1)	3.286(+1)	3.349(+1)	3.518(+1)	3.703(+1)	1.553(+1)
11	1.212(+2)	1.295(+2)	3.249(+1)	3.499(+1)	3.525(+1)	3.710(+1)	3.890(+1)	3.961(+1)	4.150(+1)	4.350(+1)
12		1.443(+2)	1.533(+2)	3.848(+1)	4.119(+1)	4.150(+1)	4.351(+1)	4.544(+1)	4.627(+1)	4.830(+1)
13			1.693(+2)	1.792(+2)	4.497(+1)	4.790(+1)	4.827(+1)	5.043(+1)	5.253(+1)	5.341(+1)
14				1.965(+2)	2.070(+2)	5.198(+1)	5.511(+1)	5.555(+1)	5.782(+1)	6.010(+1)
15					2.256(+2)	2.370(+2)	5.949(+1)	6.283(+1)	6.329(+1)	6.575(+1)
16						2.568(+2)	2.689(+2)	6.747(+1)	7.115(+1)	7.162(+1)
17							2.900(+2)	3.029(+2)	7.607(+1)	7.989(+1)
18								3.253(+2)	3.389(+2)	8.504(+1)
19									3.626(+2)	3.770(+2)
20										4.020(+2)

Table 22c Ionization Potentials of the Elements (Rydbergs)

	21 Sc	*22 Ti*	*23 V*	*24 Cr*	*25 Mn*	*26 Fe*	*27 Co*	*28 Ni*	*29 Cu*	*30 Zn*
1	5.396(-1)	5.012(-1)	4.954(-1)	4.974(-1)	5.464(-1)	5.808(-1)	5.780(-1)	5.613(-1)	5.678(-1)	6.904(-1)
2	9.408(-1)	9.981(-1)	1.077	1.213	1.149	1.190	1.255	1.335	1.491	1.320
3	1.820	2.020	2.154	2.275	2.475	2.253	2.462	2.596	2.708	2.919
4	5.401	3.180	3.433	3.613	3.763	4.028	3.768	4.035	4.217	4.366
5	6.752	7.298	4.798	5.105	5.321	5.513	5.843	5.593	5.872	6.071
6	8.136	8.783	9.415	6.662	7.037	7.281	7.497	7.938	7.570	7.938
7	1.014(+1)	1.035(+1)	1.107(+1)	1.177(+1)	8.768	9.187	9.481	9.775	1.022(+1)	9.996
8	1.162(+1)	1.252(+1)	1.275(+1)	1.357(+1)	1.430(+1)	1.111(+1)	1.160(+1)	1.191(+1)	1.227(+1)	1.286(+1)
9	1.323(+1)	1.412(+1)	1.513(+1)	1.538(+1)	1.630(+1)	1.717(+1)	1.368(+1)	1.418(+1)	1.463(+1)	1.492(+1)
10	1.654(+1)	1.587(+1)	1.694(+1)	1.796(+1)	1.825(+1)	1.926(+1)	2.024(+1)	1.651(+1)	1.705(+1)	1.749(+1)
11	1.836(+1)	1.948(+1)	1.879(+1)	1.990(+1)	2.102(+1)	2.133(+1)	2.244(+1)	2.359(+1)	1.956(+1)	2.014(+1)
12	5.052(+1)	2.142(+1)	2.264(+1)	2.191(+1)	2.311(+1)	2.431(+1)	2.469(+1)	2.588(+1)	2.711(+1)	2.284(+1)
13	5.562(+1)	5.790(+1)	2.472(+1)	2.608(+1)	2.525(+1)	2.653(+1)	2.786(+1)	2.822(+1)	2.947(+1)	3.085(+1)
14	6.106(+1)	6.344(+1)	6.585(+1)	2.824(+1)	2.962(+1)	2.883(+1)	3.021(+1)	3.162(+1)	3.197(+1)	3.337(+1)
15	6.817(+1)	6.923(+1)	7.172(+1)	7.431(+1)	3.199(+1)	3.359(+1)	3.263(+1)	3.408(+1)	3.557(+1)	3.601(+1)
16	7.416(+1)	7.673(+1)	7.791(+1)	8.063(+1)	8.327(+1)	3.596(+1)	3.763(+1)	3.663(+1)	3.822(+1)	3.984(+1)
17	8.041(+1)	8.313(+1)	8.584(+1)	8.709(+1)	8.996(+1)	9.275(+1)	4.017(+1)	4.199(+1)	4.094(+1)	4.255(+1)
18	8.915(+1)	8.974(+1)	9.261(+1)	9.547(+1)	9.680(+1)	9.981(+1)	1.027(+2)	4.462(+1)	4.652(+1)	4.549(+1)
19	9.466(+1)	9.893(+1)	9.959(+1)	1.026(+2)	1.056(+2)	1.070(+2)	1.106(+2)	1.133(+2)	4.929(+2)	5.130(+1)
20	4.171(+2)	1.047(+2)	1.093(+2)	1.100(+2)	1.131(+2)	1.163(+2)	1.178(+2)	1.211(+2)	1.242(+2)	5.420(+1)
21	4.435(+2)	4.593(+2)	1.154(+2)	1.201(+2)	1.208(+2)	1.241(+2)	1.275(+2)	1.291(+2)	1.318(+2)	1.357(+2)
22		4.870(+2)	5.036(+2)	1.265(+2)	1.314(+2)	1.322(+2)	1.357(+2)	1.392(+2)	1.400(+2)	1.435(+2)
23			5.326(+2)	5.499(+2)	1.382(+2)	1.433(+2)	1.441(+2)	1.478(+2)	1.503(+2)	1.521(+2)
24				5.803(+2)	5.983(+2)	1.504(+2)	1.557(+2)	1.566(+2)	1.597(+2)	1.629(+2)
25					6.300(+2)	6.489(+2)	1.631(+2)	1.687(+2)	1.689(+2)	1.737(+2)
26						6.819(+2)	7.015(+2)	1.763(+2)	1.807(+2)	1.822(+2)
27							7.357(+2)	7.563(+2)	1.900(+2)	1.945(+2)
28								7.923(+2)	8.129(+2)	2.043(+2)
29									8.504(+2)	8.724(+2)
30										9.106(+2)

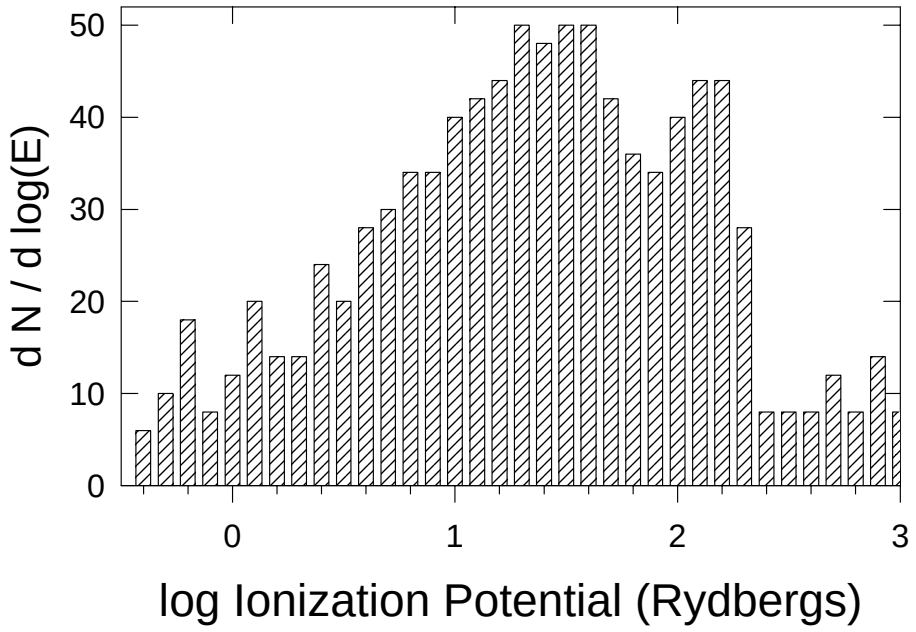

Figure 13 The number of elements with valence shell ionization potentials within logarithmically increasing energy widths is shown as a function of the log off the ionization potential. ipDen

8.6 Heavy Element Variables

8.6.1 Atomic weights

These are stored in atomic mass units, within the vector ***AtomicWeight***. The mass (gm) of unit atomic weight m_{AMU} is stored as the ***physcont.h***.

8.6.2 Ionic and total abundances

Information concerning the abundance of an element and the distribution of this abundance over the various stages of ionization is stored in the two dimensional real array ***xIonFracs***[ionization stage] [atomic number]. This array is the sole member of the common block of the same name. The first dimension of the array ranges from 0 through ***limelm+1***. Element 0 is the total abundance of that element in all gas phase forms, including molecules (but not grains). Elements 1 and higher are the abundances of that element in these stages of ionization (1 is the atom, 2 the first ion, etc). All abundances have units particles cm^{-3}. The second dimension is the atomic number of the element, ranging from 0 (hydrogen) through the value of ***limelm*** (less one) currently 30.

8.6.3 Element names

These are all contained in the *elementnames* structure, defined in the header file *elementnames.h*.

chElementSym Standard chemical symbols for all elements now in the code are stored within this 2-character variable.

chIonStage This is a two character vector ***limelm***+1 long, containing the numbers from 1 through ***limelm***+1. It is used for the spectroscopic designation of the spectrum produced by a level of ionization. C IV would be represented as C 4.

chIonRoman This is a two character vector ***limelm***+1 long, containing the numbers from 1 through ***limelm***+1 expressed as Roman numerals.

chElementName This is an eleven character vector ***limelm*** long with the names of the first ***limelm*** elements.

chElementNameShort This is a four character vector ***limelm*** long with the first four letters of the names of the first ***limelm*** elements.

8.6.4 Photoionization rates

These are stored in the multidimensional vector ***PhotoRate***. The first dimension contains the photoionization rate [0] the low-energy heating rate [1], and the high-energy (secondary ionizing) heat [3]. The second dimension is an index to the shell. These range from 0 to 6, and are 1s, 2s, 2p, 3s, 3p, 3d, 4s. Note that, for neutrals and ions of third row and heavier elements, some of the inner shells may be only partially filled. The last two dimensions give the atomic number of the element and the ionization stage, with the atom being zero.

8.6.5 Fluorescence yields

These are taken from the compilation by Kaastra and Mewe (1993), and are stored in structure ***yield***. The real variable ***vyield*** has 4 dimensions. These are the fraction of ejected electrons corresponding to number. For the latter, the index 1 will return the fraction of ionizations of that shell that eject only 1 electron. The second element is the shell number in Dima's notation (0 for the 1s shell), The atomic number (5 for carbon, etc) and the stage of ionization (1 for the atom) are the last two. The second variable in the structure is an integer array that indicates the most number of electrons that can be ejected.

8.6.6 Ionization potential pointers

These are set within routine ***CreatePoint***, which calls routine ***ipShells*** to actually set the pointers.

8.7 Isoelectronic Sequences

Table 23 lists all isoelectronic sequences for the first thirty elements. For sequences of elements heavier than K the ground configuration is correct for ions twice or more times ionized. For these heavier elements the atom and first ion may have non-standard configurations for the outer shell. The bottom row on the table indicates the shell number, in the nomenclature used for the photoionization shell layering.

8.8 Carbon

Low temperature dielectronic recombination rate coefficients are taken from Nussbaumer and Storey (1983).

Table 23 Isoelectronic Sequences

1 H	***2 He***	***3 Li***	***4 Be***	***5 B***	***6 C***	***7 N***	***8 O***	***9 F***	***10 Ne***
1s ^{2}S	1s^{2} ^{1}S	2s ^{2}S	2s^{2} ^{1}S	2p ^{2}P	2p^{2} ^{3}P	2p^{3} ^{4}S	2p^{4} ^{3}P	2p^{5} ^{2}P	2p^{6} ^{1}S
H 1	He 1	Li 1	Be 1	Bo 1	C 1	N 1	O 1	F 1	Ne 1
He 2	Li 2	Be 2	Bo 2	C 2	N 2	O 2	F 2	Ne 2	Na 2
Li 3	Be 3	Bo 3	C 3	N 3	O 3	F 3	Ne 3	Na 3	Mg 3
Be 4	Bo 4	C 4	N 4	O 4	F 4	Ne 4	Na 4	Mg 4	Al 4
Bo 5	C 5	N 5	O 5	F 5	Ne 5	Na 5	Mg 5	Al 5	Si 5
C 6	N 6	O 6	F 6	Ne 6	Na 6	Mg 6	Al 6	Si 6	P 6
N 7	O 7	F 7	Ne 7	Na 7	Mg 7	Al 7	Si 7	P 7	S 7
O 8	F 8	Ne 8	Na 8	Mg 8	Al 8	Si 8	P 8	S 8	Cl 8
F 9	Ne 9	Na 9	Mg 9	Al 9	Si 9	P 9	S 9	Cl 9	Ar 9
Ne10	Na10	Mg10	Al10	Si10	P 10	S 10	Cl10	Ar10	K 10
Na11	Mg11	Al11	Si11	P 11	S 11	Cl11	Ar11	K 11	Ca11
Mg12	Al12	Si12	P 12	S 12	Cl12	Ar12	K 12	Ca12	Sc12
Al13	Si13	P 13	S 13	Cl13	Ar13	K 13	Ca13	Sc13	Ti13
Si14	P 14	S 14	Cl14	Ar14	K 14	Ca14	Sc14	Ti14	V 14
P 15	S 15	Cl15	Ar15	K 15	Ca15	Sc15	Ti15	V 15	Cr15
S 16	Cl16	Ar16	K 16	Ca16	Sc16	Ti16	V 16	Cr16	Mm16
Cl17	Ar17	K 17	Ca17	Sc17	Ti17	V 17	Cr17	Mm17	Fe17
Ar18	K 18	Ca18	Sc18	Ti18	V 18	Cr18	Mm18	Fe18	Co18
K 19	Ca19	Sc19	Ti19	V 19	Cr19	Mm19	Fe19	Co19	Ni19
Ca20	Sc20	Ti20	V 20	Cr20	Mm20	Fe20	Co20	Ni20	Cu 20
Sc21	Ti21	V 21	Cr21	Mm21	Fe21	Co21	Ni21	Cu 21	Zn 21
Ti22	V 22	Cr22	Mm22	Fe22	Co22	Ni22	Cu 22	Zn 22	
V 23	Cr23	Mm23	Fe23	Co23	Ni23	Cu 23	Zn 23		
Cr24	Mm24	Fe24	Co24	Ni24	Cu 24	Zn 24			
Mm25	Fe25	Co25	Ni25	Cu 25	Zn 25				
Fe26	Co26	Ni26	Cu 26	Zn 26					
Co27	Ni27	Cu 27	Zn 27						
Ni28	Cu 28	Zn 28							
Cu 29	Zn 29								
Zn 30									
1	1	2	2	3	3	3	3	3	3

11 Na	*12 Mg*	*13 Al*	*14 Si*	*15 P*	*16 S*	*17 Cl*	*18 Ar*	*19 K*	*20 Ca*
3s ^{2}S	3s^2 ^{1}S	3p ^{2}P	3p^2 ^{3}P	3p^3 ^{4}S	3p^4 ^{3}P	3p^5 ^{2}P	3p^6 ^{1}S	3d ^{2}D	3d^2 ^{3}F
Na 1	Mg 1	Al 1	Si 1	P 1	S 1	Cl 1	Ar 1	K 1[3]	Ca 1^1
Mg 2	Al 2	Si 2	P 2	S 2	Cl 2	Ar 2	K 2	Ca 2^1	Sc 2^1
Al 3	Si 3	P 3	S 3	Cl 3	Ar 3	K 3	Ca 3	Sc 3	Ti 3
Si 4	P 4	S 4	Cl 4	Ar 4	K 4	Ca 4	Sc 4	Ti 4	V 4
P 5	S 5	Cl 5	Ar 5	K 5	Ca 5	Sc 5	Ti 5	V 5	Cr 5
S 6	Cl 6	Ar 6	K 6	Ca 6	Sc 6	Ti 6	V 6	Cr 6	Mm 6
Cl 7	Ar 7	K 7	Ca 7	Sc 7	Ti 7	V 7	Cr 7	Mm 7	Fe 7
Ar 8	K 8	Ca 8	Sc 8	Ti 8	V 8	Cr 8	Mm 8	Fe 8	Co 8
K 9	Ca 9	Sc 9	Ti 9	V 9	Cr 9	Mm 9	Fe 9	Co 9	Ni 9
Ca10	Sc10	Ti10	V 10	Cr10	Mm10	Fe10	Co10	Ni10	Cu 10
Sc11	Ti11	V 11	Cr11	Mm11	Fe11	Co11	Ni11	Cu 11	Zn 11
Ti12	V 12	Cr12	Mm12	Fe12	Co12	Ni12	Cu 12	Zn 12	
V 13	Cr13	Mm13	Fe13	Co13	Ni13	Cu 13	Zn 13		
Cr14	Mm14	Fe14	Co14	Ni14	Cu 14	Zn 14			
Mm15	Fe15	Co15	Ni15	Cu 15	Zn 15				
Fe16	Co16	Ni16	Cu 16	Zn 16					
Co17	Ni17	Cu 17	Zn 17						
Ni18	Cu 18	Zn 18							
Cu 19	Zn 19								
Zn 20									
4	4	5	5	5	5	5	5	6	6

21 Sc	*22 Ti*	*23 V*	*24 Cr*	*25 Mm*	*26 Fe*	*27 Co*	*28 Ni*	*29 Cu*	*30 Zn*
3d^3 ^{4}F	3d^4 ^{5}D	3d^5 ^{6}S	3d^6 ^{5}D	3d^7 ^{4}F	3d^8 ^{3}F	3d^9 ^{2}D	3d^{10} ^{1}S	4s ^{2}S	4s^2 ^{1}S
Sc 1	Ti 1	V 1	Cr 1	Mm 1	Fe 1	Co 1	Ni 1	Cu 1	Zn 1
Ti 2	V 2	Cr 2	Mm 2	Fe 2	Co 2	Ni 2	Cu 2	Zn 2	
V 3	Cr 3	Mm 3	Fe 3	Co 3	Ni 3	Cu 3	Zn 3		
Cr 4	Mm 4	Fe 4	Co 4	Ni 4	Cu 4	Zn 4			
Mm 5	Fe 5	Co 5	Ni 5	Cu 5	Zn 5				
Fe 6	Co 6	Ni 6	Cu 6	Zn 6					
Co 7	Ni 7	Cu 7	Zn 7						
Ni 8	Cu 8	Zn 8							
Cu 9	Zn 9								
Zn 10									
6	6	6	6	6	6	6	6	7	7

8.9 Nitrogen

Low temperature dielectronic recombination rate coefficients are taken from Nussbaumer and Storey (1983). Photoionization from the excited ^{2}D level of N^o is included, and can be the dominant ionization mechanism in well-shielded regions.

8.10 Oxygen

Low temperature dielectronic recombination rate coefficients are taken from Nussbaumer and Storey (1983).

Photoionization from the first two excited states of O^{2+} is included as a general ionization mechanism. This can dominate the ionization of the ion since it occurs

[3] Neutral and first ion have non-standard filling.

behind the He^{+} - He^{++} ionization front, which shields the region from 4 Ryd and higher radiation. Similarly, photoionization from the first excited state and all inner shells of O^{o} are included.

8.10.1 The O I model atom

A partial Grotrian diagram for the O I atom considered in the Lβ–O I fluorescence problem is shown in Figure 14. Multiplet averaged transition probabilities are taken from unpublished Opacity Project data, and the collision strengths are from the $\bar{g}$ approximation for collisions between electrons and neutrals. Rates for fluorescence between the two transitions are computed as in Netzer et al. (1985).

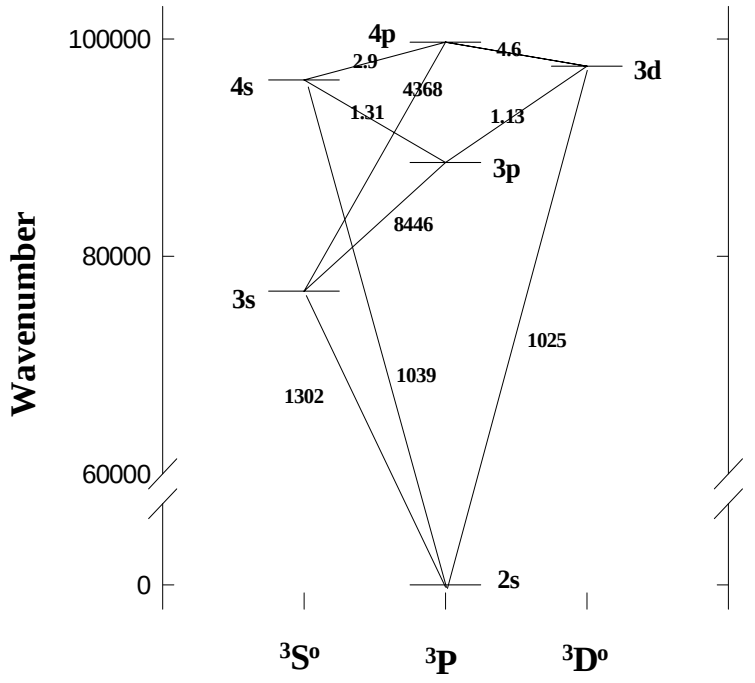

Figure 14 The levels of O^{o} included in the calculation of the OI–Lβ pumping problem are shown. oigrot

Level populations including all physical processes are computed in routine ***oilevl***. This routine is called by routine ***p8446***, which is responsible for the interactions between the hydrogen and oxygen atoms.

8.11 Neon

Low temperature dielectronic recombination rate coefficients are taken from Nussbaumer and Storey (1987).

8.12 Magnesium

Low temperature dielectronic recombination rate coefficients for recombination to the atom are taken from Nussbaumer and Storey (1986). Rate coefficients have not been computed for recombination to the ions. Means of CNO are used.

Photoionization from the excited $^2P^o$ level of Mg^{+} is included as a general Mg^{+} destruction mechanism using Opacity Project data retrieved from ***TOPBase***. This can easily be the dominant Mg^{+} destruction mechanism in BLR calculations since the excited state has an ionization potential below 1 Ryd. The code will generate a comment at the end of the calculation if this is a competitive Mg^{+} destruction mechanism.

8.13 Aluminum

Low temperature dielectronic recombination rate coefficients for recombination to the atom and first ion are taken from Nussbaumer and Storey (1986). Rate coefficients have not been computed for recombination to other ions. Means of CNO are used.

8.14 Calcium

Low temperature dielectronic recombination rate coefficients have not been computed for this element. Means of CNO are used.

8.14.1 The Ca II model atom

The Ca II ion is treated as a five–level atom plus continuum. The model atom is shown in Figure 15, and is similar to that described by Shine and Linsky (1974). Collision strengths for j-mixing collisions are from Saraph (1970). Collision and radiative data for the 4s - 4p transition are taken from the compendium of Mendoza (1983), and all other collision data are from Chidichimo (1981) and Saraph (1970). Radiative data for the 3d - 4p and 4s - 3d transitions are from Black, Weisheit, and Laviana (1972); these are in good agreement with the calculations of Osterbrock (1951). The compendium by Shine and Linsky (1974) provides photoionization cross sections for excited levels, which are adopted here. Photoionization of the excited ^{2}D level by Lα (Wyse 1941) and all other line or continuum sources is explicitly included. Recombination contributions to the population of individual levels are included by dividing the excited state recombination coefficient among the excited levels considered, according to their statistical weight and the rules of LS coupling.

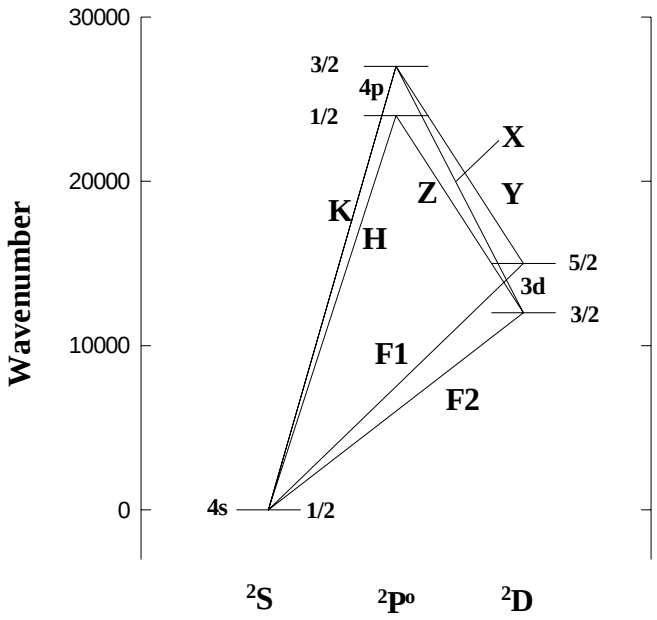

Figure 15 The five levels of Ca^+ included in the calculations are shown. The wavelengths of the predicted lines are K (3934), H (3969), X (8498), Y (8542), Z (8662), F1 (7291), and F2 (7324). ca2grot

All Ca II transitions (including the forbidden lines) can become quite optically thick. Radiative transfer is treated with the escape probability formalism, assuming incomplete redistribution, including destruction by background opacities.

8.15 Iron

Low temperature dielectronic recombination rate coefficients have not been computed for this element. Means of CNO are used. Charge transfer rate coefficients are from Neufeld and Dalgarno (1989), Neufeld (1989) and Ferland, Korista, Verner, and Dalgarno (1997).

8.15.1 The FeII model atom

The Fe II ion is described by Verner et al. (1989) and in sections of Part I of this document. In the current implementation up to 376 levels can be included. is an area of extensive activity. Figure 16 shows the lowest 16 levels of the atom and some of the lines predicted.

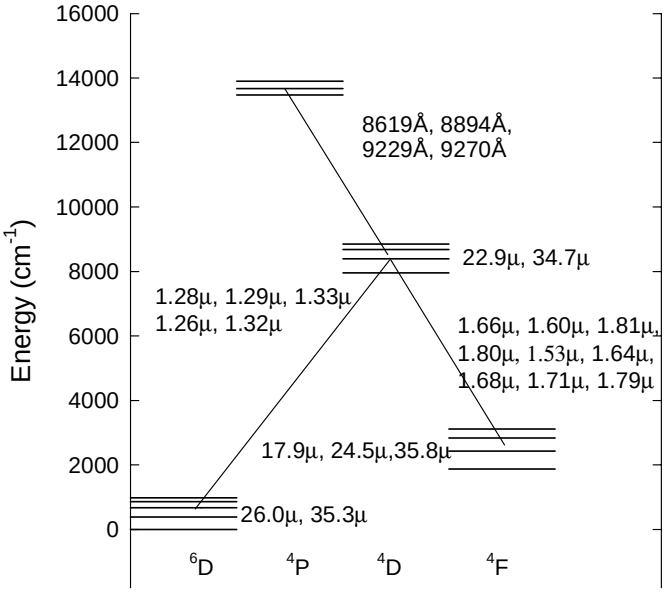

Figure 16 The sixteen level atom used to compute FeII IR emission. Lines predicted are indicated.

8.15.2 The FeIV model atom

FeIV is treated as a twelve-level atom, with energies from Sugar and Corliss (1985), transition probabilities from Garstang (1958), and collision strengths from Berrington and Pelan (1996). Figure 17 shows the model atoms with the lines predicted by the code indicated.

8.15.3 Fe Kα emission

The intensity of the Fe Kα line is predicted including both recombination and fluorescence. Figure 18 shows the fluorescence yield and Kα energy. The line predictions are separated into "cold" iron (i.e., iron with M-shell electrons present) and "hot" iron (those ionization states producing lines with energies greater than ~6.4 keV). This includes the recombination and collisional contribution. The "TOTL" Kα is the sum of the two.

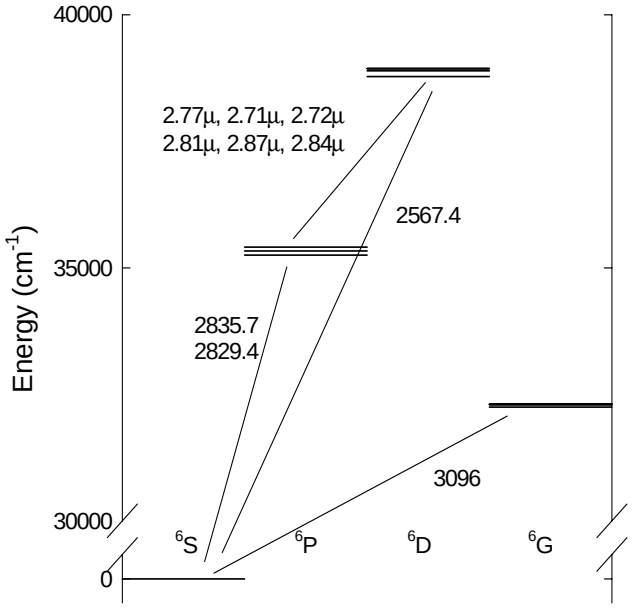

Figure 17 The twelve level atom used to compute FeIV emission. Lines predicted are indicated.

8.16 Heavy Element Opacities

Figure 19 shows a calculation of the opacity of a solar gas with very low ionization.

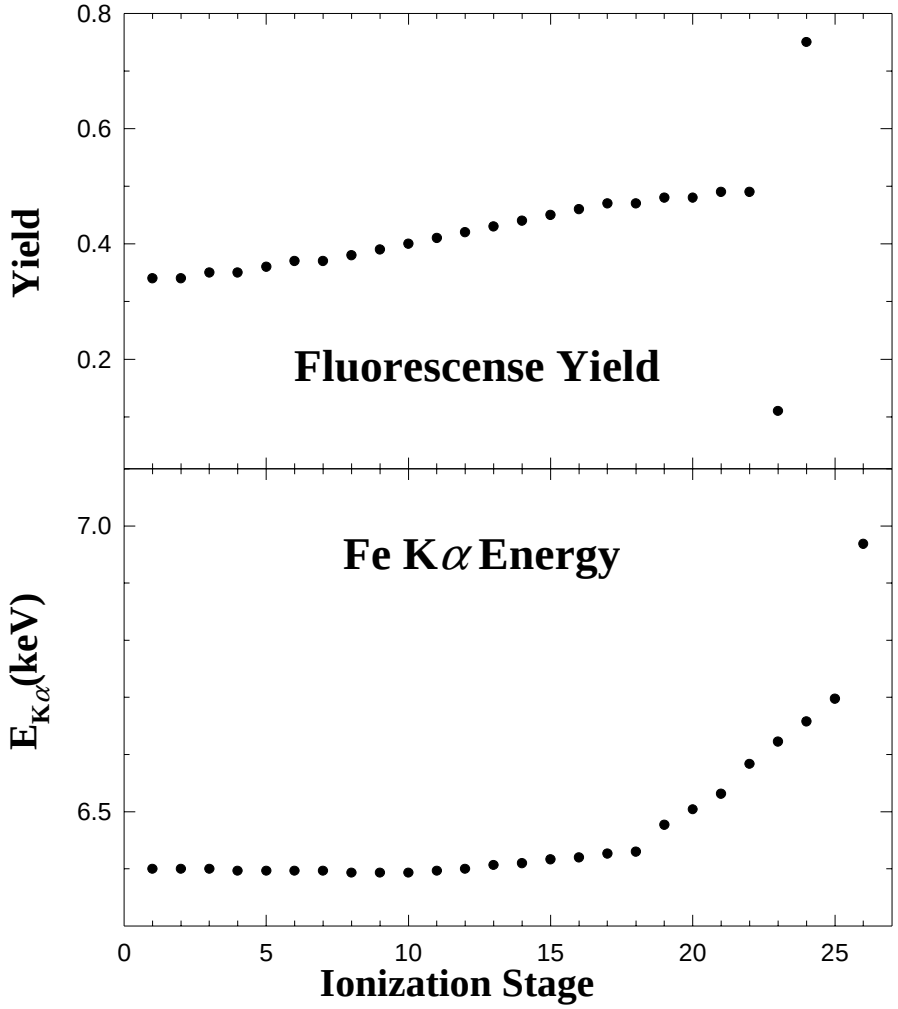

Figure 18 The fluorescence yield and energy of the emitted Fe Kα photon are shown as a function of ionization stage. feka

8.17 Overall Reliability

Table 24
Ionization Balance Reliability

	1 H	*2 He*	*3 Li*	*4 Be*	*5 B*	*6 C*	*7 N*	*8 O*	*9 F*	*10 Ne*
1	A	A	A			A	A	A		
2		A	A	A		A	A	A		A
3			A	A	A	A	A	A		A
4				A	A	A	A	A		A
5					A	A	A	A		A
6						A	A	A		A
7							A	A	A	A
8								A	A	A
9									A	A
10										A

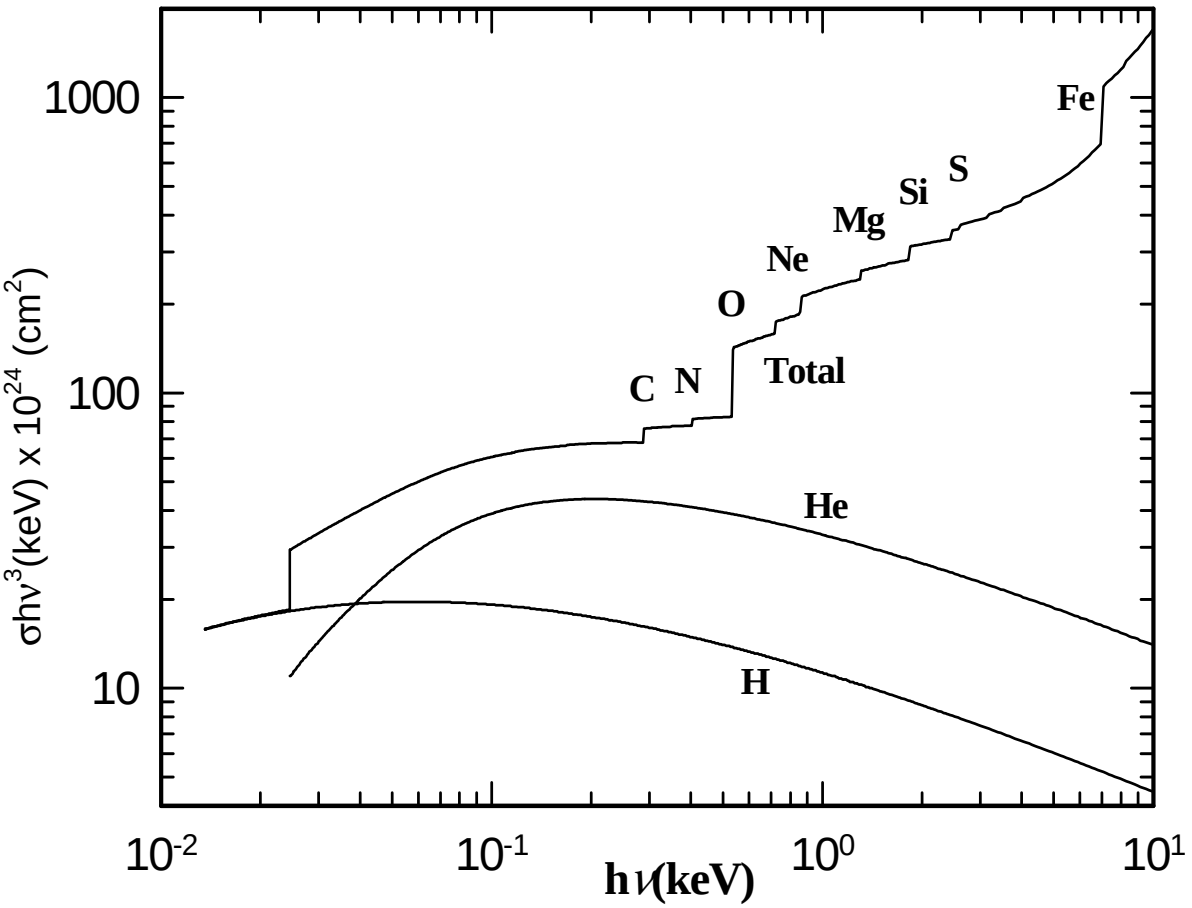

Figure 19 The opacity of a neutral gas with solar abundances is shown as a function of energy. The curve is scaled to allow direct comparison with conventional calculations of opacity at X-Ray energies (i.e., Morrison and McGammon 1983). hevopc

Ionization Balance Reliability Continued

	11 Na	*12 Mg*	*13 Al*	*14 Si*	*15 P*	*16 S*	*17 Cl*	*18 Ar*	*19 K*	*20 Ca*
1	A	A	A							
2		A	A							
3			A							
4				A						
5					A					
6						A				
7							A			
8								A		
9	A								A	
10	A	A								A
11	A	A	A							
12		A	A	A						
13			A	A	A					
14				A	A	A				
15					A	A	A			
16						A	A	A		
17							A	A	A	
18								A	A	A
19									A	A
20										A

Ionization Balance Reliability Continued

	21 Sc	22 Ti	23 V	24 Cr	25 Mn	26 Fe	27 Co	28 Ni	29 Cu	30 Zn
1										
2										
3										
4										
5										
6										
7										
8										
9										
10										
11	A									
12		A								
13			A							
14				A						
15					A					
16						A				
17							A			
18								A		
19	A								A	
20	A	A								A
21	A	A	A							
22		A	A	A						
23			A	A	A					
24				A	A	A				
25					A	A	A			
26						A	A	A		
27							A	A	A	
28								A	A	A
29									A	A
30										A

It is difficult to estimate the overall uncertainty present in an ionization balance calculation. The current photoionization cross-section data are based on accurate experiments or the Opacity Project (Verner et al. 1996). These should be accurate to roughly 10% except near resonances. Although resonances are included in the Opacity Project data, the positions of these resonances are uncertain by more than their width because the OP was not intended as an atomic structure calculation. Recombination coefficients including low temperature dielectronic recombination have yet to be computed for the majority of the stages of ionization of the elements now in Cloudy, but recombination from parent ions with closed shells is not affected, and good rates exist (Verner and Ferland 1996).

It is possible to make a subjective estimate of the uncertainty in the calculation of the ionization balance for nebular temperatures. Table 24 lists the elements now included in the calculations and gives this estimate of the uncertainty. For recombination from a closed shell autoionization resonances do not occur near threshold, recombination is primarily radiative, and the calculations should be virtually exact. Dielectronic recombination rates are also known for those species treated by Nussbaumer and Storey. These are given a quality weighting of A.

These uncertainties refer to the ionization balance of an optically thin cell of gas at nebular temperatures. The intensities of emission lines will be less uncertain than this for two reasons. First, the thermostat effect of any collisionally excited line prevents its intensity from changing by much. Second is the fact that the integrated column density in an ion is affected as much by (fairly exact) quantities such as the

ionization structure of H or He, as by the atomic data of a particular ion. At coronal temperatures the Burgess mechanism dominates, and the situation should be somewhat better.

8.18 The Bi-Diagonal Matrix

The ionization-recombination balance equations are written as a series of *n* equations coupling adjacent levels of ionization, i.e.,

$$n_z \Gamma_z^{eff} = n_{z+1} \sum n_x \alpha_{z+1} \quad . \tag{258}$$

where the effective photoionization rate Γ includes all ionization processes (photoionization of valence and inner shells, collisional ionization, charge transfer ionization, etc) and is modified to include the Auger effect. The total recombination rate coefficient $\sum n_x \alpha_{z+1}$ includes all recombination processes (dielectronic, radiative, 3-body, charge transfer). In much of the following this total recombination rate coefficient will be written simply as $n_e \alpha_e$, with the implicit understanding that all recombination processes are actually included.

The vector ***destroy[ion] [nelem]*** contains total destruction rates. ***create[ion] [nelem]*** is the total creation rates. The resulting ionization balance is solved in routine ***BiDiag***.

9 THERMAL EQUILIBRIUM

9.1 Overview

This section describes the system of equations setting the local thermal balance of a cloud. The electron temperature is the only thermodynamic quantity used to characterize a photoionized cloud. The electron velocity distribution is predominantly Maxwellian (Bohm and Aller 1947) although a trace constituent of non-thermal electrons may contribute when high-energy photons are present (Spitzer & Tomasko 1968). A kinetic temperature can then characterize the electron velocity distribution. This in turn is defined by the balance between processes that add energy (heat) and remove energy (cool) the electrons.

Heating or cooling can be defined relative to either the ground state or continuum, and this difference has caused some confusion in the literature. Cloudy defines heating and cooling relative to the continuum, as in Osterbrock (1989). Note that, in this scheme of bookkeeping, photoionization contributes an amount of heat given by $h(\nu-\nu_o)$, where $h\nu_o$ is the ionization potential of the atom or ion and ν is the photon energy. Emission of a recombination line *does not* constitute a cooling process. Heating and cooling rates are computed in cgs units (ergs, not Rydbergs) throughout Cloudy.

9.2 Thermal Stability

The criterion for thermal stability used by Cloudy is that the net cooling (i.e., cooling minus heating) has a positive temperature derivative (Field 1965). This can be expressed as

$$\frac{d(\Lambda - G)}{dT} > 0 \quad . \qquad (259)$$

The code will print a "u" next to the temperature in the zone results, and make a comment in the end, if possibly thermally unstable solutions were found. The criterion used by the code is that the derivative *at constant density* (isochoric) be positive. The more traditional criterion is that the derivative *at constant pressure* (isobaric) be positive (Field 1965).

The fact that the code identifies a region as possibly thermally unstable does not necessarily show that it is. The derivatives used in equation 259 are those found during the search for the thermal solution. As such they are evaluated out of equilibrium as part of the temperature solver. Their primary purpose was not to perform this thermal stability analysis. A section of Part III of this document goes into more detail about the stability check performed by the code, and how to do a better one.

9.3 Compton Energy Exchange

There are two parts to the Compton energy exchange problem. First, photons scatter off an electron at an angle θ, causing a change of photon energy due to Compton recoil given by

$$\frac{\Delta\varepsilon_{-}}{\varepsilon_o} = \left[1 - \frac{1}{1+\left(\varepsilon_o / m_e c^2\right)(1-\cos\theta)}\right] \quad . \tag{260}$$

For isotropic scattering the median scattering angle corresponds to cos θ = 0.5. Scattering by thermal electrons crates a shift with a distribution centered at

$$\frac{\Delta\varepsilon_{-}}{\varepsilon_o} = \frac{4kT}{m_e c^2} \tag{261}$$

and a standard deviation given by

$$\frac{\sigma}{\varepsilon_o} = \sqrt{\frac{2kT}{m_e c^2}} \tag{262}$$

(see, e.g., Zycki et al. 1994).

The net volume-heating rate (erg s^{-1} cm^{-3}) due to Compton energy exchange is given by

$$G_{Comp} - \Lambda_{Comp} = \frac{4\pi n_e}{m_e c^2}\left\{\int \sigma_h J_\nu h\nu\left[1+\eta_\nu\right] d\nu - 4kT\int \sigma_c J_\nu \, d\nu\right\} \tag{263}$$

(see, for instance, Levich and Sunyaev 1970; and Krolik, McKee, and Tarter 1981). The two terms in braces are the heating and cooling terms respectively, while the factor in brackets in the first term accounts for heating due to both spontaneous and stimulated Compton scattering. Induced Compton heating is important when η_ν is large at frequencies where $h\nu \geq kT$. In fact it is, at most, a few percent effect in most circumstances.

The terms σ_h and σ_c appearing in equation 263 are the effective energy exchange (scattering) cross section for energy exchange, and differ from the Thomson cross section for energies $h\nu \sim m_e c^2$, where the Klein-Nishina cross section must be used. The numerical fits to Winslow's (1975) results, as used by Krolik, McKee, and Tarter (1981) and kindly provided by Dr. C.B. Tarter, were used. Defining

$$\alpha = \left\{1 + \nu_{Ryd}\left(1.1792\times10^{-4} + 7.084\times10^{-10}\nu_{Ryd}\right)\right\}^{-1} \tag{264}$$

and

$$\beta = \left\{1 - \alpha\nu_{Ryd}\left(1.1792\times10^{-4} + 2\times7.084\times10^{-10}\nu_{Ryd}\right)/4\right\} \quad , \tag{265}$$

where ν_{Ryd} is the photon frequency in Rydbergs, the Compton energy-exchange rate coefficients are then $\sigma_h = \sigma_T \alpha$ and $\sigma_c = \sigma_T \alpha\beta$. Tests show that these are in excellent (much better than 1%) agreement with Guilbert's (1986) calculations for $h\nu < 10$ MeV, the energies where Guilbert's calculations are valid.

The total Compton heating-cooling rates are evaluated zone by zone in routine ***highen***. The coefficients for the heating and cooling terms, i.e., α and the product $\alpha\beta$, are calculated at the beginning of the calculation and stored in the vectors ***csigh***(ν) and ***csigc***(ν). The heating is determined by summing over the continuum;

$$G_{Comp} = \frac{n_e}{mc^2}\,\sigma_T\left(h\nu_{Ryd}\right)^2 \sum \alpha_i\,\varphi_i\,\nu_i^2\left(1+\eta_i\right) \tag{266}$$

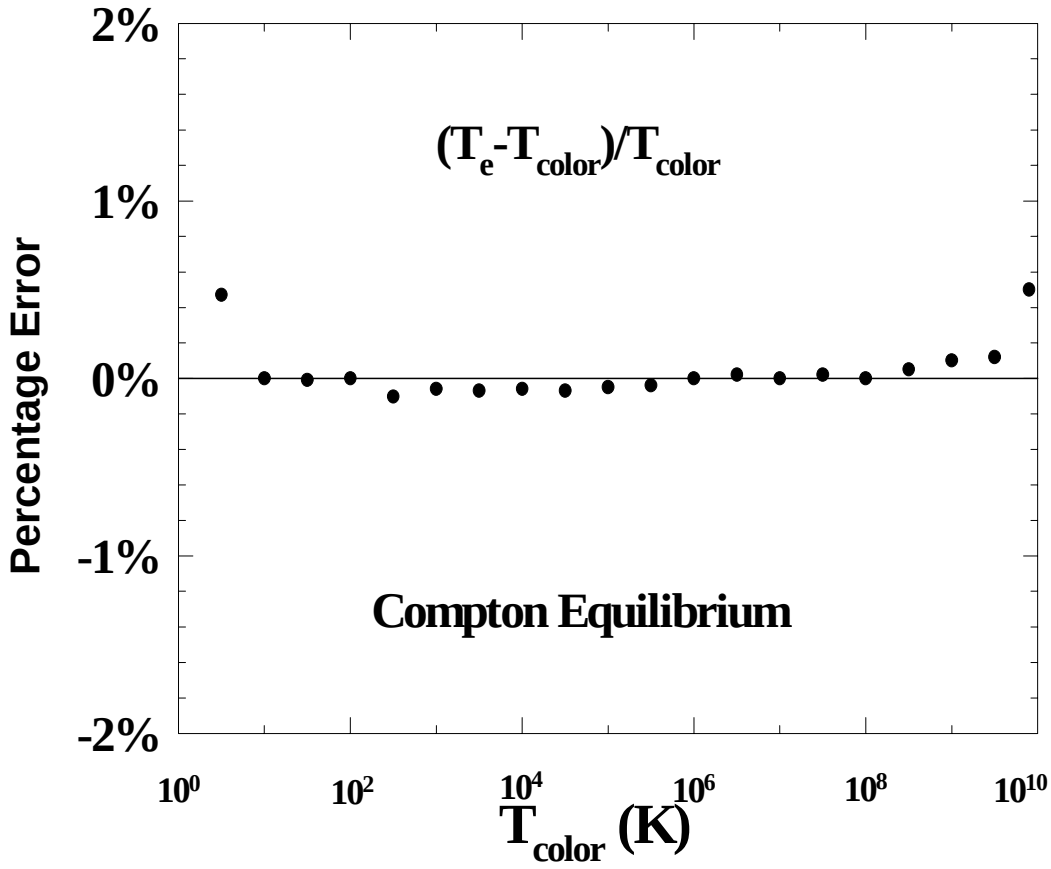

Figure 20 Thermal equilibrium in the Compton Limit. Calculations are for blackbody continua of various temperatures, given as T_{color} along the x-axis. The energy density temperature T_u is set equal to T_{color}. The density is adjusted to maintain ionization parameters U ~ 10^{10}, so that the thermal equilibrium equations are dominated by the Compton exchange problem. The deviation of the computed equilibrium temperature T_e from the asymptotic Compton temperature T_{color} is shown. Compton

where φ_i is the photon flux, stored in the vector variable ***flux***, η_i is the photon occupation number, σ_T is the Thomson cross section, and ν_i is the photon energy in Rydbergs, stored in the vector variable ***anu***.

Figure 20 shows results of a series of calculations in which Compton energy exchange was the dominant physical process affecting the temperature. These are a series of models in which the gas was irradiated by black body continua in strict thermodynamic equilibrium (i.e., $T_u = T_{color}$) and various hydrogen densities. Over the temperature range 3 K $\le T_{color} \le 10^{10}$ K the computed equilibrium electron temperature equaled the color temperature within much better than 1% ($\langle T_e - T_{color} \rangle / T_{color} = -0.00073 \pm 0.0019$).

The input streams for the two limiting cases (for temperatures of $10^{9.5}$ K and 3 K respectively) follow[4];

[4]The high temperature example will not run on an IEEE 32-bit machine. The continuum overflows because of its extreme energy density. The high temperature tests must be computed on a machine with a longer word, such as a Cray.

```
title Compton limit; high temperature limit
blackbody 9.5 lte % lte sets blackbody in strict T.E.
hden 10           % low enough for Compton to dominate
stop zone 1
print short
tolerance 0.0001  % set fine tolerance to check temp exactly


title Compton limit; low temperature limit
black linear 3 lte           % set to 3K
lowest temperature linear 2K % allow equil temp below 10K
brems 5                      % must have ionizing radiation
ionization parameter -5      % but not too much
hden -10                     % set HDEN but does not matter
eden -2                      % add some free electrons
stop zone 1
print short
tolerance 0.0001
```

The intended temperature range of validity for Cloudy is 2.8 K– 10^{10} K. Over the more limited range 10 K – 10^{9} K the computed Compton temperature, for conditions in which strict TE is expected, is generally equal to the color temperature within three significant figures (see Figure 20). At temperatures much greater than 10^{9} K the electrons become relativistic; Cloudy is not intended for these conditions. For temperatures much less than 10 K the computed temperature fails high because the energy bandwidth of the continuum array does not extend below 1.001×10^{-8} Ryd. As a further test, the models presented by Krolik, McKee, and Tarter (1981) were recomputed with excellent agreement (typically within 3%) with their computed Compton temperatures.

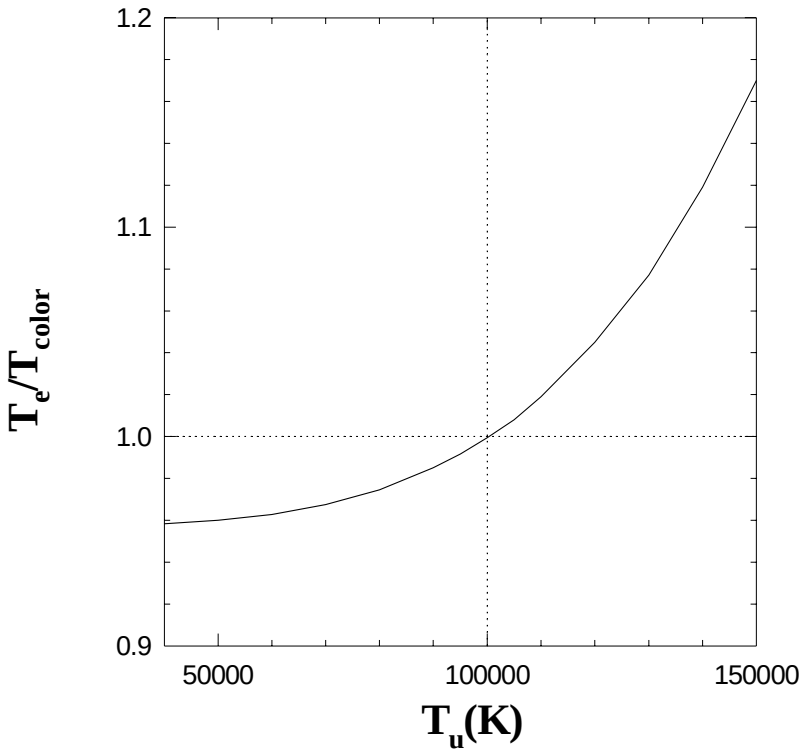

Figure 21 Calculations are for 10^5 K blackbodies and various values of the energy density temperature T_u, indicated along the x-axis. The ratio of the computed equilibrium temperature T_e to the color temperature T_{color} is shown. The two are equal when the energy density and color temperatures are equal. cmpnlte

For a blackbody radiation field with $T_u \neq T_{color}$ the Compton temperature will not be equal to T_{color} because induced scattering will not contribute the required amount of heating-cooling. This case is shown in Figure 21, the results of a series of

calculations in which the energy density temperature was varied (this is shown as the x-axis), but the color temperature held fixed at 10^5 K.

Note also that when $T_u > T_{color}$ induced Compton heating drives T_e *above* T_{color}. Only when the color and energy density temperatures are equal do the equilibrium and color temperatures match.

9.4 Bound Compton Ionization, Heating

Compton scattering can ionize atoms for photons of sufficiently high energy (≈2.3 keV for hydrogen). Rates for bound Compton scattering are computed in routine ***highen***.

9.5 Expansion Cooling

Adiabatic cooling (erg cm^{-3} s^{-1}) due to the hydrodynamic expansion of the gas is given by

$$\Lambda_{\rm exp} = -\frac{DU}{Dt} = -\frac{p}{\rho}\frac{D\rho}{Dt} - U\nabla\cdot\mathbf{v} \approx kT\frac{dn}{dt} = nkT\left[\frac{a}{v}+\frac{2v}{r}\right] \quad \text{erg s}^{-1}\ \text{cm}^{-3} \qquad (267)$$

where n, a, v, and r are the total particle density, acceleration, wind velocity, and radius respectively. This cooling term is only included when a wind geometry is computed.

9.6 Free-free Heating-Cooling

The volume free-free heating rate is given by

$$G_{ff} = 4\pi\int_{\nu_l}^{\infty} n_e\,\alpha_\nu(ff)\,J_\nu\,d\nu \qquad (268)$$

where the free-free cross section is denoted by $\alpha_\nu(ff)$ and ν_l is the low energy limit of the code (1.001×10^{-8} Ryd). The continuum J_ν is the sum of the attenuated incident radiation field and the OTS line fields. Diffuse reemission, mainly free-free emission, *is not* included in this integral, as discussed below.

The cooling by free-free emission, and the subsequent absorption of this radiation, must also be treated. The rate is evaluated in routine ***coolr***.

The code works with the difference between cooling and heating, since this is numerically more stable than considering each term as an independent heat source or coolant. The net heating or cooling is calculated in routine ***HydroCool***, and is stored directly in the heating array there.

Cooling due to diffuse continua are treated by defining a critical frequency ν_c as follows. Gas at a depth r into the cloud is transparent to photons with energies above a critical frequency ν_c such that

$$\tau_c = \int_0^r \kappa(\nu_c)\ f(r)dr = \int_0^r \alpha_\nu(ff,\nu_c)\,n_e\,f(r)dr = 1 \qquad (269)$$

and optically thick at lower frequencies. The critical frequency ν_c is evaluated for each zone. The energy in Rydbergs is stored as ***tff***, while the variable ***ntff*** points to the cell in the continuum array.

The free-free cooling rate is then given by

$$\Lambda_{ff}(\tau) = \int_{\nu_c}^{\infty} n_e \alpha_\nu (ff)\, 4\pi B_\nu (T_e)\, d\nu = \Lambda_{ff}(0) \times \exp(-h\nu_c / kT) \qquad (270)$$

where $\Lambda_{ff}(0)$ is the optically thin cooling rate and $B_\nu(T)$ is Planck's function. This is equivalent to assuming that, for $\nu < \nu_c$, where the cloud is optically thick, free-free heating and cooling exactly balance, as suggested by Kirchhoff's law and detailed balance considerations. Energies below ν_c are not included in free-free heating. This critical frequency is not allowed to be less than the plasma frequency for the current conditions.

9.7 Photoelectric Heating, Recombination Cooling

The net heating rate due to photoelectric heating less spontaneous and induced recombination cooling of level *n* is given by

$$G = G_{n,\kappa} - \Lambda_{ind,n} - \Lambda_{spon,n} \qquad (271)$$

where the volume heating rate due to photoionization is

$$G_{n,\kappa} = n_n \int_{\nu_o}^{\infty} \frac{4\pi J_\nu}{h\nu} \alpha_\nu\, h(\nu - \nu_o)\, d\nu \quad , \qquad (272)$$

the volume cooling rate due to induced recombination is

$$\Lambda_{ind,n} = n_e n_p\, 4\pi\, P_n^* \int_{\nu_o}^{\infty} \frac{J_\nu}{h\nu} \alpha_\nu \exp(-h\nu / kT)\, h(\nu - \nu_o)\, d\nu \quad , \qquad (273)$$

and the cooling rate due to spontaneous radiative recombination is

$$\Lambda_{spon,n} = n_e n_p kT \beta(T,n) \quad . \qquad (274)$$

The cooling rate coefficient β(T,n) is evaluated as described on page 233.

9.8 Collisional Ionization - Three-Body Recombination

The net volume-heating rate due to collisional ionization less three-body recombination is given by

$$G_{n,\kappa} - \Lambda_{n,\kappa} = \sum_n P_n^* n_e n_p C_{n,\kappa}\, h\nu_o (1 - b_n) \qquad (275)$$

where $C_{n,\kappa}$ is the collisional ionization rate and b_n is the departure coefficient. The term $(1 - b_n)$ is only large and positive for very low levels, in which $I_n > kT$. Far from thermodynamic equilibrium this is usually a net cooling process only for the ground term. This is because departure coefficients for excited states are nearly unity while the ground level usually has $b_n \approx 1$.

9.9 H^- Heating and Cooling

9.9.1 H^- bound-free

The volume-heating rate due to spontaneous absorption (photodissociation) is

$$G_{H^-} = n(H^-) \int_{\nu_o}^{\infty} \frac{4\pi J_\nu}{h\nu} \alpha_\nu\, h(\nu - \nu_o)\, d\nu \quad (\text{erg s}^{-1}\ \text{cm}^{-3}) \qquad (276)$$

sub

where symbols have their usual meaning. The volume-cooling rate due to induced radiative attachment is

$$\Lambda_{ind,H^-} = n_e n_{H^o} P^*(H^-) \int_{\nu_o}^{\infty} \alpha_\nu \frac{4\pi J_\nu}{h\nu} \exp\left(-h\nu / kT\right) h\left(\nu - \nu_o\right) d\nu \quad \left(\text{erg s}^{-1}\text{ cm}^{-3}\right) \tag{277}$$

while the volume cooling rate for spontaneous radiative attachment is

$$\Lambda_{spon,H^-} = n_e n_{H^o} 8\pi P^*(H^-) \int_{\nu_o}^{\infty} \alpha_\nu \frac{\nu^2}{c^2} \exp\left(-h\nu / kT\right) h\left(\nu - \nu_o\right) d\nu \quad . \tag{278}$$

9.9.2 H- free-free

Free-free heating and cooling by H- is also significant, although less so than bound-free heating. This is included, making the appropriate correction for stimulated emission, using the cross sections given by Vernazza et al. (1981; see also Bates et al. 1975).

Under most circumstances H- bound-free heating and cooling are much more important than H- free-free processes. This is surprising at first sight, since standard opacity curves comparing bound-free and free-free opacities (Bates et al. 1975; Mihalas 1978) show that the two are comparable. These curves are for strict thermodynamic equilibrium, with H- departure coefficients of unity. Like the ground state of hydrogen, the departure coefficient for H- is often many orders of magnitude larger than unity, so that the H- bound-free opacity and the resulting heating greatly exceed the H- free-free opacity.

9.10 Line Cooling, Hydrogen and Helium

The net heating due to line collisional deexcitation less excitation is given by

$$G_{line} - \Lambda_{line} = \sum_{n=1}^{N-1} \sum_{u=n+1}^{N} P_n^* n_e n_p C_{u,n} h\nu_{u,n} \left(b_u - b_n\right) \tag{279}$$

where C_{un} is the downward collision rate. Far from thermodynamic equilibrium collisions involving the ground state tend to cool the gas (since $b_1 \gg 1$) and those between levels with $n \geq 3$ tend to heat the gas (since b_n tends to increase with n).

9.11 Heavy Element Line Heating and Cooling

9.11.1 Overview

All lines of the heavy elements are treated as data types ***EmLine***. The following sections describe that format and the major routines for computing heating and cooling for *n*-level atoms of the heavy elements. Emission lines are often optically thick. All lines are transferred using escape probabilities, by determining level populations including both collisional and radiative processes (see, for example, Elitzur 1991). Line masing can sometimes occur, and again is treated using escape probabilities.

In all cases the net cooling due to a transition is given as

$$\Lambda_{line} = h\nu_{u,l}\left(n_l C_{l,u} - n_u C_{u,l}\right) \text{ [erg cm}^{-3}\text{ s}^{-1}\text{]} \tag{280}$$

where the populations of levels are given by n_i and C_{ij} is the collision rate. This cooling is evaluated in routines ***level2***, ***level3***, ***levelN***, and ***beseq***. Each routine is responsible for evaluating the line intensity, cooling, and destruction rate, and entering these into the appropriate stacks. Each routine sets the following attributes.

Lines can act to **heat** rather than cool the gas it is irradiated by a continuum with a brightness temperature greater than the gas temperature at the line energy. This is an important gas heating mechanism for PDRs, for instance (Tielens and Hollenbach 1985). If η is the photon occupation number of the attenuated incident continuum at the line frequency, then the rate atoms are excited from the ground level is given by $\eta\varepsilon A_{ul}$ where ε is the line escape probability. A fraction $C_{ul}/(C_{ul}+\varepsilon A_{ul})$ of these radiative excitations is converted into heat by collisional de-excitation. The net heating due to this process is then

$$G_{FIR} = n_l \eta_\nu \varepsilon_{lu} A_{ul} \left(\frac{C_{ul}}{C_{ul} + \varepsilon_{lu} A_{ul}} \right) h\nu \quad [\text{erg cm}^{-3}\ \text{s}^{-1}] \tag{281}$$

where n_l is the density of the ground level. This process is included for all transferred lines.

9.11.2 Two level atoms

Cooling due to collisional excitation of two level atoms of the heavy elements is evaluated in routine ***level2***. This routine does the following: a) finds the abundance of the two levels by balancing collisional and radiative processes, subject to the sum $n_l + n_u$ = abundance. b) adds the line cooling (or heating) to the total cooling, c) adds the line derivative to *dC/dT*, d) evaluates the fraction of the escaping line destroyed by background opacity, e) adds this to the local OTS radiation field, f) records the line opacity population $n_l - n_u g_l/g_u$. The populations of the atom are saved in the vector ***PopLevls***.

9.11.3 Three level atoms

The level populations, cooling, and line destruction by background opacity sources are computed for three level atoms in routine ***level3***.

Routine ***level3*** is called with three arguments, the three line structures. Level populations corrected for stimulated emission are returned in the individual line arrays. The true level populations, with no correction for stimulated emission, are returned in the array ***PopLevls***.

Levels are designated by the indices 0, 1, and 2, with 0 the lowest level. The routine is called with three line structures, indicated by *t10*, *t21*, and *t20*, each representing the downward radiative transition between the indicated levels. Any one of these transitions may be a dummy transition, (using the dummy line *TauDmmy*). The total rates between any two levels $i \Rightarrow j$ is indicated by R_{ij}. This includes collisions, radiative decays (both photon escape and destruction by background opacity), and induced transitions. If the total abundance of the parent ion is A, the three balance equations are

$$n_0 + n_1 + n_2 = A \tag{282}$$

$$n_0 \left(R_{01} + R_{02} \right) = n_1 R_{10} + n_2 R_{20} \tag{283}$$

$$n_1\left(R_{10}+R_{12}\right)=n_2R_{21}+n_0R_{01}\ . \tag{284}$$

Setting n_0 to A-n_1-n_2 equation 283 becomes

$$\left(R_{01}+R_{02}\right)\left(A-n_1-n_2\right)=n_1R_{10}+n_2R_{20}\,. \tag{285}$$

After gathering terms this equation becomes

$$A\left(R_{01}+R_{02}\right)=n_1\left(R_{10}+R_{01}+R_{02}\right)+n_2\left(R_{20}+R_{01}+R_{02}\right)\ . \tag{286}$$

Substituting for n_0, equation 284 becomes

$$n_1\left(R_{10}+R_{12}\right)=n_2R_{21}+R_{01}\left(A-n_1-n_2\right). \tag{287}$$

Gathering terms this equation becomes

$$n_1\left(R_{10}+R_{12}+R_{01}\right)=AR_{01}+n_2\left(R_{21}-R_{01}\right)\ \ . \tag{288}$$

Solving 286 for n_1 we obtain

$$n_1=\frac{A\left(R_{01}+R_{02}\right)}{R_{10}+R_{01}+R_{02}}-\frac{n_2\left(R_{20}+R_{01}+R_{02}\right)}{R_{10}+R_{01}+R_{02}} \tag{289}$$

and solving 288 we find

$$n_1=\frac{AR_{01}}{R_{10}+R_{12}+R_{01}}+\frac{n_2\left(R_{21}-R_{01}\right)}{R_{10}+R_{12}+R_{01}} \tag{290}$$

Equating the two and gathering terms we obtain

$$n_2\left(\frac{R_{21}-R_{01}}{R_{10}+R_{12}+R_{01}}+\frac{R_{20}+R_{01}+R_{02}}{R_{10}+R_{01}+R_{02}}\right)=\frac{A\left(R_{01}+R_{02}\right)}{R_{10}+R_{01}+R_{02}}-\frac{AR_{01}}{R_{10}+R_{12}+R_{01}} \tag{291}$$

with the solution

$$n_2=A\left(\frac{\left(R_{01}+R_{02}\right)}{R_{10}+R_{01}+R_{02}}-\frac{R_{01}}{R_{10}+R_{12}+R_{01}}\right)\Bigg/\left(\frac{R_{21}-R_{01}}{R_{10}+R_{12}+R_{01}}+\frac{R_{20}+R_{01}+R_{02}}{R_{10}+R_{01}+R_{02}}\right)\ . \tag{292}$$

In the code the term in the numerator in the previous equation is called *alpha*, and the denominator *beta*. Replacing n_2 in equation 289 we obtain

$$n_1=\left[A\left(R_{01}+R_{02}\right)-n_2\left(R_{20}+R_{01}+R_{02}\right)\right]\Big/\left(R_{10}+R_{01}+R_{02}\right)\ . \tag{293}$$

Again the two terms are called *alpha* and *beta*.

9.11.4 N level atoms

The level populations, cooling, and line destruction by background opacity sources are computed for *n* level atoms in routine ***LevelN***. The number of levels *n* can be as large as the value of ***limLevelN*** (currently 10), which appears as a constant within the routine.

Routine ***LevelN*** is called with 12 arguments. These are:

nlev This is the number of levels for the model atom. It is an integer and can be as large as the value of ***limLevelN***, currently 20.

abund This is the total abundance of the ion. The total population of the ***nlev*** levels will add up to this quantity, which is a real variable.

g This is a real vector of dimension ***nlev***. It contains the statistical weights of the levels.

ex This is a real vector of dimension ***nlev***. It contains the excitation temperature (K) of the ***nlev*** levels *relative to ground.* The excitation temperature of the lowest level should be zero.

p This is a real vector of dimension ***nlev*** and is the computed population of the ***nlev*** atom. It will contain all zeros if ***abund*** is zero, and ***p[0]*** will equal ***abund*** if the temperature is so low that the Boltzmann factors are zero for the current cpu.

data This two dimensional real vector is ***data[nlev][nlev]. Data[u][l***] is the effective transition probability (the product of the Einstein A and the escape probability) for the transition. ***Data[l][u***] is the collision strength for the transition.

dest This two dimensional real vector is ***dest[nlev][nlev***]. ***Dest[u][l***] is the destruction rate (the product of the Einstein A and the destruction probability) for the transition. ***dest[l][u***] is not used.

pump This two dimensional real vector is ***pump[nlev][nlev]***. ***pump[u][l***] is the upward pumping rate (the Einstein $B_{lu}J$) for the transition.

ipdest This two dimensional integer vector is ***ipdest[nlev][nlev]***. ***ipdest[u][l***] is the pointer to the line in the continuum array. ***LevelN*** computes the local line destruction rate and includes this in the OTS field if the pointers are non-zero. If this vector contains zeros then no flux is added to the OTS field.

cooltl This real variable is the total cooling in ergs/s produced by the model atom.

chLabel This is a 4 character variable, and is a label for the ion.

negpop This logical variable is true if any of the level populations were negative.

9.11.5 Li Sequence

Table 25 gives the stronger lines of Li-sequence ions. ***Level3*** is used for this sequence.

Table 25 Lithium Sequence Lines

N	*Ion*	*j=3/2-1/2*	*j=1/2-1/2*	*j=3/2-1/2*	*j=1/2-1/2*
6	C IV	1548.195	1550.770	312.422	312.453
7	N V	1238.821	1242.804	209.270	209.303
8	O VI	1031.9261	1037.6167	150.088	150.124
10	Ne VIII	770.409	780.324	88.134	
12	Mg X	609.79	624.95	57.88	57.92
13	Al XI	550.03	568.15	48.30	48.34
14	Si XII	499.40	520.67	40.92	
16	S XIV	417.61	445.77	30.43	
18	Ar XVI	353.92	389.14	25.53	
20	Ca XVIII	302.215	344.772	18.69	18.73
26	Fe XXIV	192.017	255.090	10.62	10.66

9.11.6 Boron Sequence

Figure 23 shows levels within the lowest three configurations of the Boron sequence.

9.11.7 Beryllium sequence atoms

The level populations, cooling, and line destruction by background opacity sources are computed for a specialized four level atom in routine ***beseq***.

Routine ***beseq*** is called with five arguments, the collision strengths between the excited triplet levels, the line optical depth array for the fast (j=1 to j=0) transition, and the transition probability for the slow (j=2 to j=0) transition. Induced processes are only included for the fast transition. The collision strength stored in the line array is the collision strength for the entire multiplet. Rates to levels within the term are assumed to scale as the ratio of level statistical weight to term statistical weight. The level populations for the ground and excited states, with no correction for stimulated emission, are returned in the array ***PopLevls***, contained in the common block of the same name.

The total rates between any two levels $i \Rightarrow j$ is indicated by R_{ij}. This includes collisions, radiative decays (for the fast transition, both photon escape and destruction by background opacity, and induced transitions). If the total abundance of the parent ion is A, the three balance equations are

$$n_0 + n_1 + n_2 + n_3 = A \tag{294}$$

$$n_0\left(R_{01} + R_{02} + R_{03}\right) = n_1 R_{10} + n_2 R_{20} + n_3 R_{30} \tag{295}$$

$$n_1\left(R_{10} + R_{12} + R_{13}\right) = n_3 R_{31} + n_2 R_{21} + n_0 R_{01}\ . \tag{296}$$

$$n_2\left(R_{20} + R_{21} + R_{23}\right) = n_3 R_{32} + n_1 R_{12} + n_0 R_{02}\ . \tag{297}$$

Collisions are included in all these terms. R_{32} includes the slow downward line escape, while R_{02} and R_{20} includes escape, destruction by background opacity, and fluorescent excitation - deexcitation. In the code the terms on the LHS of equations

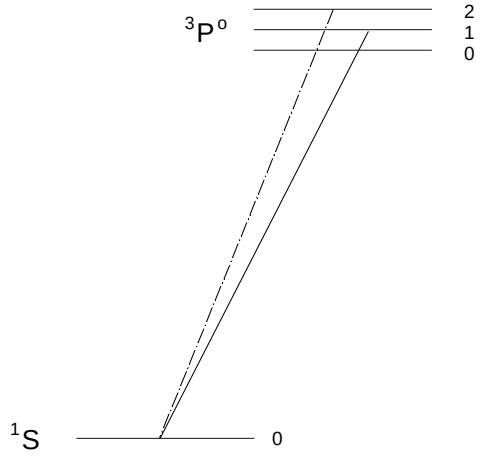

Figure 22 The four levels included in routine beseq. beseq1

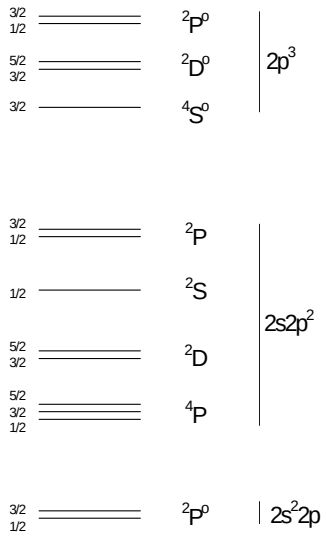

Figure 23 Energy Level Diagram for Boron Sequence. Boron

296, 297, and 295 are called α, β, and γ.

9.12 Evaluation of the Cooling Function

9.12.1 Total cooling

The cooling function is evaluated in routine ***coolr***. This in turn calls other routines which compute cooling for individual elements. Each individual coolant is entered as a separate quantity in the array ***cooling***. Under some extreme circumstances agents that are normally coolants can actually heat the gas. Negative coolants are stored in a parallel array, ***heatnt***.

The total cooling is the sum of this array, referred to as the variable ***ctot***, and evaluated in routine ***SumCool***.

9.12.2 The cooling derivative

As the cooling is evaluated, its approximate temperature derivative is computed by making analytic expansions of the cooling for individual agents. For instance, collisionally excited lines of positive ions have collisional excitation rates that depend on the product

$$\Lambda_{line} \approx n_e n_{ion} t^{-1/2} \exp(-T_{exc} / T_e) \qquad (298)$$

where T_{ex} is the excitation temperature of the line. In this case the derivative of the cooling function can be expressed as

$$\frac{d\Lambda_{line}}{dT} \approx n_e n_{ion} \frac{d}{dT} T^{-1/2} \exp(-T_{exc} / T) = \Lambda_{line} \left[\frac{T_{exc}}{T^2} - \frac{1}{2T} \right] \qquad (299)$$

This derivative is used by the thermal predictor-corrector routine to make the initial guess at a new temperature. This is approximate since both electron and ionic densities also depend on the temperature.

The variable ***tsq1*** contains the value $1/T^2$, while ***halfte*** is $1/2T$. Both are part of the structure ***cooling***.

9.13 Evaluation of the Heating Function

Various contributions to the heating function are evaluated throughout the code. Each heating agent stores its contribution to the total heating within a cell of the two dimensional array *heating*. The total heating is always the sum of the total contents of the *heating* array.

Heating due to photoionization of all stages of ionization of the 30 elements now included in the code are stored as *heating[nelem][ion]*. Heating due to photoionization of ionization stage *i* (*i=0* for the atom) of element with atomic number *nelem* is stored as *heating[i][nelem]*. Other agents are stored in unused portions of this array. The total heating and its temperature derivative are deduced from this array in routine ***SumHeat***. The heating is stored as the variable *htot*.

Line heating is treated as a special case. The level population routines are supposed to sort lines into heating and cooling components, and put these into the line vector as *ipLnHeat* and *ipLnCool*. The entries stored as *ipLnHeat* are then added to the heating stack as *heating[22][0]* when the total line cooling is evaluated in routine ***SumCool***. The entries stored as *ipLnCool* are added to the cooling stack here too.

Normally this will catch all negative coolants early. Attempts to add negative cooling to the cooling stack are trapped and stored in the array *heatnt*. This is added to the total heating in routine ***SumCool***.

9.14 Equilibrium Calculations

9.14.1 Hydrogen only

Figure 24 shows the results of a series of calculations in which the full set of statistical and thermal equilibrium equations are solved for thin cells of hydrogen gas with various densities.

The ionizing continuum is, in all cases, a black body with $T_{color} = 5 \times 10^4$ *K*, and the energy density of the radiation field is varied, up to the thermodynamic equilibrium limit, $T_u = T_{color}$.

Although the gas temperature in the thermodynamic equilibrium limit does not depend on the gas density, the physical processes that drive the gas to this temperature do. Thermal equilibrium calculations were performed with three densities chosen to span a fairly wide range. For low densities ($n(H) = 10^5$ cm^{-3}) the gas remains highly ionized for all values of T_u shown and the temperature in thermodynamic equilibrium is set by the balance between Compton and inverse-Compton scattering. The intermediate density case ($n(H) = 10^{10}$ cm^{-3}) reaches thermodynamic equilibrium with ~3/4 of the heating-cooling set by Compton scattering and the remainder due to free-free and free-bound processes. The high-density ($n(H) = 10^{15}$ cm^{-3}) case reaches its thermodynamic equilibrium temperature with a balance between free-free (1/3 of the total) and free-bound (2/3 of the total) processes. In all cases the level populations and electron temperature are within ~1% of their expected thermodynamic equilibrium values when $T_u = T_{color}$.

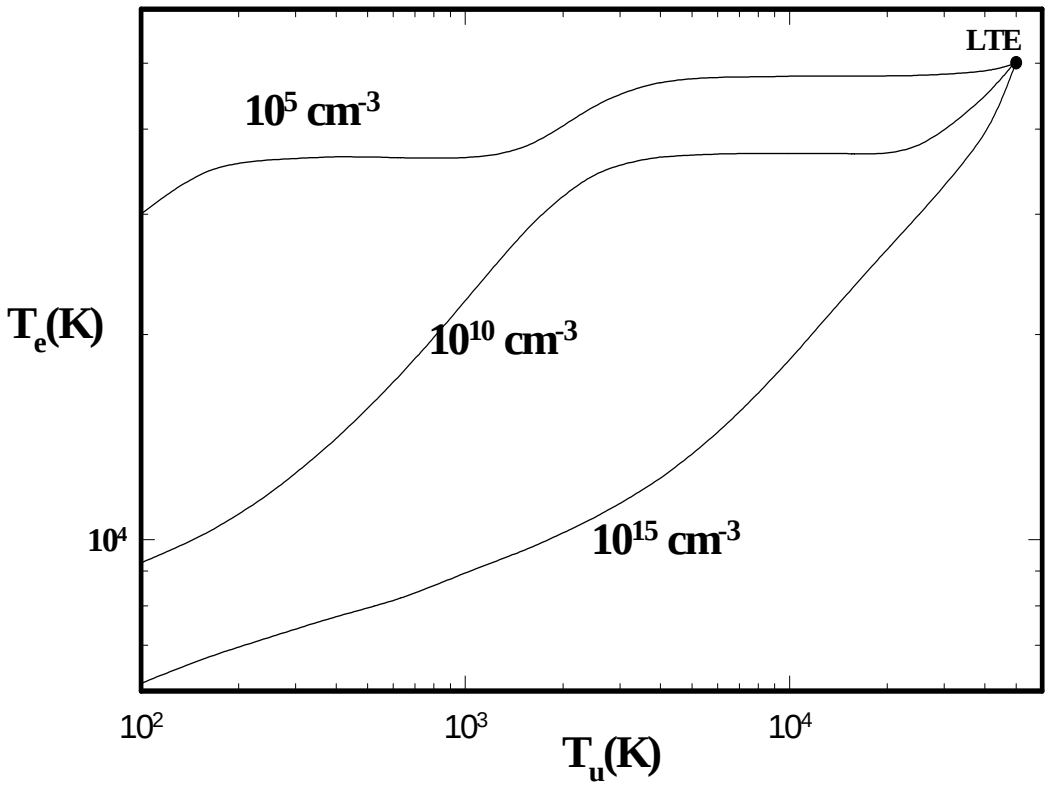

Figure 24 Thermal equilibrium calculations for an optically thin gas with 3 hydrogen densities are shown as a function of the radiation field energy density, parameterized as T_u. Ionization is by a 5×10^4 K black body. Various processes drive the gas to thermodynamic equilibrium when T_u reaches 5×10^4 K. hlte

9.14.2 Metal rich gas

Simulations of very metal rich gas is now a major emphasis of the code (Hamann and Ferland (1993; Ferland et al. 1996). In these cases the thermal and ionization balance is totally dominated by the heavy elements.

Figure 25 shows the results of a series of calculations in which gas with strongly enhanced abundances of the heavy elements is exposed to a series of black body radiation fields with different temperatures and energy densities. Ferland and Rees (1988) and Ferland and Persson (1989) gave analogous calculations for pure hydrogen clouds. The filled circle represents the cases where the energy densities of the radiation field are equal to the color temperature, and strict thermodynamic equilibrium is expected. This is indeed the case. The distribution of ionization for each color temperature is radically different, but the line interactions with this field bring the gas to the expected equilibrium temperature. This tests both the ionization and thermal balance in this extreme environment.

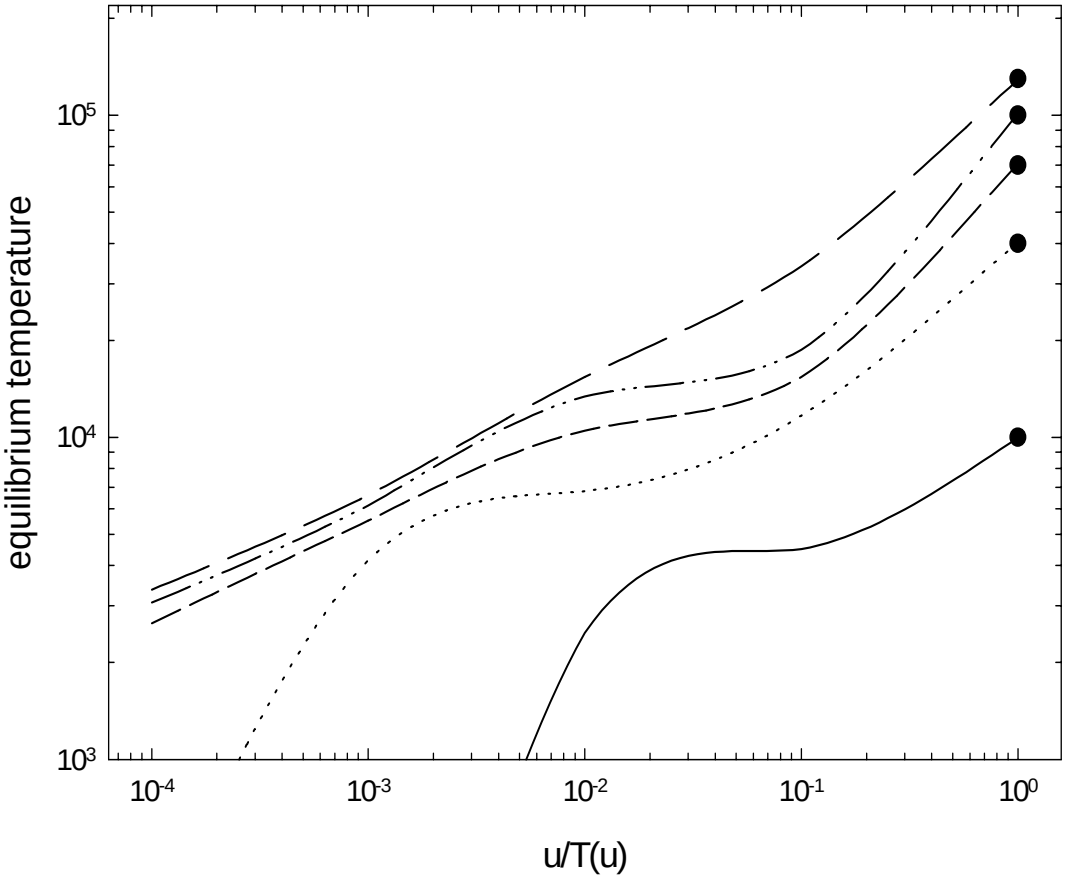

Figure 25 Equilibrium temperature of gas exposed to five black bodies with various energy density temperatures. The color temperatures of the blackbodies are 10,000K, 40,000K, 70,000K, 100,000K and 130,000K. The metallicity was 10 times solar (Hamann and Ferland 1993) so that heating cooling of thousands of heavy element emission lines dominates the thermal equilibrium. The simulation is of an optically thin cell of gas with density 10^{10} cm^{-3} (results do not depend on this density). The x-axis is the local energy density relative to the energy density in thermodynamic equilibrium at that temperature. The gas goes to thermodynamic equilibrium when the radiation field does (the color and energy density temperatures are equal). highzlte

10 GRAIN PHYSICS

10.1 Overview

The following discussion outlines some physical processes relating to grains, as incorporated in Cloudy. It is adopted from Baldwin et al. (1991), and was written in close collaboration with P.G. Martin.

Several grain populations, types of graphite and "astronomical silicates", are available. Usually one of each type, for a total of two, is selected, although there is no limit to the number of grain populations. Optical properties like opacity of the species are based on a realistic power-law size distribution. Other properties (like potential and temperature) are computed for a mean grain size rather than calculated for each individual size.

The following describes the "old", default, grains that were originally incorporated into the code in the late 1980's (Baldwin et al. 1991). These use optical properties that correspond to averages over the grain size distribution. The new ('pgains") grains both resolves the grain size distribution and includes single photon heating for the smaller grains. This new treatment will be described in van Hoof et al. (2001) and this document at a later time.

10.2 Grain Opacity

Grains are not included in the calculation by default. When enabled with the **grain** command the default mixture has interstellar medium (ISM) properties. Grains more similar to those seen in Orion or planetary nebulae are also available.

10.2.1 ISM grains

The optical constants for the default (ISM) grain species are from the calculations of Martin and Rouleau (1990). These extend the work of Draine and Lee (1984) to ionizing energies where the grains are strongly absorbing. These opacity calculations were based on the Mathis, Rumpl, and Nordsieck (1977) power-law size distribution to simulate interstellar extinction in diffuse clouds.

10.2.2 Orion grains

Grains within the Orion Nebula have a relatively large ratio of total to selective extinction R and an exceptionally gray opacity in the ultraviolet. These are both indicative of a deficiency in small grains and a larger mean grain size. To account for this, a second set of opacity functions is included, the Orion group. For this the value of the smallest size (a_-) in the Mathis et al. (1977) size distribution was increased from 0.0025μm to 0.03μm. While this simple adjustment of the size distribution is not entirely adequate for explaining the details of the visible and near ultraviolet Orion extinction curve (Mathis and Wallenhorst 1981), it should be an improvement for the ionizing ultraviolet portion, which is most important.

The Orion extinction curve is designed to simulate the large R grains observed in this HII region. Relative to ISM standard grains the total amount of grain material was preserved, so that α_{abs} in the infrared and in the EUV and X-Ray regions remains

unchanged. The main differential effect is to lower the cross section through a broad peak at 1 Ryd.

10.2.3 PN grains

Infrared opacities for the silicate component are taken from unpublished work by K. Volk. Ultraviolet silicate cross sections, and the graphite constituent, are standard ISM.

10.2.4 Extinction

The ISM extinction properties, both effective scattering (subscript *scat*) and absorption (subscript *abs*), are shown in Figure 26.

The quantities plotted are cross sections (cm^2) per H nucleon: $\sigma = \kappa/n(H)$, where κ (cm^{-1}) is the opacity due to grains and $n(H)$ (cm^{-3}) is the local density of H in any form. Rather than the total scattering cross section σ_s an effective scattering cross section $\sigma_{scat} = \sigma_s (1-g)$ is plotted. This discounts the radiation scattered near the forward direction. The asymmetry parameter g approaches unity at high and low energies, particularly for larger grains, so that σ_{scat} becomes much less than α_{abs}

The optical depth τ is σ times the hydrogen column density (or κ integrated over the path). Absorption attenuates the incident radiation field as $\exp(-\tau_{abs})$. The effects of scattering are more difficult to model. In an open geometry, scattering attenuates approximately as $(1+0.5\ \tau_{scat})^{-1}$. However, in a closed geometry, to within factors of order unity, the scattered light is not lost from the beam, and the scattering opacity can be ignored. In either case, effective grain scattering optical depth is generally fairly small through the ionized nebula at ionizing energies.

10.3 Photoelectric Emission

As discussed below, photoelectric emission from grains contributes directly to heating the gas and, through the grain potential U_g established, affects radiative and collisional heating of the grains and the grain drift velocity.

The photoionization rate of a grain, per unit projected area, is

$$\Gamma_g = \int_{\nu_o}^{\infty} Q_{abs} \frac{4\pi J}{h\nu} \hat{Y}\, d\nu \qquad (300)$$

where $\hat{Y}$ is the effective photoelectric yield per absorbed photon, Q_{abs} is the absorption efficiency factor, and $4\pi J/h\nu$ symbolizes the photon flux of direct, diffuse, and OTS radiation fields. For the OTS line component, the integral is of course just a sum over the line photons that are sufficiently energetic. The threshold for photoemission, to be determined self-consistently, is given by $h\nu_o = \max\{V_n+V_g, V_n\}$, where V_n is the photoelectric threshold for a neutral grain and $V_g = eU_g$.

V_g will depend on grain size through Q_{abs} and $\hat{Y}$. In the present implementation, a typical V_g is defined for each species by using Q_{abs} averaged over the size distribution: $Q_{abs} = \alpha_{abs}/\Sigma = \kappa_{abs}/n(H)\,\Sigma$. The projected grain area per H, Σ, is similar for each species: 2.1×10^{-22} cm^2 for graphite and 2.4×10^{-22} cm^2 for silicates.

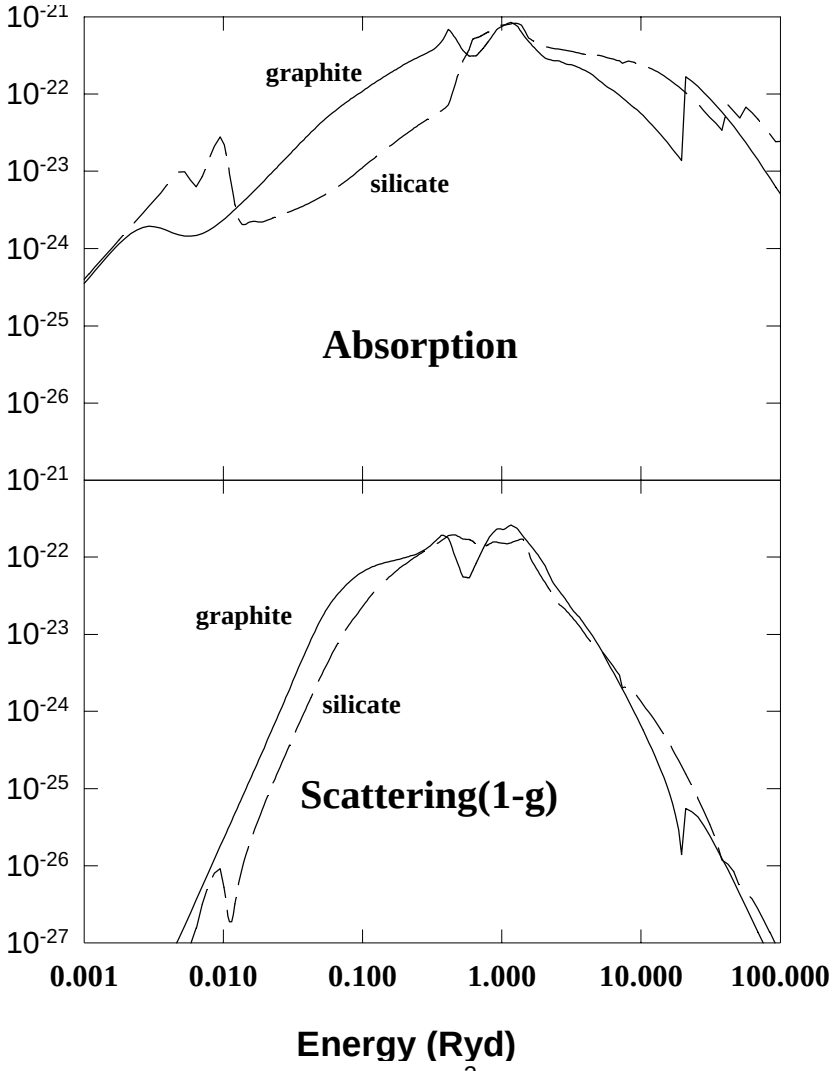

Figure 26 The absorption and scattering cross sections (cm^2 per hydrogen nucleon) for the two ISM grain populations, graphite and silicate, are shown. The effective scattering cross section is the scattering cross section multiplied by *1-g*, where *g* is the asymmetry parameter. grnopc

$\hat{Y}$ is constructed as follows. The basic laboratory data measure the yield (per absorbed photon) for a neutral surface, Y_n. For each incident photon energy $h\nu$, the photoelectrons emerging from the neutral surface have varying energies E, with a probability distribution $p_n(E)$. To account for electron escape from finite sized

grains, yields measured for semi-infinite sheets in the laboratory have to be corrected by a factor $f(E)$ (which introduces a size dependence). Such a correction would change the shape of the probability distribution as well as increase the integrated emission from a neutral surface (Draine 1978 gives an approximate expression for the overall increase). Then, formally

$$\hat{Y} = Y_n \int_{E_o}^{(h\nu - V_n)} f\, p_n\, dE \qquad (301)$$

where $E_0 = \max\{0\ ,\ V_g\}$ introduces the fact that the lowest energy photoelectrons do not escape from positively charged grains.

The form adopted is

$$Y_n = \min\left\{Y_o\left(1 - V_n / h\nu\right), Y_1\right\} \tag{302}$$

for $h\nu \geq V_n$, and V_n = 8 eV and Y_0 = 0.5 is assumed for both grain populations; according to Draine (1978) this combination gives about the right amount of photoelectric emission to heat neutral H I clouds in interstellar space ($h\nu \leq$ 13.6 eV). For the higher energies a cap at Y_1 = 0.2 is introduced, which is suggested by experimental data. For p_n a simple form that is independent of E (Draine 1978) is adopted:

$$p_n = \left(h\nu - V_n\right)^{-1} \quad . \tag{303}$$

While only approximate, this induces the physically correct response (decrease) in $\hat{Y}$ (and the photoelectric heating) when the grain is positively charged. Because the form of *f(E)* is highly uncertain *f = 1* is assumed (this again avoids a size dependency). Extension of the flat cap in Y_n to high energies also addresses this issue to some degree. With these assumptions, $\hat{Y}$ is known in analytic form:

$$\hat{Y} = Y_n \min\left\{1, 1 - V_g / \left(h\nu - V_n\right)\right\} \; . \tag{304}$$

10.4 Collisional Charging of a Grain

Per unit projected area of a grain, collisions with particles of space density n, mass m, and charge Z (Z = *-1* for electrons) give an effective recombination rate

$$\alpha\left(gr\right) = -n\,\bar{v}\,SZ\,\eta \; , \tag{305}$$

where

$$\bar{v} = \sqrt{8kT / \pi m_e} \tag{306}$$

is the mean particle speed. In this expression, and for other collisional rates involving n below, it is implicit that there is a sum of similar terms over all species in the gas. For electrons S is the sticking probability which we take to be 1 (Spitzer 1948; Watson 1972; Draine 1978). For positively charged nuclei, SZ is the charge transfer efficiency, taken to be Z here. The last factor η, the correction for Coulomb interactions between the grain and the recombining particles of charge Z, is given in terms of

$$\psi = ZV_g / kT_e \tag{307}$$

by

$$\eta = \begin{cases} 1 - \psi & if \quad \psi \leq 0 \\ \exp\left(-\psi\right) & if \quad \psi > 0 \end{cases} \tag{308}$$

Terms for positively charged nuclei are included, but are usually small relative to the contribution from free electrons.

10.5 Grain Potential

The steady state grain potential is determined for each grain species independently by requiring charge balance. Expressed as a balance per unit area this is $\alpha_{gr} = \Gamma_{gr}$. Because of the many dependencies on V_g, this is carried out numerically.

10.6 Grain Drift Velocity

The grain drift velocity is determined by balancing the radiative acceleration due to the direct attenuated radiation field with the drag forces given by equations 1–6 of Draine and Salpeter (1979). The equations are solved numerically for the drift velocity, including interactions with electrons and all ions present in the gas.

10.7 Radiative Heating and Cooling of a Grain

Once the grain potential is known, the rate of radiative heating of the grain per unit projected area is

$$G_{grain}(rad) = \int_0^{\nu_o} Q_{abs}\, 4\pi\, J\, d\nu + \int_{\nu_o}^{\infty} Q_{abs}\, \frac{4\pi J}{h\nu}\, (h\nu - EY)\, d\nu \,. \tag{309}$$

The last term represents the portion of the photon energy that does not heat the grain, but rather passes to the escaping electrons:

$$EY = Y_n \int_{E_o}^{(h\nu - V_n)} E\, f\, p_n\, dE \quad . \tag{310}$$

With the above approximations for f and p_n this is given analytically by

$$EY = 0.5\, Y_n \left[(h\nu - V_n)^2 - [\max(0, V_g)]^2 \right] / (h\nu - V_n) \tag{311}$$

The cooling of a grain by radiative losses, per unit projected area, is given by

$$\Lambda_{grain}(rad) = \int_0^{\infty} Q_{abs}\; 4\pi\, B_\nu (T_g)\, d\nu \tag{312}$$

where $B_\nu(T_g)$ is the Planck function for the grain temperature.

10.8 Collisional Heating of a Grain

Collisions with electrons, ions, and neutral particles also heat the grains. Per unit projected area of the grain, this heating rate may be written as

$$G_{grain}(col) = n\, \bar{v}\, S \left(2kT_e \xi - ZV_g \eta + I\eta - 2kT_g\, \eta \right) \quad . \tag{313}$$

The first term corresponds to kinetic energy extracted from the gas. The factor ξ makes adjustment for Coulomb interactions and is given by

$$\xi = \begin{cases} 1 - \psi/2 & if \quad \psi \le 0 \\ (1 + \psi/2)\exp(-\psi) & if \quad \psi > 0 \end{cases} \,. \tag{314}$$

The second term in $G_{grain}(col)$ allows for the change of the particle's energy in the grain potential. In the third term, the product $I\eta$ is the average chemical energy released per impact. Here it is assumed that when impinging ions recombine the ionization energy released is deposited as heat in the grain (there is then no corresponding term for heating the gas in Λ_g below). The last term describes the

effect of thermal evaporation of neutralized ions and thermally accommodated neutral particles (there is no corresponding term for electrons).

In implementing the above processes, *S* for electrons is again the sticking probability. For positively charged nuclei, *S* is the energy transfer efficiency, taken here to be unity (this process should be evaluated consistently with that for charge transfer). For neutral particles of mass *m* striking a grain whose typical atom has mass *M*, the accommodation coefficient $S \approx 2\ m\ M/(m + M)^2$ (Draine 1978).

10.9 Grain Temperature

The equilibrium grain temperature is determined by the balance between cooling (Λ) and heating (*G*) by radiative and collisional processes. For the radiative terms, Q_{abs} averaged over the size distribution is used to obtain a typical temperature for each species.

As a test of the bandwidth of the code, and its behavior in a well-defined limit, tests where computed in which the grains were irradiated by black body radiation in strict thermodynamic equilibrium (i.e., the color and energy density temperatures were equal). Radiation temperatures between 10 K and 10^9 K, the temperature limits to the code, were used. These tests showed that the deduced grain equilibrium temperature was within much better than 1 percent of the blackbody temperature.

10.10 Photoelectric Heating of the Gas

Heating of the gas by photoemission from grains can be an important process in ionized regions (Spitzer 1948; Oliveira and Maciel 1986). For charged grains this heating rate (erg cm^{-3} s^{-1}) is given by

$$G_{gas} = \int_{\nu_o}^{\infty} \kappa_{abs} \frac{4\pi J}{h\nu} \left(EY - V_g \hat{Y} \right) d\nu \, . \qquad (315)$$

The first term describes the energy of the photoelectrons as they leave the surface, balancing the similar term in $G_{grain}(rad)$. The second term compensates for the grain potential, and can be seen to balance the related term in $G_g(col)$ when charge balance holds.

10.11 Collisional Cooling of the Gas

The gas is cooled as the gas particles hit the cooler grain surface. Per unit volume, this cooling rate may be written as

$$\Lambda_{gas} = n\ n(H) \Sigma \overline{v}\ S \left(2kT_e \xi - 2kT_{grain} \eta \right) \quad , \qquad (316)$$

the individual terms consistently balancing the corresponding ones in $G_g(col)$ (see equation 314).

10.12 Grain Sublimation

The code checks that grain survival is likely by comparing the highest grain temperature with the sublimation temperatures. These are taken to be 1400 K for silicates and 1750 K for graphite and are based on the paper by Laor and Draine (1993). These values are stored in the vector ***sublimat*** and initialized in block data

martin. A warning will be printed at the end of the calculation if the grain temperature rises above the sublimation point. A caution will be printed if the temperature rises above 90% of the sublimation point.

10.13 Ionic Recombination on Grain Surfaces

Positive ion recombination on grain surfaces proceeds at a rate $n_{ion} n_H \alpha_{gr}$ where the recombination coefficient is taken from Draine and Sutin (1987; their equation 5.15). For a standard grain size distribution this rate coefficient is $\sim 5.8\times10^{-13}\ T_e^{-0.5}\ cm^3\ s^{-1}$. This process is included for all ions included in the calculation when grains are present, but is not generally important. The rate coefficient is evaluated in routine ***hmole*** and stored as the variable ***gionrc***.

10.14 Grain Variables

ndust The number of grain species. This variable appears in parameter statements throughout the code. Currently ***ndust*** is 20.

lgDustOn This logical variable is true if grains are enabled, and false otherwise. This is the variable to check to determine whether grains exist in the current model.

Dqabs[energy][ndust] Absorption Q for this grain species as a function of energy.

dqscat[energy][ndust] Scattering Q for this grain species as a function of energy.

dston1[ndust] A logical variable that indicates whether this grain species is enabled.

dstab1[energy][ndust] Absorption cross section for this grain species

dstsc1[energy][ndust] Scattering cross section for this grain species.

dstab[ndust] **T**otal absorption cross section for all grain species.

Dstsc[energy] Total scattering cross section for all grain species.

dstq[ndust] The grain charge, in units of number of electrons.

dstpot[ndust] The grain potential, in Rydbergs.

dstdft[ndust] The grain species' drift velocity.

avdft[ndust] Variable used to derive average drift velocity of a grain species.

Dustp[4][ndust] These are parameters describing the grain species, and are set in block data ***martin***. They are defined in Peter Martin's program that computes grain optical parameters. The four elements of the array are the grain density, molecular weight, normalizing abundance, and depletion.

Eev[limcrs][ndust) is an ***limcrs*** long array of energies (in Rydbergs, despite the variable name). ***ndpts*** of these are energies where the grain optical parameters are defined.

Sab[limcrs][ndust] is an ***limcrs*** long array of absorption cross sections for the grain species, at the ***ndpts*** energy points. These are defined as the effective absorption cross section per hydrogen nucleon.

Sse[limcrs][ndust] is an ***limcrs*** long array of scattering cross sections for the grain species, at the ***ndpts*** energy points. These are defined as the effective scattering cross

section per hydrogen nucleon, multiplied by (1-g) where g is the grain asymmetry factor.

Ndpts[ndust] is the number of energies where the grain optical properties are defined, for each species.

Darea[ndust] is the grain surface area (cm^2) per hydrogen nucleon.

Dsize[ndust] is the grain radius (cm) per hydrogen nucleon.

Dwork[ndust] Grain species neutral surface work function in Rydbergs.

Dstfac[ndust] This is the log of the depletion scale factor for each grain species. It is equal to 0 for "normal" abundances, -1 for 1/10th of "normal", etc. This is the first optional number that appears on the **`grains`** command. The number remains the log of the depletion throughout the calculation.

Tedust[ndust] The equilibrium temperature for a grain species.

11 OTHER PHYSICAL PROCESSES

11.1 Overview

This section describes other physics processes that have been incorporated into Cloudy. Some of these are taken from published papers that have described the formalism used by Cloudy in detail. The original papers are cited in the beginning of each section.

11.2 Cosmic Ray Interactions

The implementation of cosmic rays was done in collaboration with Richard Mushotzky. This section is taken from Ferland and Mushotzky (1984).

Synchrotron radio sources are usually modeled in terms of an interaction between a magnetic field and a relativistic gas with a typical energy per electron of a few hundred MeV (see Pacholczyk 1970; Longair 1981). The spectral index of the radio emission for radio-loud active galaxies is usually ~ -0.7, and this suggests that the electrons, which make the dominant contribution to synchrotron emission, have a density (per unit energy interval) given by $n(cr, E) \sim E^{-2.4}$ (Kellerman 1966). The total relativistic electron density is sensitive to the lower bound of the energy distribution, which is typically of order 10–100 MeV, corresponding to relativistic factor of $\gamma \sim 10$–100 (Lee and Holman 1978).

The cosmic ray density used by Cloudy is defined as

$$n(cr) = \int_{E_{\min}}^{E_{\max}} n\left(cr, E\right) dE \qquad (317)$$

with the lower bound set to E_{min} = 5 MeV, corresponding to $\gamma \sim 10$. The density is only weakly sensitive to the upper limit $E_{max} \approx 10$ GeV because of the strong convergence of the electron density function, although uncertainties in the lower energy bound introduce a fundamental uncertainty. Cosmic ray protons should have much smaller affects than the electrons, so the total cosmic ray electron density n(cr) is the only parameter.

The code assumes that the gas is “optically thin” to the energetic electrons. Serious and fundamental uncertainties afflict detailed treatments of the penetration of energetic particles into gas, particularly if magnetic fields are present. In the simplest case penetration is impeded only by ionization and heating losses resulting from two-body collisions. In this case the ability to heat an entire cloud is determined by the range of a particle, or the column density of gas required to stop it (see Rossi 1952). Relativistic electrons have a range that is given to within 15% by (Berger and Seltzer 1965)

$$R_e = 10^{25} \left(\frac{E}{100 \text{ MeV}} \right)^{0.8} \quad \text{cm}^{-2} \qquad (318)$$

for a gas composed of neutral hydrogen. The range of a 100 MeV electron in a fully ionized gas, in which bremsstrahlung and Coulomb losses are more important than ionization, would be some 10 times smaller.

The relativistic particles both heat and ionize the gas. The main concern is for the rate with which energy is transferred to the cold gas (Lea and Holman 1978; Ginzberg and Syrovatskii 1964). In the H^+ zone the main interaction will be with free electrons. Kinetic energy is passed to the cold electrons at a rate

$$G_{cr} = 8.5\times10^{-19}\ n_e\ n(cr) \quad \left(\text{erg cm}^{-3}\ \text{s}^{-1}\right) \tag{319}$$

by direct Coulomb interactions (Jackson 1975; Spitzer 1962; Ginzburg and Syrovatskii 1964; Pacholczyk 1970). Here n_e is the thermal electron density, and the integration is over the electron distribution given above.

In regions where hydrogen is neutral the main interaction between thermal and relativistic gases is through ionization of the cold gas. For large neutral fractions very little of the energy of secondary electrons goes into actually heating the gas (Rossi 1952; Spitzer and Tomasko 1968). Calculations show that secondary electrons have typical energies of ~ 40 eV, and that there is roughly one ionization per 15 eV deposited. Using the Bethe-Bloch approximation (Ginzburg and Syrovatskii 1964) the neutral heating rate is

$$G_{cr} = 3.7\times10^{-20}\ n\left(H^o\right) n(cr) \quad \left(\text{erg cm}^{-3}\ \text{s}^{-1}\right) \tag{320}$$

and the H^o ionization rate is

$$\Gamma = 1.5\times10^{-8}\ n(cr)\, n\left(H^o\right) \quad \left(\text{cm}^{-3}\ \text{s}^{-1}\right)\ . \tag{321}$$

This ionization rate was scaled through Lotz's (1967) curves to include collisional ionization of heavy elements in the calculation of heavy element ionization equilibria.

If cosmic rays are not included, and the hydrogen ground state photoionization rate falls below the galactic background cosmic ray ionization rate, then a comment will be generated warning that the cosmic ray background should perhaps be included. According to Spitzer (1978), the background cosmic ray ionization rate is very uncertain, but of the order of 2×10^{-17} s^{-1} for neutral hydrogen. According to the equations above, this rate corresponds to a cosmic ray density of ~ 2×10^{-9} cm^{-3}, the value used as the "background" cosmic ray density option for the **`cosmic ray`** command.

The discussion above, as well as the code, includes only two-body Coulomb interactions, and *does not* include collective effects, such as those discussed by Scott et al. (1980). Rephaeli (1987) notes that collective effects may not be important in most circumstances.

11.3 Line Radiation Pressure

Line radiation pressure was implemented in Cloudy in collaboration with Moshe Elitzur. The following was written in collaboration with Moshe, and is adopted from Elitzur and Ferland (1986).

11.3.1 Formalism

For radiation intensity I_ν, the standard expression for the radiation pressure per unit frequency, P_ν, is (e.g. Schwarzchild 1965)

$$P_\nu = \frac{1}{c}\int I_\nu \mu^2 \, d\Omega \quad , \tag{322}$$

where μ = cos(θ) and θ is the direction of propagation of the radiation. When the radiation field is isotropic, its pressure and energy density,

$$u_\nu = \frac{1}{c}\int I_\nu \, d\Omega \quad , \tag{323}$$

are related by the familiar expression

$$P_\nu = \frac{1}{3}u_\nu \quad . \tag{324}$$

This relation holds for a rather wide range of circumstances. If the angular distribution of I_ν is expanded in a power series in μ, then only powers higher than the second will lead to violations of equation 324. However, the successive coefficients of this expansion are decreasing approximately like the optical depth (e.g. Schwarzchild 1965, p 40), so deviations from equation 324 will only be proportional to $1/\tau^2$. Hence, when the medium is optically thick at the frequency ν equation 324 is an excellent approximation for the radiation pressure.

The only radiative quantity we need to know in order to calculate the radiation pressure is the angle-averaged flux, J_ν, since

$$u_\nu = \frac{1}{c}4\pi J_\nu \quad . \tag{325}$$

The integrated radiation pressure is then

$$P(\nu) = \frac{4\pi}{3c}\int J_\nu \, d\nu \quad . \tag{326}$$

Introducing the line-width, defined by

$$\Delta\nu = \frac{1}{\overline{J}_{u,l}}\int J_\nu \, d\nu \quad , \tag{327}$$

where

$$\overline{J}_{u,l} = \int J_\nu \, \Phi(\nu)\, d\nu \tag{328}$$

is the integrated mean intensity in the line and Φ(ν) is the normalized line profile $\left[\int \Phi(\nu)\, d\nu = 1\right]$. The quantity $\overline{J}$ is readily available in the escape probability approximation because it is related directly to the source function *S* by

$$\overline{J}_{u,l} = S\left(1 - P_{u,l}\right) \tag{329}$$

where $P_{u,l}$ is the photon escape probability. The line source function *S* is simply $B_\nu(T_{exc})$, the Planck function of the line excitation temperature. The final expression for the pressure due to a line at frequency ν is therefore

$$P(\nu) = \frac{4\pi}{3c}B_\nu\left(T_{exc}\right)\Delta\nu\left(1 - P_{u,l}\right) \quad . \tag{330}$$

Combining equation 330 with equation 147 on page 217 we obtain the final form of the line radiation pressure,

$$P(\nu) = \frac{8\pi h\nu^3}{3c^3} \frac{n_u / g_u}{\left(n_l / g_l - n_u / g_u\right)} \Delta\nu \left(1 - P_{u,l}\right) \quad . \tag{331}$$

In these expressions the line width is given in frequency units. Within the code the line width is given in velocity units, and the line pressure is given as

$$\begin{aligned} P(\nu) &= \frac{8\pi h\nu^4}{3c^4} \frac{n_u / g_u}{\left(n_l / g_l - n_u / g_u\right)} \Delta v \left(1 - P_{u,l}\right) = \frac{8\pi h}{3\lambda^4} \frac{n_u / g_u}{\left(n_l / g_l - n_u / g_u\right)} \Delta v \left(1 - P_{u,l}\right) \\ &= 6.872 \times 10^{-68} \nu^4 \frac{n_u / g_u}{\left(n_l / g_l - n_u / g_u\right)} \Delta v \left(1 - P_{u,l}\right) \quad . \\ &= 5.551 \times 10^{-26} \lambda^{-4} \frac{n_u / g_u}{\left(n_l / g_l - n_u / g_u\right)} \Delta v \left(1 - P_{u,l}\right) \end{aligned} \tag{332}$$

11.3.2 Line width

The line width is a crucial parameter in the calculations since the line radiation pressure is directly proportional to it. For lines with a moderate optical depth (i.e., $\tau \leq 10^4$) the damping wings are optically thin, and the line emission profile is essentially identical to the absorption profile. Then $\Phi(\nu)$ is simply described by the Doppler profile $\pi^{1/2} \exp(-x^2)$, where $x=(\nu-\nu_o)/\Delta\nu_{Dop}$ is the dimensionless frequency shift from line center and $\Delta\nu_{Dop} = (2kT/m)^{1/2}\ \nu_o/c$ is the Doppler width. The line full width is then

$$\Delta\nu = \Delta\nu_{Dop} \times 2\left(\ln\tau\right)^{1/2} \tag{333}$$

for $\tau \gg 1$.

The situation when the line optical depth exceeds ~ 10^4 is much more complicated. This is because scattering in the damping wings becomes significant, and the frequency dependence of the emission profile is not known before the entire radiative transfer problem is solved. In general, it is known that, for Lα (generally the most important source of line radiation pressure) and large optical depths, the line width (in dimensionless units) is

$$x = k\left(a\tau\right)^{1/3} \quad , \tag{334}$$

(Adams 1972; Harrington 1973; Bonilha et al. 1979). In this expression a is the damping constant ($a \approx 4.72 \times 10^{-4}\ t_4^{-1/2}$ for Lα), τ is the line center optical depth, t_4 is the temperature in units of 10^4 K, and k is a number of order unity.

The frequency width required here is the value that will provide a rectangular profile with the same area as the proper integral of the source function. The results of Adams (1972) are adopted, and the resulting expression for the full line width in the case of large optical depths ($\tau \gg 1$) is

$$\Delta\nu = \Delta\nu_{Dop}\ 2.3\ \left(a\tau\right)^{1/3} \tag{335}$$

An important point, evident from the plots provided by Adams for the source function as a function of frequency (his Fig 3), is that the width of the frequency distribution varies very little with position in the slab. This is also evident from the

mean intensity plots of Harrington, as mentioned above, and is a result of the strong coupling between distant regions caused by scattering in the line wings. The expression provided in equation 335 for all locations in the slab, with τ being half the total slab thickness.

11.3.3 Background opacity and thermalization

Background opacity is included in the determination of the level populations using the formalism outlined in the section on line radiative transfer. Its main effect is to lower the line excitation temperature by providing a second "escape" (actually destruction) route for trapped photons. This is assumed to be the only effect background opacity has on radiation pressure. Balmer continuous absorption typically has an optical depth only of order unity, while the line optical depths are many orders of magnitude larger. Absorption in the Balmer continuum can only compete with line scattering in the extreme wings, at frequency shifts exceeding ~ $(a\tau)^{1/2}$, which are much larger than the line width predicted by equation 335.

Collisional de-excitation can also break the assumption of pure scattering because a photon will be lost to the thermal pool before the radiative process can take place. This will happen when the density is high enough that the rate for collisional de-excitation, C_{ul}, exceeds the probability for the effective rate for the transition, $P_{ul}\,A_{ul}$, where P_{ul} is the line escape probability and A_{ul} is the Einstein coefficient. Because at large optical depths P_{ul} is essentially equal to τ^{-1}, the "effectively thin" assumption breaks down when

$$\tau \approx A_{u,l} / C_{u,l} \quad . \tag{336}$$

Once the line optical depth exceeds ~ *A/C*, a "thermalization limit" is encountered, and the assumption of a purely scattering nebula does not apply anymore. Therefore, in evaluating the optical depth for the line width expression (equation 335) the minimum of the actual line optical depth and the one prescribed by *A/C* is used. This is a conservative estimate of the effect of collisions on photon scattering. This is probably the most poorly understood part of the calculation of the line radiation pressure.

11.4 Radiative Acceleration

The radiative acceleration (cm s^{-2}) due to the direct attenuated continuum flux F_ν, for density ρ, is given by

$$a_{rad} = \frac{1}{\rho c}\int F_\nu \bar{\kappa}_\nu \, d\nu + \frac{1}{\rho c}\sum_l F_\nu(l)\kappa_l \gamma_l \, B_{l,u} \quad . \tag{337}$$

Here $\bar{\kappa}_\nu$ is the effective continuous opacity. The radiative acceleration includes the usual photoelectric and free-free absorption in the gas, and Compton and Rayleigh scattering. In addition it includes the term $\kappa_{abs} + (1\text{-}g)\kappa_s$ for the grain contributions if grains are present. The integral is over all energies considered by the code (from λ ≈ 10 m to hν ≈100 MeV).

The second term is a sum is over all transferred lines (typically 10^4 to 10^5 transitions). Here κ_l is the line opacity, $B_{l,n}$ is the Einstein coefficient, and γ_l is the

escape probability in the direction towards the source of ionizing radiation (Ferland and Rees 1988).

11.5 Pressure Laws

11.5.1 Units

Pressure is force per unit area. The unit of force in the cgs system is the dyn, which is 10^{-5} N. The fundamental units of the dyn are g cm s^{-2}. For pressure these are dyn cm^{-2} or gm cm^{-1} s^{-2}.

11.5.2 Ideal gas laws

For a non-relativistic non-degenerate gas the energy density is

$$u = \frac{3}{2} n_{tot} kT_e \tag{338}$$

and the pressure is

$$P_{gas} = n_{tot} kT_e = \frac{2}{3} u \quad \text{dynes cm}^{-2}. \tag{339}$$

n_{tot} is the total particle density (cm^{-3}). For a relativistic non-degenerate gas the energy density is

$$u = 3 n_{tot} kT_e \tag{340}$$

and the pressure is

$$P_{gas} = n_{tot} kT_e = \frac{1}{3} u \ \text{dynes cm}^{-2}. \tag{341}$$

11.5.3 Equation of state

When the pressure is held constant (with the **`constant pressure`** command) the pressure law is given by

$$P(r) = P_{gas}(r_o) + \int a_{rad}\, \rho\, dr = P_{gas}(r) + P_{line}(r) \tag{342}$$

where

$$P_{gas}(r_o) = n_{tot}\, kT \tag{343}$$

is the gas pressure at the illuminated face of the cloud, the total particle density is n_{tot}, and r is the radius of the current position.

11.5.4 Turbulent pressure?

Turbulence can be included as a line broadening mechanism. Its only affect is in modifying the line opacities and resulting optical depths. Turbulence should add a component to the total pressure of

$$P_{turb}(r_o) = \frac{1}{2} \rho\, v_{turb}^2 = 5.8 \times 10^6 \left(\frac{n}{10^5 \text{ cm}^{-3}} \right) \left(\frac{v_{turb}}{1 \text{ km s}^{-1}} \right)^2 \quad \text{cm}^{-3}\ ^\circ\text{K} \tag{344}$$

where n is the density and v_{turb} is the turbulent velocity. Turbulent pressure is not included in the pressure law since it would be either negligible, or so large that it would not be possible to determine the gas pressure.

11.5.5 Ram or dynamic pressure

Pressure associated with energy of bulk motion can be referred to as ram or dynamic pressure. It is given by ρv^2.

11.5.6 Pressure variables and routines

TotalPressure This routine evaluates the sum of the gas and line radiation pressures. This routine *does not* evaluate the force term due to the attenuation and reflection of the incident continuum. The function has a single dummy argument, and returns the total pressure in dynes/cm^2.

PresInit This is the gas pressure at the illuminated face of the cloud.

pgas This is the gas pressure, nkT, with units dynes/cm^2., and is evaluated in routine ***TotalPressure***.

prad This is the line radiation pressure, evaluated as described on page 297. It is also evaluated in ***TotalPressure***.

pinteg The integrated radiative force on the gas is evaluated in routine ***radinc*** and is stored as the variable ***pinteg***. This is kept separate from the local gas pressure since it is really a global quantity, unaffected by changes at the current position.

pnow This is the current sum of gas and local line radiation pressure.

presur This routine obtains the current total pressure, and ratios that with the desired total pressure. This scale factor is then applied to various physical quantities.

perror This is the fractional error allowed in the pressure convergence. It currently is set in a data statement within ***presur***.

presok ***presur*** will set the variable ***presok*** to false if the change in the local conditions was too large, and so capped, and to true if a good final pressure was achieved. The pressure is declared converged by ***presur*** when ***pnow*** (the local pressure) is within ***perror*** of being equal to the sum of ***PresInit*** and ***pinteg***.

PIonte This routine calls ***presur***.

11.6 Wind Geometry

Cloudy will do a simple wind geometry if the **wind** command is specified. The effective acceleration is written as $a_{eff} = a_{rad} - g_{grav}$, where a_{rad} is computed in equation 337 above, and g_{grav} is the inward

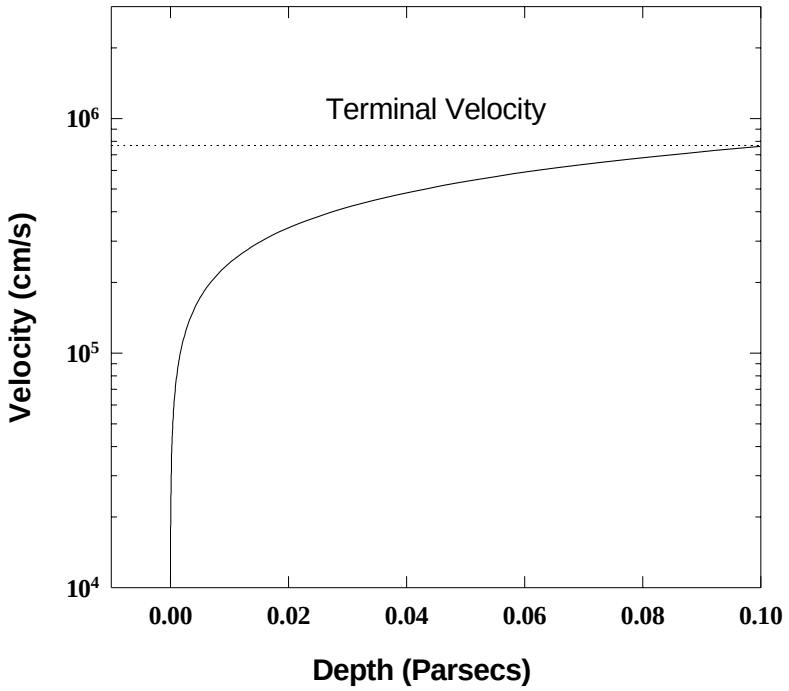

Figure 27 The wind velocity is computed using the input stream shown in one of the test cases in the last section. Parameters were chosen to have a readily computed final velocity. The velocity at the outer edge of the slab is within 1 percent of its expected value. wind

gravitational acceleration due to the central object. The default is one solar mass. The velocity is computed assuming that the acceleration is constant across the zone. In this case the change in the wind velocity *v* between the inner and outer edges of a zone of thickness *dr* will be

$$v^2 - v_o^{\ 2} = 2\, a_{eff}\, dr \qquad (345)$$

where v_o is the velocity at the inner edge. The calculation will stop if the velocity ever falls below zero.

All calculations involving the velocity and density associated with this wind are performed in routine ***presur***. The density at the illuminated face of the cloud is entered with the **hden** command. The density is varied across the model to conserve mass flux (i.e., the product $\rho(r)\, r^2\, v(r)$ is kept constant). Because of this, a filling factor would not make physical sense, and should not be used. Note also that it is usually necessary to set an outer radius when a wind model is computed to stop the calculation from extending to infinity.

A simple Sobolev or large velocity gradient (LVG) approximation is used for line transfer when a wind is computed. In the constant expansion velocity case the effective optical depth is given by;

$$\tau_{l,u}(r) = \alpha_{l,u} \left(n_l - n_u \frac{g_l}{g_u} \right) r \frac{v_{th}}{\max(v_{th}, v_{\exp})} \qquad (346)$$

where *r* is the smaller of the radius or depth and v_{th} and v_{exp} are the thermal and expansion velocities respectively. The choice of the smaller of the radius or depth is not in strict keeping with the Sobolev approximation, but is necessary since calculations often begin at very large radii from the central object. The optical depths would have unphysically large values were this choice not made.

In the case where the code actually solves for the velocity, which is then not constant, the effective optical depth is given by (Castor, Abbott, & Klein 1975)

$$\tau_{l,u}(r) = \alpha_{l,u} \left(n_l - n_u \frac{g_l}{g_u} \right) v_{th} \left| \frac{dv}{dr} \right|^{-1} \qquad (347)$$

where *dv/dr* is the acceleration.

Figure 27 shows a test case in which a wind is driven in the plane parallel electron scattering limit. As can be seen the numerical solution is in excellent agreement with the analytically predicted result.

11.7 Secondary Ionization

11.7.1 Ionization, heating, and cooling

Although the electron velocity distribution is predominantly Maxwellian (Bohm and Aller 1947), a small constituent of non-thermal secondary electrons may be present when high-energy radiation is present. Secondary ionizations by supra-thermal electrons are treated following Xu and McCray (1991). All sources of energetic electrons, including both Auger and primary electrons, are considered in the initial input of high-energy electrons into the gas. The resulting coefficient giving the rate of non-thermal electrons is stored as the variable ***csupra***, which has units s^{-1}.

A typical energy of an electron in the non-thermal shower is ~ 20 eV; this energy is used to evaluate collisional ionization and excitation cross sections. Secondary ionization is included among the general ionization processes considered for all species. The coefficient giving the rate for excitations of Lα is given as ***x12***.

11.7.2 Evaluation of rate of hot electron energy input

The variable ***ipSecIon*** points to the lowest photon energy (100 eV) where a photoelectron can produce secondary ionization. Below this energy photoelectrons are assumed to produce 100% heat with no secondary ionization.

Each of the routines that evaluate photoionization or Comptonization rates records the total energy input by photons with energy greater than this. These are saved with units Rydbergs per photoionization per atom, ε^*_{Ryd}.

11.7.3 Secondary rates per atom

The secondary ionization energy redistribution coefficients are evaluated in routine ***nockon***. Three variables, the heating efficiency ***heatef***, the ionization efficiency ***efionz***, and the efficiency for exciting Lα ***exctef***, are defined. In the following equations ε^*_{Ryd} is the initial energy of the hot photoelectron.

heatef This is a fraction (between 0 and 1) of the energy of the photoelectron that goes into heating the Maxwellian electron bath. The heat actually deposited in the free electrons (Ryd cm^3 s^{-1}) is given by

$$\Lambda_{\rm sec} = \varepsilon^*_{Ryd} \times \mathrm{HEATEF}\,. \qquad (348)$$

efionz This is the number of hydrogen ionizations produced per Rydberg of heat input by suprathermal electrons. The number (s^{-1}) of knock-on secondary ionizations is given by

$$r_{ion} = \mathrm{CSUPRA} = \varepsilon^*_{Ryd} \times \mathrm{EFIONZ}\,, \qquad (349)$$

exctef This is the energy in Rydbergs that goes into Lα excitations. The number (s^{-1}) of excitations of Lα is given by

$$r_{Ly\alpha} = \mathrm{SECLA} = \varepsilon^*_{Ryd} \times \mathrm{EXCTEF} \times 4/3\,, \qquad (350)$$

Table 26 Secondary Ionization Variables

Agent	Ionization	La
Hydrogen	***sechi***	***hlax***
Helium	***seche***	***helax***
Compton	***seccmp***	***scmpla***
Heavies	***secmet***	***smetla***

Table 27 Secondary Ionization Efficiencies

Electron fraction	Secondary Ionization	Heating Efficiency	Lyα Excitations	sum
1.00E-04	3.75E-01	1.11E-01	4.19E-01	9.06E-01
3.16E-04	3.66E-01	1.51E-01	3.99E-01	9.15E-01
1.00E-03	3.51E-01	2.03E-01	3.71E-01	9.25E-01
3.16E-03	3.28E-01	2.73E-01	3.35E-01	9.36E-01
1.00E-02	2.92E-01	3.66E-01	2.87E-01	9.45E-01
3.16E-02	2.39E-01	4.87E-01	2.25E-01	9.51E-01
1.00E-01	1.64E-01	6.40E-01	1.50E-01	9.54E-01
3.16E-01	6.98E-02	8.24E-01	6.50E-02	9.59E-01
1.00E+00	0.00E+00	9.97E-01	0.00E+00	9.97E-01

11.7.4 Total interaction rates

The interaction rates per unit volume are given by the rates per atom (given by the variables in Table 26) and the density of the atom. This results in the total number of secondary interactions per unit volume. This total rate is converted into a rate per target atom by dividing the volume rate by the number of *atoms* per unit volume. The results are the rates (with units s^{-1}) referred to by the variable ***csupra*** (secondary ionization rate) and ***x12*** (secondary rate of excitation of Lyman lines).

11.7.5 Rates during the hydrogen balance solution

The hydrogen ionization balance is performed in routine ***hlevel***. In deep regions of X-Ray ionized clouds the dominant source of secondaries is often inner shell ionization of the heavy elements, especially oxygen. Often secondary ionization is the dominant ionization source of hydrogen, and in this case the secondary ionization rate changes as the electron density changes, during searches for the ionization balance. It would not be computationally expedient to reevaluate all heavy element ionization rates during the search for the hydrogen ionization balance, so, during this search an effective secondary ionization rate, given by a simple scaling law using the current electron fraction, and the secondary rate and electron fraction where it was last evaluated. The effective suprathermal rate is referred to as ***csupeff***.

11.7.6 Molecules and Suprathermal Electrons

The collisional and heating effects of the suprathermal secondary electrons following inner-shell photoionization are treated using standard assumptions (Bergeron and Souffrin 1971; Shull and van Steenberg 1985; Voit 1991).

8 eV of heat is deposited for each H_2 ionization by a cosmic ray (Tielens and Hollenbach 1985). Relative rates are taken from HM89.

The result of this is a secondary ionization rate that must then be multiplied by scale factors that account for the relative collision cross section for each species relative to hydrogen. These are taken from HM89 and TH85.

Secondary electrons also produce a diffuse background of electronic H_2 lines that can photodissociate most molecules. This is treated using the scaling rule of Gredel, Lepp, and Dalgarno (1987) and Gredel et al. (1989).

11.8 Eddington Limit

The Eddington limit is given by

$$L_{Edd} = \frac{4\pi GcM}{\kappa} = 1.45\times 10^{38}\,\frac{M}{M_o}\,\frac{\kappa_T}{\kappa}\ \text{erg s}^{-1} \qquad (351)$$

where κ_T is the Thomson opacity and κ is the actual gas opacity (generally several orders of magnitude above Thomson).

11.9 Jeans Length and Mass

The Jeans length and mass are computed for each zone in the calculation. The smallest computed Jeans length and mass are saved, and a note is printed at the end of the calculation if the computed structure is Jeans unstable.

The expression for the Jeans length is

$$\lambda_J = \left(\frac{\pi k T}{\mu m_p G \rho} \right)^{1/2} = 6.257 \times 10^7 \left(\frac{T}{\mu \rho} \right)^{1/2} \quad (\mathrm{cm}) \tag{352}$$

where μ is the mean mass per particle

$$\mu = \frac{\sum n_i m_i}{\sum n_i} \quad (\mathrm{gm}) \tag{353}$$

of the.

The Jeans mass is then given by

$$M_J = \frac{4\pi}{3} \rho \left(\frac{\lambda_J}{2} \right)^3 \quad (\mathrm{gm}) \tag{354}$$

where the mass is that of a sphere with radius $\lambda_J /2$.

The minimum Jeans mass is evaluated in routine tauinc as the calculation progresses. The code will generate a comment if the computed structure is Jeans unstable.

11.10 Luminosity Distance

The luminosity distance D_L is given by equation 355.

$$D_L = \begin{cases} \dfrac{cz}{H_o}(1 + z/2) & q_o = 0 \\ \dfrac{c}{H_o q_o^2} \left\{ q_o z + (q_o - 1) \left[(2 q_o z + 1)^{1/2} - 1 \right] \right\} & q_o > 0 \\ \dfrac{2c}{H_o} \left[1 + z - (1+z)^{1/2} \right] & q_o = 1/2 \end{cases} \tag{355}$$

For q_o=*1/2* and H_o = 70 km / s / Mpc the luminosity distance is

$$D_L = 2.643 \times 10^{26} \left[1 + z - (1+z)^{1/2} \right] \ \mathrm{cm} \tag{356}$$

The proper distance D_P is given by $D_P = D_L (1+z)$.

Liske (2000) provides expressions giving the cosmological distance and redshift between any two objects.

12 OTHER DETAILS

12.1 Overview

This section largely outlines internal details of code variables, and how these relate to overall quantities. These are described only after the relevant portion of the code has become fairly mature, and not likely to undergo further major revision.

12.2 Overall Structure

This section outlines the flow control in the higher levels of the code.

12.2.1 The main program

When used as a stand-alone program, control passes to program ***main*** contained in **`maincl.c`**, which initializes the code by calling ***cdInit***. It then reads the input stream (from standard input) and passes the line images into the code by calling ***cdRead***. The main routine calls ***cdDrive*** to compute the model after all lines have been read. It then checks whether any problems occurred during the calculation (by calling ***cdNwcns***), prints a brief summary of what happened, and then stops. The organization is shown in Figure 28.

There actually is no difference in the way the stand-alone and subroutine versions of the code receive commands. The main routine simply reads standard input and passes the command string into the code through routine ***cdRead***. The one difference is that the main routine includes logic to identify whether the input stream is the edited header of a previous calculation.

12.2.2 Routine cdDrive

cdDrive is called to execute the code, both in the stand-alone and main versions. ***cdDrive*** decides whether to compute a single model or try to optimize a model by varying a set of parameters by checking whether the keywork **`vary`** occurred on a command line. If the keyword did not apprear then it simply calls routine ***cloudy*** to compute a single model. If the keyword **`vary`** occurred then ***cdDrive*** calls ***DoOptimize***, the routine to optimize parameters to match a set of observations. Otherwise it simply computes a single model.

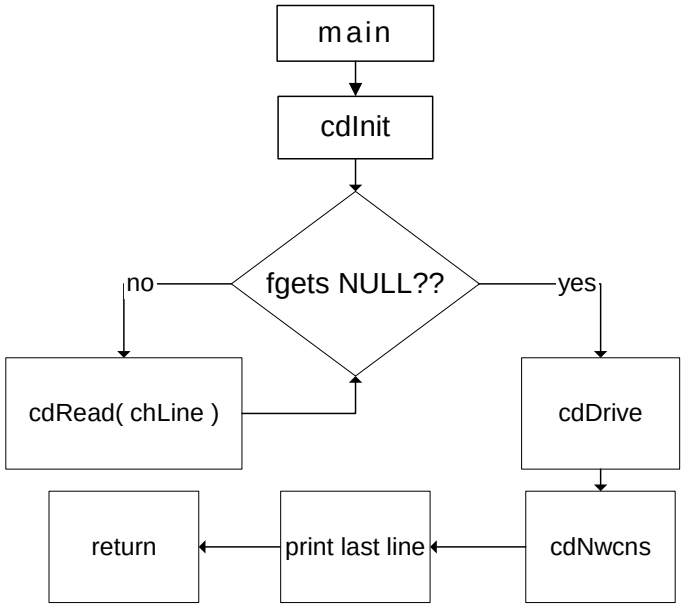

Figure 28 This shows the structure of the main program.

12.2.3 Routine Cloudy

Most of the actual work performed in the computation of a model is done is the main subroutine Cloudy (Figure 29). This routine controls the zone and iteration variables ***nzone*** and ***iter***.

At its outermost level the routine controls the number of

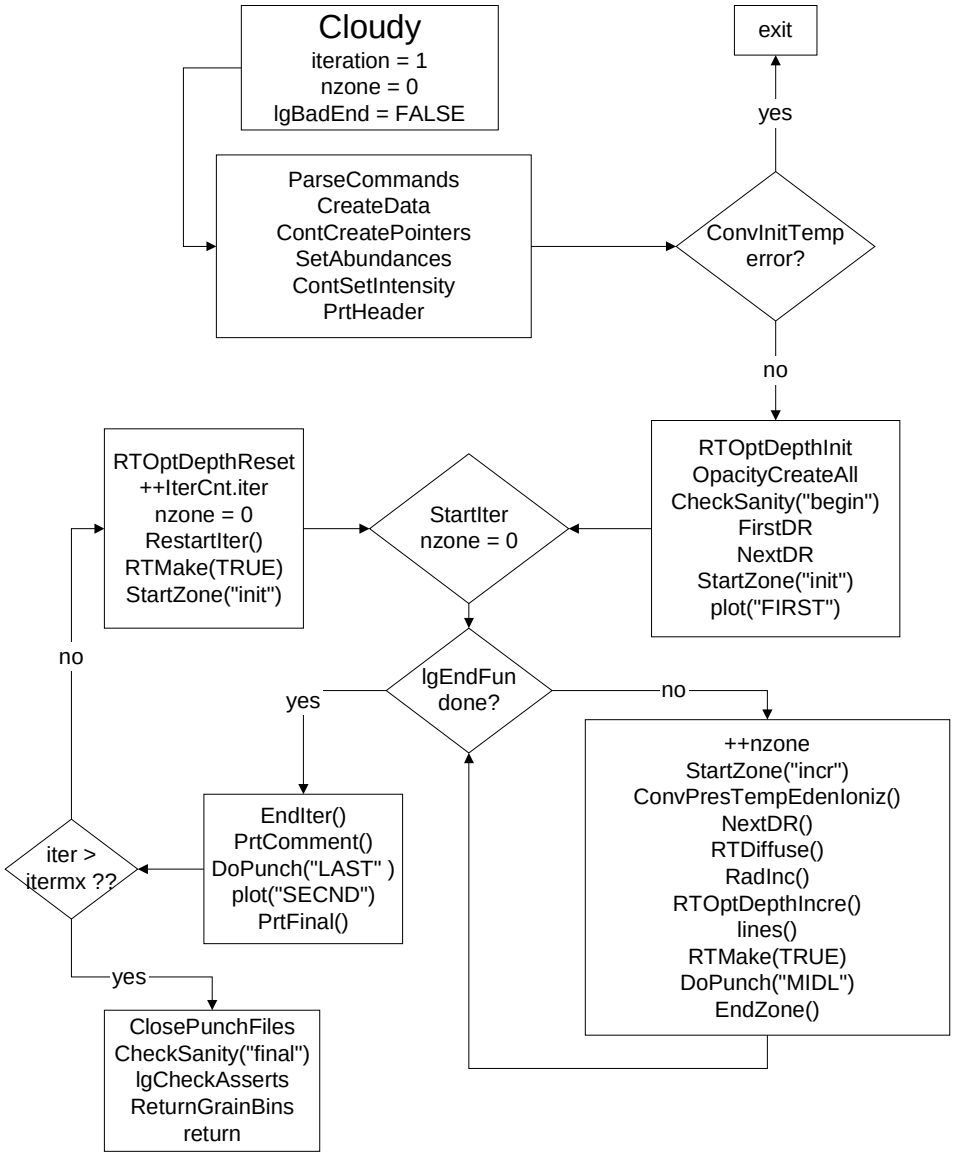

Figure 29 This figure shows the structure of subroutine Cloudy.

iterations, determining when the model is converged. Within this loop is an inner loop that determines whether a particular iteration is complete. This inner loop controls the integration over zones and checks stopping criteria to determine whether the structure is complete.

12.2.4 ConvPresTempEdenIoniz converge pressure

ConvPresTempEdenIoniz, shown in Figure **30**, is the routine that converges the local pressure, or specification of the gas density. Its major loop calls routine ***PresChng***, which determines what the local density / pressure should be, and sets the variable ***conv.lgConvPres*** to true if the current conditions are correct. Next routine ***ConvTempEdenIoniz*** is called to deterine the local temperature, electron density, and level of ionization at the new density. ***ConvPresTempEdenIoniz*** loops until the pressure is declared converged by the flag ***conv.lgConvPres***, as set in routine ***PresChng***.

As the top-level routine, this is the one that will announce a convergence failure if one should occur. After the attempt at converging the pressure, temperature, electron density, and ionization is complete, the status of a series of flags is checked and ***ConvFail*** called if convergence was not achieved. This is the routine that will actually print an error message if appropriate.

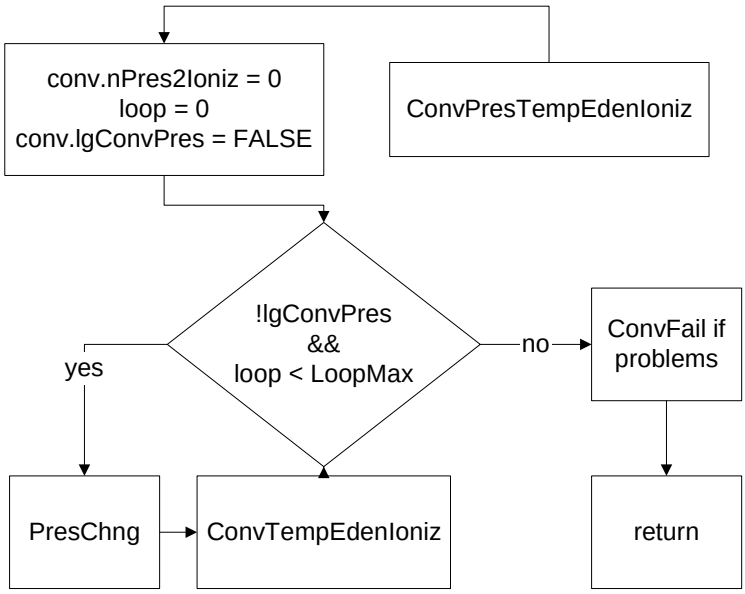

Figure 30 This figure shows the structure of routine ConvPresTempEdenIoniz..

12.2.5 ConvTempEdenIoniz – converge temperature

ConvTempEdenIoniz is the routine that calls ***ConvEdenIoniz*** to converge the electron density and ionization, and siimulatneously determines the electron temperature by balancing heating and cooling. An overview is shown in Figure **31**. Ionte totally controls the value of ***lgDoPhoto***. When ***lgDoPhoto*** is true the code completely reevaluates all opacities and photoionization rates. When false the rates are left at previous values, safe for second iterations.

ConvTempEdenIoniz returns when the heating and cooling match (the variable ***conv.lgConvTemp l*** is set TRUE), or a temperature failure occurs (***tfail*** is set true). The Boltzmann factors are evaluated next in routine ***boltgn***.

A great deal of the code within ***ConvTempEdenIoniz*** deals with idenfitying temperature osciallations or problems in obtaining temperature convergence. The upshot of this is an estimate of the partial derivative of the difference in heating and cooling with respect to temperature.

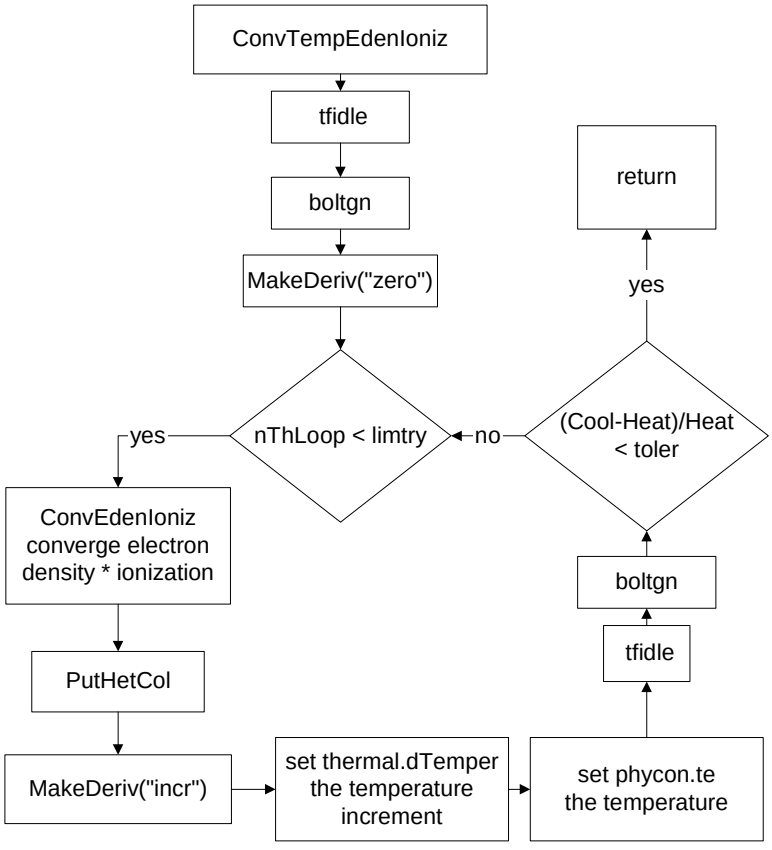

Figure 31 This figure shows the structure of routine ConvTempEdenIoniz.

Many tricks are used to establish this estimate. Routine ***MakeDeriv*** can recall previous values of the heating and cooling and make numerical estimates of their change with respect to temperature. Analystiical estimates are also made from the functional form of various heating and cooling constituents.

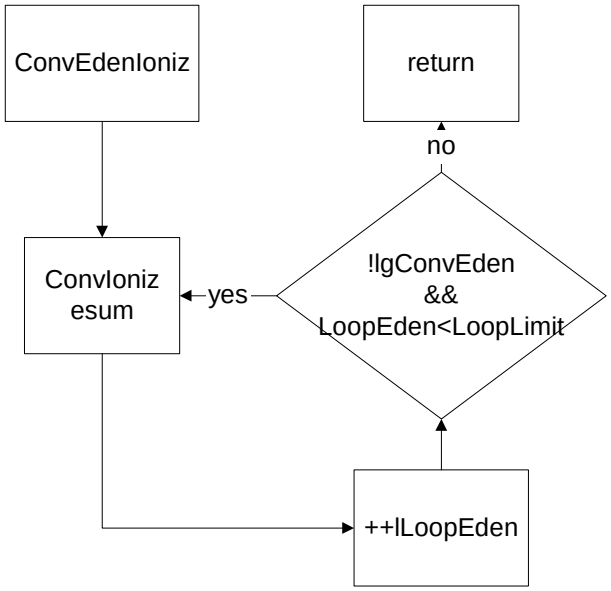

Figure 32 This figure shows the structure of routine ***ConvEdenIoniz***.

12.2.6 ConvEdenIon – converge the electron density

The electron density is actually converged by routine ***ConvEdenIon***, called by ***ConvTempEdenIon*** as described above. The structure of the routine is shown in Fig 32

12.2.7 Line radiative transfer routines

Figure 33 shows the series of routines that are called to evaluate line radiative transfer.

12.3 Geometry

This section defines the internal variables used to describe the geometry. The geometry is always spherical, but can be made effectively plane parallel by making the inner radius of the cloud much larger than its thickness.

Most variables having to do with the geometry members of the structure *radius*, contained in *radius.h*, and are set and incremented in routine ***StartZone***. The following gives the variable name and a brief description of its intentions. Variables are contained within the structure radius.

rinner, $\mathbf{r_o}$ This is the separation between the center of symmetry (i.e., the center of the central object) and the inner edge of the cloud. It remains constant throughout the calculation. If an inner radius is not

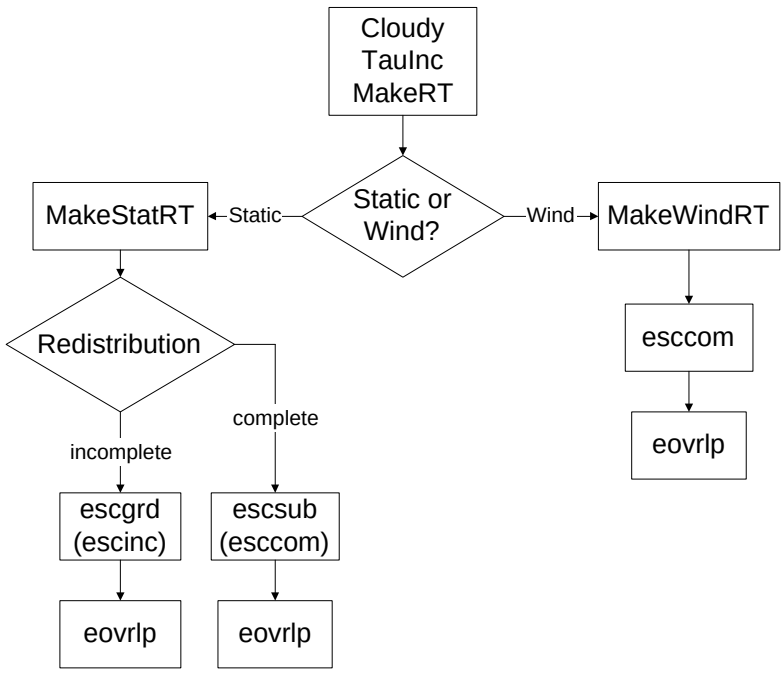

Figure 33 This figure shows the structure of the radiative transfer routines. radtrn

specified then it is given the default value of 10^{25} cm. This will usually result in a plane parallel geometry.

drad, δ**r** This is the thickness of the current zone. Note that the zone size changes continuously throughout the calculation. Upper or lower limits to ***drad*** can be set with the **drmax** and **drmin** commands, described in Part I.

Radius, **r** This is the distance between the center of symmetry and the *outer* edge of the current zone. For the first zone, ***radius*** has the value ***rinner + drad***.

depth, Δ**r** This is the distance between the inner edge of the cloud and the *outer* edge of the current zone. For the first zone, ***depth*** has the value ***drad***.

A problem can arise under certain extreme circumstances. The depth variable ***depth*** must be increased for every zone, by adding the zone thickness ***drad***. Both variables are double precision. If the radio ***drad/depth*** falls below ~ 10^{-14} then the depth cannot be updated on most machines. The problem is that the sum ***depth*** + ***drad*** will be equal to ***depth*** because of numerical underflow. If this occurs (i.e., the zone thickness ***drad*** falls below ***depth*** / 10^{14}) the code will stop, with the comment than the zone thickness is too small relative to the depth. There is no obvious solution to this problem.

drNext This will be the thickness of the next zone. The thickness of the zones is adjusted continuously during a calculation. Adaptive logic is used to ensure that the zones are large enough to be economical, but small enough to follow changes in the physical conditions across the nebula. This choice of the next zone thickness is done in routine ***NextDR***. The logic behind the choice of the zone thickness can be followed with either the **trace dr** or **punch dr** commands.

router[iteration] This is the limit to the outer radius of the structure, as set before the calculation begins. The default value is effectively infinite, actually 10^{30} cm.

r1r0sq This is the sphericity ratio

$$\mathrm{R1R0SQ} = \left[\frac{\text{outer radius of zone}}{\text{radius of face}}\right]^2 = \left(\frac{\mathrm{RADIUS}}{\mathrm{RINNER}}\right)^2 \qquad (357)$$

dReff This is the effective radius, $\delta r_{eff} = \delta r \times f(r)$ where f(r) is the filling factor.

dVeff This is the effective volume relative to the inner radius. The units of ***dVeff*** are cm, and it is equal to ***dReff*** if the geometry is plane parallel.

$$\mathrm{dVeff} = \left(\frac{radius - dRad/2}{rinner}\right)\left(\frac{\min\left(radius - dRad/2, \mathrm{cylind}\right)}{rinner}\right) dRad \times f(r) \qquad (358)$$

Structure ***fourpi*** has the following:

pirsq This is the log of the inner area ($4\pi r_o^2$).

lgFourPi – set true if quantities like line intensities are into 4π sr.

12.4 Physical Conditions

12.4.1 Densities

These are contained in structure ***phycon***.

xMassDensity The gas mass density in gm cm^{-3}.

pden This is the number of particles per cubic centimeter. It is evaluated in ***TotalPressure***.

wmole This is a quantity related to the mean molecular weight, the mean AMU per particle. It is evaluated in ***TotalPressure***.

$$\mathrm{w}mole = \frac{\sum n_i m_i}{n_{tot}} \tag{359}$$

With these definitions the density ***densty*** (gm cm^{-3}) is the product of ***pden*** and ***wmole***.

TotalNuclei – total number of nuclei

The following are contained in structure *phycon*.

eden This is the electron density, as evaluated in routine ***esum***. ***eden*** is also controlled by other parts of the code, which allow it to change only gradually while looking for a new solution.

EdenTrue This is the correct electron density, and is evaluated in ***esum***. The electron density has converged when ***EdenTrue*** and ***eden*** are within ***EdenError*** of one another. ***EdenError*** is set in the large block data to 0.01. This variable is the sole member of the common block of the same name.

edensqte This is the ratio

$$edensqte = \left(n_e + n_H 10^{-4}\right) T_e^{-0.5} \tag{360}$$

used in many collision rate equations across the code. It is evaluated in routine ***tfidle***. The second term in parenthesis approximately accounts for neutral collisions.

cdsqte This is the ratio

$$cdsqte = edsqte \times 8.629 \times 10^{-6} = \left(n_e + n_H 10^{-4}\right) T_e^{-0.5} 8.629 \times 10^{-6} \tag{361}$$

used in many collision rate equations across the code. It is evaluated in routine ***tfidle***.

12.4.2 Temperatures

These are all contained in structure ***phycon***.

te This is the local electron temperature.

tlast is the final temperature of the last computed zone. It is only meaningful for the second or greater zone.

alogte, ***alogete*** These are the base 10 and natural logs of the electron temperature. The array ***telogn*** contains powers of the base 10 log of the temperature.

telogn[i] This is a vector dimensioned 7 long. The nth member of the array contains log(T$_e$)^n.

alogete is the natural log of the temperature.

Routine ***StartZone*** will propose a temperature for the next zone, the variable ***TeProp***, if the model is a constant density model. Routine ***tfidle*** sets all ancillary variables related to the temperature, such as alogte.

12.4.3 Structure

The *struc* structure. This saves information about the structure of the model. It has several elements, each containing a saved quantity for a zone. These vectors are dimensioned ***nzlim*** long. ***NZLIM*** is currently set to 2000, so only the first 2000 zones can be saved. This is the only thing that sets the limit to the number of zones whose information can be saved. Increase ***NZLIM*** if more are needed.

ednstr The electron density of each zone is saved in this vector.

hiistr The H^+ density of each zone is saved in this vector.

histr The H^o density of each zone is saved in this vector.

heatsrt This is the total heating.

pdenstr This save the total number of particles per cubic centimeter.

radstr The effective thickness ***dReff*** (cm) of each zone is saved in this vector. This includes a filling factor if one was specified.

testr The temperature structure of the nebula is saved in this vector.

volstr The volume ***dVeff*** (cm^3) of each zone is saved in this vector. This includes a filling factor if one was specified.

12.5 Zones and Iterations

iteration This global variable is the counter for the current iteration. It is set to one at the start of the first iteration, and is incremented in routine Cloudy after the last printout, just after the limiting optical depths are updated by calling routine ***RTOptDepthReset***. The calculation stops when ***iteration*** is greater than ***itermx*** *after* the iteration is complete, but before the counter is incremented.

ITRDIM This is the limit to the total number of iterations that can possibly be performed. It is used to declare the dimension of the vectors that store iteration information. It currently is set to 20.

itermx This is the limit to the number of iterations to be performed and is set by the user. ***itermx*** is part of the structure ***IterCnt***. ***itermx*** is initialized to 0 so that the code normally stops after the first iteration. The value of ***itermx*** can be changed with the **`iterate`** command. ***itermx*** is set equal to the number entered on the command *minus one*. This is so that "**`iterate 1`**" will cause the code to stop after a single iteration (***iteration*** is equal to 1 at the end of the first iteration, and the code will only stop if ***iteration*** is greater than ***itermx*** after the iteration is complete).

nzone This is a global variable and gives the current zone number. It is equal to one for the first zone. ***nzone*** is set and incremented in routine Cloudy. ***nzone*** is equal to zero during the search for the initial conditions, on all iterations. After the search has identified a solution the conditions in the first zone are computed with ***nzone*** set to unity.

nend[I] This is the limit to the number of zones in the current (i^{th}) iteration and is part of the structure *ZoneCnt*. It is a vector of dimension 20 (as set by ***ITRDIM***). Individual elements of the vector are set with the **`stop zone`** command. The current iteration stops when ***nzone*** is greater than or equal to ***nend[iteration***].

lgLastIt This logical variable indicates whether (true) or not this is the last iteration. It is controlled by routine ***startr*** and is set true if ***iter*** is greater than ***itermx***, and false otherwise.

12.6 Search phase?

The logic used during the search for the initial conditions at the illuminated face of the cloud is quite different from that used when going from zone to zone across the cloud. Usually no good estimate of the initial conditions exists, but within the cloud conditions do not vary by much from zone to zone. One way to check whether the code has a valid estimate of the physical conditions, or whether the first step in the initial search for parameters is taking place, is to check the status of the variable ***conv.lgSearch***. The initial search is underway if this variable is true. Another is to check whether ***nzone*** is greater than 0.

Some quantities are totally unknown while the various routines are being called for the very first time during a calculation. The variable *nPres2Ioniz*, part of *conv*, is zero before the ionization has been determined the first time, since it counts the number of times the pressure routine has called the ionization routine.

12.7 Composition variables

All variables that hold information are contained in the structure *abundances*, defined in the header file *abundances.h*.

Routine ***SetAbundances*** is called by routine ***cloudy*** after all commands have been entered. This routine sets the final abundances to be used in the first zone of the calculation. The following variables are used.

Routine ***SetAbundances*** first modifies the contents of *solar* by the scale factors. The helium abundance is altered by both *depset* and *scalem*, while all heavier elements are modified by these and *dmetal* as well. Then *xIonFracs[0][nelem]* is set to the density (cm^{-3}) of each element, the product *hden* and *solar[nelem]*. This is the total abundance of that element, in all stages of ionization and molecular forms.

The initial chemical composition is printed by routine ***PrintElem***, which is called by ***SetAbundances***.

Default abundances are stored in several arrays. Solar abundances are stored in the array *SolarSave[nelem]*, where *nelem* is the atomic number on the C scale. Other mixtures, such as ISM, HII Region, etc, are also entered in this structure, in other arrays. Each array is dimensioned *LIMELM* (currently 30), the number of elements included in the code.

When the code is initialized the contents of *SolarSave* are copied to the array *solar*, which will contain the initial abundance mix for the current calculation. Gas phase depletion factors, used to modify the final abundance, are stored in the array *depset[nelem]* and are set to unity in routine ***zero*** when the calculation is initialized. The final contents of *solar* will be absolute abundances by number, on a scale with hydrogen at unity.

When an element with atomic number *nelem+1* is turned off, the logical variable ***lgElmtOn[nelem]*** is set to false.

ScaleMetals This is the scale factor entered with the **metals** command when a number but no keyword appears on the line. This multiplies the abundances of all elements heavier than helium. It has no effect on hydrogen or helium.

depset If the **metals** command is entered and no numbers appear, but the keyword **deplete** occurs instead, then this array of scale factors is set to the contents of the array *deplon*.

ScaleElement This is an array of *LIMELM* scale factors, and is set when the **element scale** command is entered.

lgAbnSolar This logical variable is false if the default abundances have been altered, and is true if they are left at the default solar mixture. It is used for sanity checks within the code.

xIonFracs This is a two dimensional vector containing information about gas phase ionic abundances. *xIonFracs[0][nelem]* is the gas-phase density (cm^{-3}) of all stages of ionization of element *nelem*. *xIonFracs[0][nelem]* is the gas-phase density of the nth ionization stage of that element, where the atom is 1. Unlike the previous variables, which are all in the structure *abundances*, *xIonFracs* is in the header file *xionfracs.h* and not part of a structure.

12.8 Covering factors

Two covering factors enter into the calculations. These are referred to as the geometric covering factor, and the radiative transfer covering factor. All covering factors are part of the structure *sphere*, defined in the header file *sphere.h*.

12.8.1 Geometric covering factor

This covering factor linearly affects the luminosity of emission lines. The nebula intercepts a fraction $\Omega_{geo}/4\pi$ of the luminosity radiated by the central object. Within the code the geometric covering factor is referred to by the variable *covgeo*.

The code actually works in units of intensity radiated by a unit area of illuminated face of the cloud to avoid exponential range problems with IEEE machines. If the predicted intensity of a line (erg s^{-1} cm^{-2}) is given by I then the line luminosity will be

$$L = 4\pi \; r_{inner}^2 \frac{\Omega_{geo}}{4\pi} I \qquad (362)$$

where r_{inner} is the inner radius.

The default value of the geometric covering factor is unity, and it can be changed with the **covering factor** and **sphere** commands.

12.8.2 Radiative transfer covering factor

The radiative transfer covering factor has only second order effects on the intensity of emission lines. This is the covering factor which takes into account interactions with diffuse fields produced on the symmetric far side of the nebula. Within the code it is referred to by the variable *covrt*.

The default value of the radiative transfer covering factor is zero, appropriate for an open geometry. For a closed geometry it is set to unity. The radiative transfer covering factor only affects the model through the diffuse fields. For a closed geometry all radiation is included in the outward beam, and for an open geometry

only half. This covering factor has no effects on the calculations, other than the amount of diffuse fields transferred outward. Physically for an open geometry the fraction of radiation escaping in the inward direction is then lost to the system. In an open geometry the nebula is symmetric, and escaping radiation is exactly matched by radiation impinging from the far side of the geometry.

13 GLOSSARY OF SYMBOLS

As far as possible, the notation used by HAZY follows standard texts (Osterbrock 1989; Mihalas 1978). This is a summary of some of the symbols used. Page references to Part II of HAZY or the numerical quantity are listed in the third column of this glossary.

The fundamental constants now used by the code are from a variety of revisions of the basic data, some dating back to the 1970's. An effort is now underway to convert the constants to the 1986 CODATA recommended values (see http://physics.nist.gov/PhysRefData/codata86/codata86.html).

Symbol	Description	Units	Notes
a	Stefan radiation density	erg cm^{-3} K^{-4}	7.56464×10^{-15}
a	damping constant	-	page 218
a_o	Bohr radius	cm	0.5291775×10^{-8}
a_{rad}	radiative acceleration	cm s^{-2}	page 297
A_{ul}	radiative rate from level *u* to *l*	s^{-1}	
b_n	departure coefficient	-	page 231
B	magnetic field	esu	
B_ν	Planck function	erg cm^{-2} s^{-1} Hz^{-1} sr^{-1}	
c	speed of light	cm s^{-1}	2.997925×10^{10}
C	collisional rate	s^{-1}	
C_{ul}	line collision rate	s^{-1}	
D_{ul}	line destruction probability	-	page 219
f	oscillator strength		
f(r)	filling factor	-	
f_ν F_ν	flux density	erg cm^{-2} s^{-1} Hz^{-1}	
g	grain asymmetry factor	-	page 289
g_i	statistical weight	-	
g_{III}	T aver free-free gaunt factor	-	
G	energy gains	heating	erg cm^{-3} s^{-1}
I	integrated intensity	erg s^{-1} sr^{-1} Hz^{-1}	
I_n	ionization potential of level n	erg; Ryd	
I_ν	intensity	erg s^{-1} sr^{-1} Hz^{-1}	
h	Planck's constant	erg s	6.62620×10^{-27}
J	integrated mean intensity	erg s^{-1} sr^{-1}	
J_ν	mean intensity	erg s^{-1} sr^{-1} Hz^{-1}	
k	Boltzmann constant	eV deg^{-1}	8.6171×10^{-5}
k	Boltzmann constant	erg deg^{-1}	1.38062×10^{-16}
$L_\odot$	luminosity of sun	erg s^{-1}	3.826×10^{33}
m_A	mass of atom A	gm	
m_{AMU}	atomic mass unit	gm	1.6605402×10^{-24}
m_e	electron mass	gm	9.10956×10^{-28}
$m_e c^2$	electron energy	Ryd	3.75584×10^{4}

m_p	proton mass	gm	1.6726231×10^{-24}
M_J	Jeans' mass	gm	page 306
$M_\odot$	mass of the sun	gm	1.989×10^{33}
$M_\oplus$	mass of the Earth	gm	5.977×10^{27}
n_e	electron density	cm^{-3}	
n_j	population of level j	cm^{-3}	
n_p	proton density	cm^{-3}	
n(H)	total H density, all forms	cm^{-3}	
n(x)	density of species x	cm^{-3}	
n(cr)	cosmic ray density	cm^{-3}	page 296
n	atom's level		
N(x)	column density of species x	cm^{-2}	
N(H)	total H col den, all forms	cm^{-2}	
N_{eff}	effective H column density	cm^{-2}	
$P^*(x)$	LTE relative population	cm^3	page 231
P_{gas}	gas pressure	dyn cm^{-2}	page 301
P_{lines}	line radiation pressure	dyn cm^{-2}	page 301
P_{tot}	total pressure	dyn cm^{-2}	page 301
P_{ul}	line escape probability	-	page 219
$P_{\tau x}(n)$	continuum escape prob	-	
pc	parsec	cm	3.085678×10^{18}
q_{ij}	line collisional rate coefficient	$cm^3\ s^{-1}$	
q_n	collisional rate coefficient	$cm^3\ s^{-1}$	
q_e	electron charge	esu	4.80325×10^{-10}
Q_{abs}	grain absorption efficiency	-	page 289
Q(H)	hydrogen ionizing photons	s^{-1}	
r	radius	cm	
$r_{l,u}$	rate	s^{-1}	
r_o	inner radius	cm	
R	total to selective extinction	-	
R_H	Rydberg unit for H	-	page 206
R_∞	Rydberg unit for inf mass	-	page 206
R_{AU}	radius of Earth's orbit	cm	1.4959×10^{13}
$R_\oplus$	radius of the Earth	cm	6.378×10^{18}
$R_\odot$	radius of the sun	cm	6.9599×10^{10}
T_e	electron temperature	cm^{-3}	
$T_{eff}(\odot)$	Sun's effective temperature	K	5770
T_{exc}	excitation temperature	K	page 228
T_{color}	color temperature	K	
T_{low}	lowest temp allowed	K	2.8 K
T_u	energy density temperature	K	page 238
u	energy density	erg cm^{-3}	

U_g	grain potential	volt	page 292
v	velocity (mean or projected)	cm s^{-1}	
$\bar{v}$	mean particle speed	cm s^{-1}	page 291
v_{Dop}	Doppler velocity	cm s^{-1}	page 215
v_{exp}	expansion velocity	cm s^{-1}	
v_{th}	thermal velocity	cm s^{-1}	page 215
v_{turb}	turbulent velocity	cm s^{-1}	page 215
V_g	grain potential	eV	page 292
V_n	grain work function	eV	page 292
W	geometric dilution factor	-	
x	relative shift from line center	-	page 214
X_c	continuous to total opacity	-	page 218
$\hat{Y}$	grain photoelectric yield	-	
z	redshift	-	
Z	nuclear charge	-	
$\alpha(n, T)$	recombination coefficient	cm^3 s^{-1}	page 232
$\overline{\alpha}(n,T)$	effec recomb coefficient	cm^3 s^{-1}	page 209
α_ν	continuous abs cross section	cm^2	
α_{lu}	line absorption cross section	cm^2	page 214
β	recombination cooling coef	cm^3 s^{-1}	page 234
η_ν	photon occupation number	-	page 237
δr	zone thickness	cm	
Δr	depth into cloud	cm	
$\gamma_{u,l}$	cont pumping probability		page 220
Γ_n	photoionization rate	s^{-1}	page 237
Γ	reciprocal lifetime of up level	s^{-1}	page 218
Γ_{OTS}	OTS photoionization rate	s^{-1}	page 210
κ	absorption opacity	cm^{-1}	
κ_{lu}	line absorption opacity	cm^{-1}	
κ_s	continuous scattering opacity	cm^{-1}	
κ_ν	continuous absorption opacity	cm^{-1}	
λ_J	Jeans' length	cm	page 306
Λ	energy loss, cooling	erg cm^{-3} s^{-1}	
μ	mean molecular weight	-	page 306
Ω	energy specific collision strength		page 222
Ω	shell coverage	sr	
$\Omega / 4\pi$	covering factor	-	
$\Phi(H)$	flux of ionizing photons	cm^{-2} s^{-1}	
φ_ν	photon flux density	cm^{-2} s^{-1} Ryd^{-1}	
φ_{OTS}	flux of OTS photons	cm^{-2} s^{-1}	page 210
ρ	mass density	gm cm^{-3}	
πa_o^2	area of first Bohr orbit	cm^2	87.9737×10^{-18}

σ_T	Thomson cross section	cm^2	6.6524×10^{-25}
σ_ν	scattering cross section	cm^2	
σ_{Ray}	Rayleigh scat cross section	cm^2	page 212
Σ	projected grain area	cm^2	page 289
τ	optical depth	-	
τ_{abs}	absorption optical depth	-	
τ_{scat}	scattering optical depth	-	
$\tau_{u,l}$	line optical depth	-	
Υ	thermal averaged collision strength		page 222
ν	frequency	Hz	
ν_{Ryd}	frequency	Ryd	
$\delta\nu$	line width	Hz	
$\delta\nu_{Dop}$	Doppler width	Hz	
χ_n	$h\nu/kT$	-	

14 REFERENCES

Abbott, D. C. 1982, ApJ, 259, 282
Adams, T. 1972, ApJ, 174, 439
Aldrovandi, S., & Pequignot, D. 1972, A&A, 17, 88
Aldrovandi, S., & Pequignot, D. 1974, Revista Brasileira de Fisica, 4, 491
Ali, B., Blum, R. D., Bumgardner, T. E., Cranmer, S. R., Ferland, G. J., Haefner, R. I., & Tiede, G. P. 1991, PASP, 103, 1182
Allen, C. W. 1976, *Astrophysical Quantities*, Third Edition (London: Athlone Press).
Aller, L. H. 1984, in *Physics of Thermal Gaseous Nebulae*, (Dordrecht: Reidel).
Aller, L. H., & Czyzak, S. J. 1983, ApJS, 51, 211.
Anderson, H., Ballance, C.P., Badnell, N.R., & Summers, H.P., 2000, J Phys B, 33, 1255Arimoto, N., & Yoshii, Y. 1987, A&A, 173, 23
Armour, Mary-Helen, Ballantyne, D.R., Ferland, G.J., Karr, J., & Martin, P.G., 1999, PASP 111, 1251-1257
Arnaud, M., & Raymond, J. 1992, ApJ, 398, 394
Arnaud, M., & Rothenflug, R. 1985, A&AS, 60, 425
Avni, Y., & Tananbaum, H. 1986, ApJ, 305, 83
Avni, Y., Worrall, D. M., & Morgan, W. A. ApJ, 1995, 454, 673
Avrett, E. H., & Loeser, R. 1988, ApJ, 331, 211
Bahcall, J.H., & Kozlovsky, B.-Z. 1969, ApJ, 155, 1077
Bajtlik, S., Duncan, R. C., & Ostriker, J. P. 1988, ApJ, 327, 570
Balbus, S. A., & McKee, C. F. 1982, ApJ, 252, 529
Baldwin, J., Ferland, G. J., Martin, P. G., Corbin, M., Cota, S., Peterson, B. M., & Slettebak, A. 1991, ApJ, 374, 580
Baldwin J. A., Ferland, G. J., Korista, K. T., Carswell, R., Hamann, F., Phillips, M., Verner, D., Wilkes, B., & Williams, R. E. 1996, ApJ, 461, 683
Baldwin, J. A., Ferland, G. J., Korista K. T., & Verner, D. 1995, ApJ, 455, L119
Baldwin, J.A., Verner, E.M., Verner, D.A., Ferland, G.J., Martin, P.G., Korista, K.T., & Rubin, R. H., 2000, ApJS, 129, 229-246
Baldwin, J., Wampler, J., & Gaskell, C. M. 1989, ApJ, 338, 630
Balick, B., Gammon, R. H., & Hjellming, R. 1974 PASP, 86, 616
Ballantyne, D.R., Ferland, G.J., & Martin, P.G., 2000, ApJ 536, 773-777
Bässgen, G., Bässgen, M., & Grewing, M. 1988, A&A, 200, 51
Bates, D. R., Kingston, A. E., & McWhirter, R. W. P. 1962, Proc R Soc, A267, 297
Bechtold, J., Weymann, R. J., Lin, Z., & Malkan, M. A. 1987, ApJ, 315, 180
Bell, K. L., Kingston, A. E., & McIlveen, W. A. 1975, J. Phys. B 8, 358
Berger, M. J., & Seltzer, S. M. 1965, NASA SP-3012
Bergeron, J., & Collin-Souffrin, S. 1971, A&A, 14, 167
Berrington, K., & Pelan, A. 1995, A&AS, 114, 367
Bertoldi, F., & Draine, B. T. 1996, ApJ, 458, 222
Bethe, H. 1930, Ann. Phys. 5, 325
Bica, E. 1988, A&A, 195, 76
Bieniek, R. J., & Dalgarno, A. 1979, ApJ, 228, 635
Binette, L., Prieto, A., Szuszkiewicz, E., & Zheng, W. 1989, ApJ, 343, 135
Black, J. H. 1978, ApJ, 222, 125
Black, J. H. 1987, in *Interstellar Processes*, ed. D.J. Hollenbach & H.A. Thronson, (Dordrecht: Reidel), p 731
Bohm, D., & Aller, L. H. 1947, ApJ, 105, 131
Bonihala, J. R. M., Ferch, R., Salpeter, E. E., Slater, G., & Noerdlinger, P. 1979, ApJ, 233, 649
Borkowski, K. J., & Harrington, J. P. 1991, ApJ, 379, 168
Bottorff, M., Lamothe, J., Momjian E., Verner, E., Vinkovic, D. & Ferland, G. 1998 PASP, 110, 1040
Bottorff, M. C., Ferland, & Gary J., 2000, MNRAS 316, 103-106
Bottorff, Mark, Ferland, Gary, Baldwin, Jack, & Korista, Kirk, 2000, ApJ, 542, 644-654

Boyd, R., & Ferland, G.J. 1987, ApJ, 318, L21
Bowen, I. S. 1960, ApJ, 132, 1
Bray, I., Burgess, A., Fursa, D.V., & Tully, J.A., 2000, A&AS, 146, 481
Bregman, J. D., Allamandola, L. J., Tielens, A. G. G. M., Geballe, T. R., & Witteborn, F. C. 1989, ApJ, 344, 791
Broad, J. T., & Reinhardt, W. P. 1976, Phys Rev A 14, 2159
Brocklehurst, M., 1970, MNRAS, 148, 417
Brocklehurst, M., 1972, MNRAS, 157, 211
Brown, R. L., & Mathews, W. G. 1970, ApJ, 160, 939
Burgess, A. 1965, ApJ, 141, 1588
Burgess, A., & Summers, H. P. 1969, ApJ, 157, 1007
Burgess, A., & Summers, H. P. 1976, MNRAS, 174, 345
Butler, S. E., Bender, C. F., & Dalgarno, A. 1979, ApJ, 230, L59
Butler, S. E., & Dalgarno, A. 1979, ApJ, 234, 765
Butler, S. E., Heil, T. G., & Dalgarno, A. 1980, ApJ, 241, 442
Butler, S. E., & Dalgarno, A. 1980, ApJ, 241, 838
Callaway, J. 1994, At Dat Nuc Dat Tab 57, 9
Cameron, A.G.W. 1982, in *Essays in Nuclear Astrophysics*, ed CA Barnes, DD Clayton, & DN Schramm, (Cambridge: Cambridge Univ Press)
Canfield, R. C., & Puetter, R. C. 1980, ApJ, 236, L7
Cardelli, J. A. 1994, Science 264, 209
Cardelli, J. A., et al. 1991, ApJ, 377, L57
Castor, J.I., Abbott, D.C., & Klein, R.I., 1975, ApJ, 195, 157-174
Carswell R. F. & Ferland, G. J. 1988, MNRAS, 235, 1121
Castor, J. I. 1970, MNRAS, 149, 111
Chaffee, F. H., & White, R. E. 1982, ApJS, 50, 169
Chamerlain, J.W., 1956, ApJ, 124, 390
Chan, E. S., Avrett, E. H., & Loeser, R. 1991, A&A, 247, 580
Chapman, R. D., & Henry, R. J. W. 1971, ApJ, 168, 169
Chidichimo, M. C. 1981, J. Phys. B., 14, 4149
Clavel, J., & Santos-Lleo, M. 1990, A&A, 230, 3
Clegg, R. E. S. 1987, MNRAS, 229, 31p
Clegg, R. E. S., & Harrington, J. P. 1989, MNRAS, 239, 869
Cohen, E. R., & Taylor, B. N. 1987, Rev Mod Phys 57, 1121
Cota, S. A. 1987, Ph.D. Thesis, OSU
Cota, S. A., & Ferland, G. J. 1988, ApJ, 326, 889
Cowie, L. L., & Songaila, A. 1986, ARA&A 24, 499
Craig, I.J.D., & Brown, J.C., 1986, *Inverse Problems in Astronomy* (Adam Hilger: Bristol)
CrinkLaw, G., Federman, S. R., & Joseph, C. L. 1994, ApJ, 424, 748
Crosas, M., & Weisheit, J.C. 1993, MNRAS, 262, 359
Cruddace, R., Paresce, F., Bowyer, S., & Lampton, M. 1974, ApJ, 187, 497
Dalgarno, A., & Kingston, A. E. 1963, Observatory, 83, 39
Dalgarno, A., & McCray, R. A. 1973, ApJ, 181, 95
Dalgarno, A., & Roberge, W. G. 1979, ApJ, 233, L25
Dalgarno, A., Yan, Min, & Liu, Weihong 1999, ApJS, 125, 237
Davidson, K. 1972, ApJ, 171, 213
Davidson, K. 1975, ApJ, 195, 285
Davidson, K. 1977, ApJ, 218, 20
Davidson, K., & Netzer, H. 1979, Rep. Prog. in Physics 51, 715
Davidson, K., & Fesen, R.A. 1985, ARA&A, 23, 119
Desert, F.-X., Boulanger, F., & Puget, J. L. 1990, A&A, 237, 215
Dove, J. E., Rush, A., Cribb, P., & Martin, P. G. 1987, ApJ, 318, 379
Dove, J. E., & Mandy, M. E. 1986, ApJ, 311, L93
Draine, B. T. 1978, ApJS, 36, 595
Draine, B. T., & Lee, H. M. 1984, ApJ, 285, 89

Draine, B. T., & Salpeter, E. E. 1979, ApJ, 231, 77
Draine, B. T., & Sultin, B. 1987, ApJ, 320, 803
Drake, S. A., & Ulrich, R.K. 1980, ApJS, 42, 351
Elitzur, M. 1982, Rev. Mod. Phys 54, 1125
Elitzur, M. 1984, ApJ, 280, 653
Elitzur, M, 1992, *Astronomical Masers*, (Dordrecht: Kluwer)
Elitzur, M., Ferland, G. J., Mathews, W. G., & Shields, G. 1983, ApJ, 272, L55
Elitzur, M., & Ferland, G. J. 1986, ApJ, 305, 35
Elvis, M. et al. 1994, ApJS, 95, 1
Fabian, A. C., Pringle, J. E., & Rees M. J. 1976, MNRAS, 175, 43
Federman, S. R., et al. 1993, ApJ, 413, L51
Ferguson, J., Ferland, G. J., & A. K. Pradhan, 1995, ApJ, 438, L55
Ferguson, J., & Ferland, G.J. 1997, ApJ, 479, 363
Ferguson, J. W., Korista, K. T., Baldwin, J. A., & Ferland, G. J. 1997, ApJ, 487, 122
Ferguson, Jason W., Korista, Kirk. T., and Ferland, Gary J., 1997, ApJS 110, 287-297.
Ferland, G. J. 1977, ApJ, 212, L21
Ferland, G. J. 1979, MNRAS, 188, 669
Ferland, G. J. 1980a, MNRAS, 191, 243
Ferland, G. J. 1980b, BAAS, 12, 853
Ferland, G. J. 1980c, PASP, 92, 596
Ferland, G. J. 1986, PASP, 98, 549
Ferland, G. J. 1986, ApJ, 310, L67
Ferland, G. J. 1992, ApJ, 389, L63
Ferland, G. J. 1993, ApJS, 88, 49
Ferland, G. J. 1999, PASP, 111, 1524
Ferland, G. J. 1999a, in ASP 162, Quasars and Cosmology, ed G Ferland & J Baldwin
Ferland, G. J., 1999b, ApJ 512 247-249
Ferland, G. J., Baldwin J. A., Korista, K. T., Hamann, F., Carswell, R., Phillips, M., Wilkes, B., & Williams, R. E. 1996, ApJ, 461, 683
Ferland, G., Binette, L., Contini, M., Harrington, J., Kallman, T., Netzer, H., Pequignot, D., Raymond, J., Rubin, R., Shields, G., Sutherland, R., & Viegas, S. 1995, in *The Analysis of Emission Lines*, Space Telescope Science institute Symposium Series, R. Williams & M. Livio, editors (Cambridge: Cambridge University Press)
Ferland, G. J., & Elitzur, M. 1984, ApJ, 285, L11
Ferland, G. J., Fabian, A. C., & Johnstone, R.M. 1994, MNRAS, 266, 399
Ferland, G. J., Korista, K.T. & Peterson, B.M. 1990, ApJ, 363, L21
Ferland, G. J., Korista, K.T., Verner, D. A., & Dalgarno, A. 1997, ApJ, 481, L115
Ferland, G. J. Korista, K.T. Verner, D.A. Ferguson, J.W. Kingdon, J.B. Verner, & E.M. 1998, PASP, 110, 761
Ferland, G. J., Lambert, D. L., Netzer, H., Hall, D. N. B., & Ridgway, S. T. 1979a, ApJ, 227, 489
Ferland, G. J., Lambert, D. L., Slovak, M., Shields, G. A., & McCall, M. 1982, ApJ, 260, 794
Ferland, G. J., & Mushotzky, R. F. 1982, ApJ, 262, 564
Ferland, G. J., & Mushotzky, R. F. 1984, ApJ, 286, 42
Ferland, G. J., & Netzer, H. 1979, ApJ, 229, 274
Ferland, G. J., & Netzer, H. 1983, ApJ, 264, 105
Ferland, G. J., Netzer, H., & Shields, G. A. 1979, ApJ, 232, 382
Ferland, G. J., Peterson, B. M., Horne, K., Welsh, W. F., & Nahar, S. N. 1992, ApJ, 387, 95
Ferland, G. J., & Persson, S. E. 1989, ApJ, 347, 656
Ferland, G. J., & Rees, M. J. 1988, ApJ, 332, 141
Ferland, G. J., & Shields, G. A. 1978, ApJ, 226, 172
Ferland, G. J., & Shields, G. A. 1985, in *Astrophysics of Active Galaxies & Quasi-stellar Objects*, J.S. Miller, Ed.
Ferland, G. J., & Truran, J. W. 1981, ApJ, 244, 1022
Ferland, G. J., Williams, R. E., Lambert, D. L., Shields, G. A., Slovak, M., Gondhalekar, P. M., & Truran, J. W. 1984, ApJ, 281, 194

Field, G. B. 1965, ApJ, 142, 431
Francis, P. J. 1993, ApJ, 407, 519
Gaetz, T. J., & Salpeter, E. E. 1983, ApJS, 52, 155
Garstang, R.H. 1958, MNRAS, 118, 57
Gavrila, M. 1967, Phys Rev 163, 147, also JILA Report #86, Sept 19, 1966
Ginzburg, V. I., & Syrovatskii, S. I. 1964, *The Origin of Cosmic Rays*, (Oxford: Pergamon)
Gould, R. S. 1978, ApJ, 219, 250
Gredel, R., Lepp, S., & Dalgarno, A. 1987, ApJ, 323, L137
Gredel, R., Lepp, S., Dalgarno, A., & Herbst, E. 1989, ApJ, 347, 289
Greenhouse, M., et al. 1993, ApJS, 88, 23
Grevesse, N., & Anders, E. 1989, *Cosmic Abundances of Matter*, AIP Conference Proceedings 183, p. 1, Ed. C. J. Waddington, (New York: AIP)
Grevesse, N. & Noels, A. 1993 in *Origin & Evolution of the Elements*, ed. N. Prantzos, E. Vangioni-Flam, & M. Casse p. 15 (Cambridge: Cambridge Univ. Press)
Guhathakurta, P., & Draine, B. T. 1989, ApJ, 345, 230
Guilbert, P. W. 1986, MNRAS, 218, 171
Guilbert, P., & Rees, M. J. 1988, MNRAS, 233, 475
Habing, H. J. 1968, Bull. Astr. Inst. Netherlands 19, 421
Halpern, J. P., & Grindlay, J. E. 1980, ApJ, 242, 1041
Hamann, F., & Ferland, G. J. 1992, ApJ, 391, L53
Hamann, F., & Ferland, G. J. 1993, ApJ, 418, 11
Hamann, F., & Ferland, G. J. 1999, ARAA, 37, 487
Harrington, J. P. 1969, ApJ, 156, 903
Harrington, J. P. 1973, MNRAS, 162, 43
Heitler, W. 1954, *The Quantum Theory of Radiation* (Oxford: Oxford University Press)
Hjellming, R. M. 1966, ApJ, 143, 420
Hollenbach, D., & McKee, C. F. 1979, ApJS, 41, 555
Hollenbach, D., & McKee, C. F. 1989, ApJ, 342, 306
Hollenbach, D.J., Takahashi, T., & Tielens, A.G.G.M., 1991, ApJ, 377, 192-209
Hubbard, E. N., & Puetter, R. C. 1985, ApJ, 290, 394
Hummer, D. G. 1962, MNRAS, 125, 21
Hummer, D. G. 1968, MNRAS, 138, 73
Hummer, D. G. 1988, ApJ, 327, 477
Hummer, D. G, Berrington, K. A., Eissner, W., Pradhan, A. K., Saraph H. E., Tully, J. A. 1993, A&A, 279, 298
Hummer, D. G., & Kunasz, 1980, ApJ, 236, 609
Hummer, D. G., & Seaton, M. J. 1963, MNRAS, 125, 437
Hummer, D. G., & Storey, P. J. 1987, MNRAS, 224, 801
Hummer, D. G., & Storey, P. J. 1992, MNRAS, 254, 277
Hutchings, J.B. 1976, ApJ, 205, 103
Ikeuchi, S., & Ostriker, J. P. 1986, ApJ, 301, 522
Jackson, J. D. 1975, *Classical Electrodynamics* (New York: Wiley)
Kaler, J., & Jacoby, G. 1991, ApJ, 372, 215
Janev, R. K., Langer, W. D., Post, D. E., & Evans, K. 1987, *Elementary Processes in Hydrogen–Helium Plasmas* (Berlin: Springer--Verlag)
Jenkins, E. B. 1987, in *Interstellar Processes*, D. Hollenbach & H. Thronson, Eds, (Dordrecht: Reidel), p.533
Johnson, L. C. 1972, ApJ, 174, 227
Johnstone, R. M., Fabian, A. C., Edge, A. C., & Thomas, P. A. 1992, MNRAS, 255, 431
Kaler, J., 1978, ApJ, 220, 887
Kallman, T. R., & McCray, R. 1982, ApJS, 50, 263
Karzas, W. J., & Latter, R. 1961, ApJS, 6, 167
Kaastra, J. S., & Mewe, R. 1993, A&AS, 97, 443
Kato, T. 1976, ApJS, 30, 397
Kellerman, K. I. 1966, ApJ, 146, 621

Khromov, G. S. 1989, Space Science Reviews 51, 339
Kingdon, J. B., & Ferland, G. J. 1991, PASP, 103, 752
Kingdon, J. B., & Ferland, G. J. 1993, ApJ, 403, 211
Kingdon, J. B., & Ferland, G. J. 1995, ApJ, 450, 691
Kingdon, J. B., & Ferland, G. J. 1996, ApJS, 106, 205
Kingdon, J. B., Ferland, G. J., & Feibelman, W.A. 1995, ApJ, 439, 793
Kingdon J.B., & Ferland, G.J., 1998, ApJ 506, 323-328
Kingdon, J. B., & Ferland, G. J. 1998, ApJ, 516, L107-109
Korista, K. T., Baldwin, J. A., & Ferland, G. J. 1998, ApJ, 507, 24
Korista, K. T., & Ferland, G. J. 1989, ApJ, 343, 678
Korista, K. T., & Ferland, G. J. 1998, ApJ, 495, 672
Korista, K. T., Ferland, G. J., & Baldwin, J. 1997, ApJ, 487, 555
Krolik, J., McKee, C. M., & Tarter, C.B. 1981, ApJ, 249, 422
Kurucz, R. L. 1970, SAO Special Reports 309
Kurucz, R. L. 1979, ApJS, 40, 1
Kurucz, R. L. 1991, in *Proceedings of the Workshop on Precision Photometry: Astrophysics of the Galaxy*, ed. A. C. Davis Philip, A. R. Upgren, & K. A. James, (Schenectady: Davis), 27
Kwan, J., & Krolik, J. 1981, ApJ, 250, 478
Lambert, D. L., & Pagel, B. E. J. 1968, MNRAS, 141, 299
La Franca, Franceshini, A., Cristiani, S., & Vio, R. 1995, A&A, 299, 19
Lame N. J., & Ferland, G. J. 1991, ApJ, 367, 208
Landini, M., & Monsignori Fossi, B. 1990, A&AS, 82, 229
Landini, M., & Monsignori Fossi, B. 1991, A&AS, 91, 183
Lanzafame, A., Tully, J. A., Berrington, K. A., Dufton, P. L., Byrne, P. B., & Burgess, A. 1993, MNRAS, 264, 402
Laor, A., & Draine, B. T. 1993, ApJ, 402, 441
Latter, W. B., & Black, J. H. 1991, ApJ, 372, 161
Lea, S., & Holman, G. 1978, ApJ, 222, 29
Lennon, D. J., & Burke, V. M. 1991, MNRAS, 251, 628
Lenzuni, P., Chernoff, D. F., & Salpeter, E. E. 1991, ApJS, 76, 759
Levich, E. V., & Sunyaev, R.A. 1970, Astrophysical Letters 7, 69
Lepp, S., & Shull, J. M. 1983, ApJ, 270, 578
Lightman, A. P., & White, T.R. 1988, ApJ, 335, 57
Liske, J., 2000, MNRAS, 319, 557-561
Lites, B. W., & Mihalas, D. 1984, Solar Physics 93, 23
Liu, X.-W., Storey, P. J., Barlow, M. J., & Clegg, R. E. S. 1995, MNRAS, 272, 369
Longair, M. S. 1981, *High Energy Astrophysics*, (Cambridge: Cambridge University Press)
Lotz, W. 1967, ApJS, 14, 207
MacAlpine, G. M. 1971, ApJ, 175, 11
Maguire, S. 1993, *Writing Solid Code*, Microsoft Press
Mallik, D. C. V., & Peimbert, M. 1988, Rev Mexicana 16, 111
Martin, P. G. 1979, *Cosmic Dust* (Oxford: Clarendon Press)
Martin, P. G. 1988, ApJS, 66, 125
Martin, P. G., & Ferland, G. J. 1980, ApJ, 235, L125
Martin, P.G., & Rouleau, F., 1991, in Malina R.F., Bowyer S., eds, Extreme Ultraviolet Astronomy, Pergamon Press, Oxford, p. 341
Martin, P. G., & Whittet, D. C. B. 1990, ApJ, 357, 113
Masters, A. R., Pringle, J. E., Fabian, A. C., & Rees, M. J. 1977, MNRAS, 178, 501
Mathews, W. G., Blumenthal, G. R., & Grandi, S. A. 1980, ApJ, 235, 971
Mathews, W. G., & Ferland, G. J. 1987, ApJ, 323, 456
Mathis, J. S. 1982, ApJ, 261, 195
Mathis, J. S. 1985, ApJ, 291, 247
Mathis, J. S., Rumpl, W., & Nordsieck, K. H. 1977, ApJ, 217, 425
Mathis, J. S., & Wallenhorst, S. G. 1981, ApJ, 244, 483
Matteucci, F., & Tornambe, A. 1987, A&A, 185, 51

Matteucci, F., & Greggio, A. 1986, A&A, 154, 279
Mazzotta, P., Mazzitelli, G., Colafrancesco, C., & Vittorio, 1998, A&AS 133, 403-409
McKee, C. F. 1999, preprint, Astro-ph 9901370
Mendoza, C. 1983, in *Planetary Nebulae*, IAU Sym 103, D. R. Flower, Ed., p 143, (Dordrecht: Reidel)
Meyer, D.M., Jura, M., & Cardelli, J.A. 1998, ApJ, 493, 222-229
Mewe, R. 1972, A&A, 20, 215
Mihalas, D. 1972, *Non-LTE Model Atmospheres for B & O Stars*, NCAR-TN / STR-76
Mihalas, D. 1978, *Stellar Atmospheres*, 2nd Edition (San Francisco: W.H. Freeman)
Mihalszki, J. S., & Ferland, G. J. 1983, PASP, 95, 284
Morrison, R., & McCammon, D. 1983, ApJ, 270, 119
Morton, D. C., York, D. G., & Jenkins, E. B. 1988, ApJS, 68, 449
Nahar, S. N., & Pradhan, A. K. 1992, ApJ, 397, 729
Netzer, H. 1990, in *Active Galactic Nuclei, Saas-Fee Advanced Course 20*, Courvorsier, T.J.-L., & Mayor, M., (Springer-Verlag; Berlin)
Netzer, H., Elitzur, M., & Ferland, G. J. 1985, ApJ, 299, 752
Netzer, H., & Ferland, G. J. 1984, PASP, 96, 593
Neufeld, D. A. 1989, Harvard Research Exam
Neufeld, D. A., & Dalgarno, A. 1989, Phys Rev A, 35, 3142
Novotny, Eva, 1973, *Introduction to Stellar Atmospheres*, (New York; Oxford University Press)
Nussbaumer, H., & Storey, P. J. 1983, A&A, 126, 75
Nussbaumer, H., & Storey, P. J. 1984, A&AS, 56, 293
Nussbaumer, H., & Storey, P. J. 1986, A&AS, 64, 545
Nussbaumer, H., & Storey, P. J. 1987, A&AS, 69, 123
Oliveira, S., & Maciel, W. J. 1986, Ap&SS, 126, 211
Oliva, E., Pasquali, A., & Reconditi, M. 1996, A&A, 305, 210
Osterbrock, D. E. 1951, ApJ, 114, 469
Osterbrock, D. E. 1989, *Astrophysics of Gaseous Nebulae & Active Galactic Nuclei*, (Mill Valley; University Science Press)
Osterbrock, D. E., & Flather, E. 1959, ApJ, 129, 26
Osterbrock, D. E., Tran, H. D., & Veilleux, S. 1992, ApJ, 389, 305
Ostriker, J. P., & Ikeuchi, S. 1983, ApJ, 268, L63
Pacholczyk, A. G. 1970, *Radio Astrophysics* (San Francisco: Freeman)
Pagel, B. E. J. 1997, *Nucleosynthesis and Chemical Evolution of Galaxies*, (Cambridge: Cambridge University Press)
Palla, F., Salpeter, E. E., & Stahler, S. W. 1983, ApJ, 271, 632
Peebles, P. J. E. 1971, *Physical Cosmology*, (Princeton: Princeton U. Press)
Peimbert, M. 1967, ApJ, 150, 825
Pengelly, R. M. 1964, MNRAS, 127, 145
Pequignot, D. 1986, *Wordshop on Model Nebulae*, (Paris: l'Observatoire de Paris) p363
Pequignot, D., & Aldrovandi, S.M.V. 1986, A&A, 161, 169
Pequignot, D., Stasinska, G., & Aldrovandi, S. M. V. 1978, A&A, 63, 313
Pequignot, D., Petitjean, P., & Boisson, C. 1991, A&A, 251, 680
Peterson, J. R., Aberth, W., Moseley, J., & Sheridan, J. 1971, Phys Rev A, 3, 1651
Prasad, S.S., & Huntress, W.T., 1980, ApJS, 43, 1-35
Press W. H., Teukolsky, S.A., Vetterling, W. T., & Flannery, B. P. 1992, *Numerical Recipes*, (Cambridge; Cambridge University Press)
Puetter, R. C. 1981, ApJ, 251, 446
Puy, D., Alecian, G., Le Bourlot, J., Leorat, J., & Pineau des Forets, G. 1993, A&A, 267, 337
Rauch, T. 1997 A&A, 320, 237
Raymond, J. C., Cox, D. P., & Smith, B. W. 1976, ApJ, 204, 290
Rees, M. J., Netzer, H., & Ferland, G. J. 1989, ApJ, 347, 640
van Regemorter, H. 1962, ApJ, 136, 906
Rephaeli, Y. 1987, MNRAS, 225, 851
Reilman, R. F., & Manson, S. T. 1979, ApJS, 40, 815, errata 46, 115; 62, 939
Roberge, W. G., Jones, D., Lepp, S., & Dalgarno, A. 1991, ApJS, 77, 287

Rossi, B. 1952, *High-Energy Particles* (New York; Prentice-Hall)
Rouleau, F., & Martin, P.G. 1991, ApJ, 377, 526
Rowan, T. 1990, *Functional Stability Analysis of Numerical Algorithms*, Ph.D. Thesis, Department of Computer Sciences, University of Texas at Austin
Rubin, R. H. 1968, ApJ, 153, 671
Rubin, R. H. 1983, ApJ, 274, 671
Rubin, R. H. Martin, P. G. Dufour, R. J. Ferland, G. J Baldwin, J. A. Hester, J. J. & Walter, D. K. 1998, ApJ, 495, 891
Rubin, R. H., Simpson, J. R., Haas, M. R., & Erickson, E. F. 1991, ApJ, 374, 564
Rybicki, G. B., & Hummer, D. G. 1991, A&A, 245, 171
Rybicki, G. B., & Hummer, D. G. 1992, A&A, 262, 209
Rybicki, G. B., & Hummer, D. G. 1994, A&A, 290, 553
Rybicki, G. B., & Lightman, A.P. 1979, *Radiative Processes in Astrophysics* (New York: Wiley)
Sanders, D. B., et al. 1989, ApJ, 347, 29
Saraph, H. E. 1970, J.Phys.B., 3, 952
Savage, B. D., & Sembach, K. R. 1996, ARA&A, 34, 279
Savin, Daniel Wolf, 2000, ApJ, 533, 106
Savin, D. W.; Kahn, S. M.; Linkemann, J.; Saghiri, A. A.; Schmitt, M.; Grieser, M.; Repnow, R.; Schwalm, D.; Wolf, A.; Bartsch, T.; Brandau, C.; Hoffknecht, A.; Müller, A.; Schippers, S.; Chen, M. H.; Badnell, N. R., 1999, ApJS, 123, 687
Sciortino, S., et al. 1990, ApJ, 361, 621
Scott, J. S., Holman, G. D., Ionson, J. A., & Papadopoulos, K. 1980, ApJ, 239, 769
Schaerer D., de Koter, A., Schmutz, W., & Maeder, A. 1996ab, A&A, 310, 837, & A&A, 312, 475
Schaerer D., & de Koter A. 1997, A&A, 322, 592
Schuster, A. 1905, ApJ, 21, 1
Schutte, W. A., Tielens, A. G. G. M., & Allamandola, L. J. 1993, ApJ, 415, 397
Schwarzschild, M. 1965, *Structure & Evolution of the Stars*, (New York: Dover)
Seaton, M. J. 1959, MNRAS, 119, 81
Seaton, M. J. 1959, MNRAS, 119, 90
Seaton, M. J. 1987, J.Phys. B, 20, 6363
Sellmaier, F. H., Yamamoto, T., Pauldrach, A. W. A., & Rubin, R. H. 1996, A&A, 305, L37
Shields, G. A. 1976, ApJ, 204, 330
Shine, R. A., & Linsky, J. L. 1974, Solar Physics 39, 49
Shull, J. M. 1979, ApJ, 234, 761
Shull, J. M., & Van Steenberg, M. E. 1982, ApJS, 48, 95
Shull, J. M., & Van Steenberg, M. E. 1985, ApJ, 298, 268
Sellgren, K., Tokunaga, A. T., & Nakada, Y. 1990, ApJ, 349, 120
Sellmaier, F.H., Yamamoto, T., Pauldrach, A.W.A., Rubin, R.H 1996, A&A, 305, 37
Sikora, M., Begelman, M. C., & Rudak, B. 1989, ApJ, 341, L33
Simonyi, C. 1977, *Meta-Programming: A Software Production Method*, Thesis, Stanford University
Snow, T. P., & Dodger, S. L. 1980, ApJ, 237, 708
Snow, T. P., & York, D. G. 1981, ApJ, 247, L39
Snow, T.P., & Witt, A. 1996, ApJ, 468, L65
Spitzer, L. 1948, ApJ, 107, 6
Spitzer, L. 1962, *Physics of Fully Ionized Gasses*, (New York: Interscience)
Spitzer, L. 1978, *Physical Processes in the Interstellar Medium*, (New York: Wiley)
Spitzer, L. 1985, ApJ, 290, L21
Spitzer, L., & Tomasko, M. G. 1968, ApJ, 152, 971
Stecher, T. P., & Williams, D. A. 1967, ApJ, 149, 29
Stoy, R. H. 1933, MNRAS, 93, 588
Storey P. J. 1981, MNRAS, 195, 27p
Storey, P. J. 1994, A&A, 282, 999
Storey, P. J., & Hummer, D. G. 1991, Comput. Phys. Commun. 66, 129
Storey, P. J., & Hummer, D. G. 1995, MNRAS, 272, 41 (on the web at http://adc.gsfc.nasa.gov/adc-cgi/cat.pl?/catalogs/6/6064/)

Swings, P., & Struve, O. 1940, ApJ, 91, 546
Tarter, C. B., & McKee, C. F. 1973, ApJ, 186, L63
Tarter, C.B., Tucker, W.H., & Salpeter, E.E., 1969, ApJ, 156, 943
Tielens, A. G. G. M., & Hollenbach, D. 1985a, ApJ, 291, 722
Tielens, A. G. G. M., & Hollenbach, D. 1985b, ApJ, 291, 746
Tout, C. A., Pols, O. R., Eggleton, P. P. & Han, Z. 1996, MNRAS, 281, 257
Turner, J., & Pounds, K. 1989, MNRAS, 240, 833
Van Blerkom, D., & Hummer, D. G. 1967, MNRAS, 137, 353
van Dishoeck, E.F., & Black, J.H., 1988, ApJ, 334, 771
van Hoof, P. A. M. 1997, PhD Thesis, University of Groningen
van Hoof, P.A.M., Beintema, D.A., Verner D.A., & Ferland, G.J., 2000a, A&A 354, L41-L44
van Hoof, P.A.M., Van de Steene, G.C., Beintema, D.A., Martin, P.G., Pottasch, S.R., Ferland, G. J., 2000b, ApJ 532, 384-399
van Regemorter, H. 1962, ApJ, 136, 906
Vedel, H., Hellsten, U., & Sommer-Larsen, J. 1994, MNRAS, 271, 743
Vernazza, J. E., Avrett, E. H., & Loeser, C. B. 1981, ApJS, 45, 635
Verner, D. A., Yakovlev, D. G., Band, I. M., & Trzhaskovshaya, M. B. 1993, ADNDT, 55, 233
Verner, D. A ., & Yakovlev, 1995, A&AS, 109, 125
Verner, D. A., & Ferland, G. J. 1996, ApJS, 103, 467
Verner, D. A., Ferland, G. J., Korista, K., & Yakovlev D. G. 1996, ApJ, 465, 487
Verner, D. A., Verner, K., & Ferland, G. J. 1996, ADNDT, 64, 1
Verner, E.M. Verner, D.A. Korista, K.T. Ferguson , J.W. Hamann, F. & Ferland, G.J. 1999, ApJS 120, 101
Voronov, G. S. 1997, ADNDT, 65, 1
Voit, G. M. 1991, ApJ, 377, 1158
Volk, K., and Kwok, S. 1988, ApJ, 331, 435
Vriens, L., & Smeets, A. H. M. 1980, Phys Rev A, 22, 940
Watson, W. D. 1972, ApJ, 176, 103
Weisheit, J. C. 1974, ApJ, 190, 735
Weisheit, J. C., & Collins, L. A. 1976, ApJ, 210, 299
Weisheit, J. C., & Dalgarno, A. 1972, Astrophysical Letters, 12, 103
Weisheit, J., Shields, G. A., & Tarter, C. B. 1981, ApJ, 245, 406
Werner, K., & Heber, U. 1991, in *Stellar Atmospheres: Beyond Classical Models*, p 341, NATO ASI Series C, eds. L. Crivellari, I. Hubney, & D. G. Hummer, (Dordrect: Kluwer)
White, R. E. 1986, ApJ, 307, 777
Wiese, W.L., Fuhr, J.R., & Deters, T.M., 1996, J Phys Chem Ref Data, Monograph 7
Wiese, W. L., Smith, M. W., & Glennon, B. M. 1966, NSRDS-NBS 4
Wilkes, B. J., Ferland, G. J., Truran, J., & Hanes, D. 1981, MNRAS, 197, 1
Wilkes, et al 1994, ApJS, 92, 53
Wilkinson, D. T. 1987, in *13th Texas Symposium on Relativistic Astrophysics*, M. P. Ulmer, ed., (Singapore: World Scientific), p209
Williams, R. E. 1967, ApJ, 147, 556
Williams, R. E. 1992, ApJ, 392, 99
Wills, B., Netzer, H., & Wills, D. 1985, ApJ, 288, 94
Winslow, A. M. 1975, Lawrence Livermore Lab. report UCID-16854
Wishart, A. W. 1979, MNRAS, 187, 59p
Wolfire, M. G., Tielens, A., & Hollenbach, D. 1990, ApJ, 358, 116
Worral et al. 1987, ApJ, 313, 596
Wyse, A. B. 1941, PASP, 53, 184
York, D. G., Meneguzzi, M., & Snow, T. 1982, ApJ, 255, 524
Xu, Y., & McCray, R. 1991, ApJ, 375, 190
Zamorani, G., et al. 1981, ApJ, 245, 357
Zheng, W., Kriss, G.A., Telfer, R.C., Grimes, JP. & Davidsen, A.F. 1997, ApJ, 475, 469
Zuckerman, B. 1973, ApJ, 183, 863
Zycki, P. T., Krolik, J. H., Zdziarski, A. A., & Kallman, T. R. 1994, 437, 597
Zygelman, B., & Dalgarno, A. 1990, ApJ, 365, 239